

World Journal of *Radiology*

World J Radiol 2012 January 28; 4(1): 1-35





Editorial Board

2009-2013

The *World Journal of Radiology* Editorial Board consists of 319 members, representing a team of worldwide experts in radiology. They are from 40 countries, including Australia (3), Austria (4), Belgium (5), Brazil (3), Canada (9), Chile (1), China (25), Czech (1), Denmark (1), Egypt (4), Estonia (1), Finland (1), France (6), Germany (17), Greece (8), Hungary (1), India (9), Iran (5), Ireland (1), Israel (4), Italy (28), Japan (14), Lebanon (1), Libya (1), Malaysia (2), Mexico (1), Netherlands (4), New Zealand (1), Norway (1), Saudi Arabia (3), Serbia (1), Singapore (2), Slovakia (1), South Korea (16), Spain (8), Switzerland (5), Thailand (1), Turkey (20), United Kingdom (16), and United States (82).

PRESIDENT AND EDITOR-IN-CHIEF

Filippo Cademartiri, *Monastier di Treviso*

STRATEGY ASSOCIATE EDITORS-IN-CHIEF

Ritesh Agarwal, *Chandigarh*
Kenneth Coenegrachts, *Bruges*
Mannudeep K Kalra, *Boston*
Meng Law, *Los Angeles*
Ewald Moser, *Vienna*
Aytekin Oto, *Chicago*
AAK Abdel Razek, *Mansoura*
Àlex Rovira, *Barcelona*
Yi-Xiang Wang, *Hong Kong*
Hui-Xiong Xu, *Guangzhou*

GUEST EDITORIAL BOARD MEMBERS

Wing P Chan, *Taipei*
Wen-Chen Huang, *Taipei*
Shi-Long Lian, *Kaohsiung*
Chao-Bao Luo, *Taipei*
Shu-Hang Ng, *Taoyuan*
Pao-Sheng Yen, *Hualien*

MEMBERS OF THE EDITORIAL BOARD



Australia

Karol Miller, *Perth*
Tomas Kron, *Melbourne*
Zhonghua Sun, *Perth*



Austria

Herwig R Cerwenka, *Graz*

Daniela Prayer, *Vienna*
Siegfried Trattnig, *Vienna*



Belgium

Piet R Dirix, *Leuven*
Yicheng Ni, *Leuven*
Piet Vanhoenacker, *Aalst*
Jean-Louis Vincent, *Brussels*



Brazil

Emerson L Gasparetto, *Rio de Janeiro*
Edson Marchiori, *Petrópolis*
Wellington P Martins, *São Paulo*



Canada

Sriharsha Athreya, *Hamilton*
Mark Otto Baerlocher, *Toronto*
Martin Charron, *Toronto*
James Chow, *Toronto*
John Martin Kirby, *Hamilton*
Piyush Kumar, *Edmonton*
Catherine Limperopoulos, *Quebec*
Ernest K Osei, *Kitchener*
Weiguang Yao, *Sudbury*



Chile

Masami Yamamoto, *Santiago*



China

Feng Chen, *Nanjing*
Ying-Sheng Cheng, *Shanghai*
Woei-Chyn Chu, *Taipei*

Guo-Guang Fan, *Shenyang*
Shen Fu, *Shanghai*
Gang Jin, *Beijing*
Tak Yeung Leung, *Hong Kong*
Wen-Bin Li, *Shanghai*
Rico Liu, *Hong Kong*
Yi-Yao Liu, *Chengdu*
Wei Lu, *Guangdong*
Fu-Hua Peng, *Guangzhou*
Liang Wang, *Wuhan*
Li-Jun Wu, *Hefei*
Zhi-Gang Yang, *Chengdu*
Xiao-Ming Zhang, *Nanchong*
Chun-Jiu Zhong, *Shanghai*



Czech

Vlastimil Válek, *Brno*



Denmark

Poul Erik Andersen, *Odense*



Egypt

Mohamed Abou El-Ghar, *Mansoura*
Mohamed Ragab Nouh, *Alexandria*
Ahmed A Shokeir, *Mansoura*



Estonia

Tiina Talvik, *Tartu*



Finland

Tove J Grönroos, *Turku*

**France**

Alain Chapel, *Fontenay-Aux-Roses*
 Nathalie Lassau, *Villejuif*
 Youlia M Kirova, *Paris*
 Géraldine Le Duc, *Grenoble Cedex*
 Laurent Pierot, *Reims*
 Frank Pilleul, *Lyon*
 Pascal Pommier, *Lyon*

**Germany**

Ambros J Beer, *München*
 Thomas Deserno, *Aachen*
 Frederik L Giesel, *Heidelberg*
 Ulf Jensen, *Kiel*
 Markus Sebastian Juchems, *Ulm*
 Kai U Juergens, *Bremen*
 Melanie Kettering, *Jena*
 Jennifer Linn, *Munich*
 Christian Lohrmann, *Freiburg*
 David Maintz, *Münster*
 Henrik J Michaely, *Mannheim*
 Oliver Micke, *Bielefeld*
 Thoralf Niendorf, *Berlin-Buch*
 Silvia Obenauer, *Duesseldorf*
 Steffen Rickes, *Halberstadt*
 Lars V Baron von Engelhardt, *Bochum*
 Goetz H Welsch, *Erlangen*

**Greece**

Panagiotis Antoniou, *Alexandroupolis*
 George C Kagadis, *Rion*
 Dimitris Karacostas, *Thessaloniki*
 George Panayiotakis, *Patras*
 Alexander D Rapisdis, *Athens*
 C Triantopoulou, *Athens*
 Ioannis Tsalafoutas, *Athens*
 Virginia Tsapaki, *Anixi*
 Ioannis Valais, *Athens*

**Hungary**

Peter Laszlo Lakatos, *Budapest*

**India**

Anil Kumar Anand, *New Delhi*
 Surendra Babu, *Tamilnadu*
 Sandip Basu, *Bombay*
 Kundan Singh Chufal, *New Delhi*
 Shivanand Gamanagatti, *New Delhi*
 Vimoj J Nair, *Haryana*
 R Prabhakar, *New Delhi*
 Sanjeeb Kumar Sahoo, *Orissa*

**Iran**

Vahid Reza Dabbagh Kakhki, *Mashhad*
 Mehran Karimi, *Shiraz*
 Farideh Nejat, *Tehran*
 Alireza Shirazi, *Tehran*
 Hadi Rokni Yazdi, *Tehran*

**Ireland**

Joseph Simon Butler, *Dublin*

**Israel**

Amit Gefen, *Tel Aviv*
 Eyal Sheiner, *Be'er-Sheva*
 Jacob Sosna, *Jerusalem*
 Simcha Yagel, *Jerusalem*

**Italy**

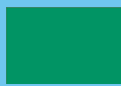
Mohssen Ansarin, *Milan*
 Stefano Arcangeli, *Rome*
 Tommaso Bartalena, *Imola*
 Filippo Cademartiri, *Parma*
 Sergio Casciaro, *Lecce*
 Laura Crocetti, *Pisa*
 Alberto Cuocolo, *Napoli*
 Mirko D'Onofrio, *Verona*
 Massimo Filippi, *Milan*
 Claudio Fiorino, *Milano*
 Alessandro Franchello, *Turin*
 Roberto Grassi, *Naples*
 Stefano Guerriero, *Cagliari*
 Francesco Lassandro, *Napoli*
 Nicola Limbucci, *L'Aquila*
 Raffaele Lodi, *Bologna*
 Francesca Maccioni, *Rome*
 Laura Martincich, *Candiolo*
 Mario Mascacchi, *Florence*
 Roberto Miraglia, *Palermo*
 Eugenio Picano, *Pisa*
 Antonio Pinto, *Naples*
 Stefania Romano, *Naples*
 Luca Saba, *Cagliari*
 Sergio Sartori, *Ferrara*
 Mariano Scaglione, *Castel Volturno*
 Lidia Strigari, *Rome*
 Vincenzo Valentini, *Rome*

**Japan**

Shigeru Ehara, *Morioka*
 Nobuyuki Hamada, *Chiba*
 Takao Hiraki, *Okayama*
 Akio Hiwatashi, *Fukuoka*
 Masahiro Jinzaki, *Tokyo*
 Hiroshi Matsuda, *Saitama*
 Yasunori Minami, *Osaka*
 Jun-Ichi Nishizawa, *Tokyo*
 Tetsu Niwa, *Yokohama*
 Kazushi Numata, *Kanagawa*
 Kazuhiko Ogawa, *Okinawa*
 Hitoshi Shibuya, *Tokyo*
 Akira Uchino, *Saitama*
 Haiquan Yang, *Kanagawa*

**Lebanon**

Aghiad Al-Kutoubi, *Beirut*

**Libya**

Anuj Mishra, *Tripoli*

**Malaysia**

R Logeswaran, *Cyberjaya*
 Kwan-Hoong Ng, *Kuala Lumpur*

**Mexico**

Heriberto Medina-Franco, *Mexico City*

**Netherlands**

Jurgen J Fütterer, *Nijmegen*
 Raffaella Rossin, *Eindhoven*
 Paul E Sijens, *Groningen*

**New Zealand**

W Howell Round, *Hamilton*

**Norway**

Arne Sigmund Borthne, *Lørenskog*

**Saudi Arabia**

Mohammed Al-Omran, *Riyadh*
 Ragab Hani Donkol, *Abha*
 Volker Rudat, *Al Khobar*

**Serbia**

Djordjije Saranovic, *Belgrade*

**Singapore**

Uei Pua, *Singapore*
 Lim CC Tchoyoson, *Singapore*

**Slovakia**

František Dubecký, *Bratislava*

**South Korea**

Bo-Young Choe, *Seoul*
 Joon Koo Han, *Seoul*
 Seung Jae Huh, *Seoul*
 Chan Kyo Kim, *Seoul*
 Myeong-Jin Kim, *Seoul*
 Seung Hyup Kim, *Seoul*
 Kyoung Ho Lee, *Gyeonggi-do*
 Won-Jin Moon, *Seoul*
 Wazir Muhammad, *Daegu*
 Jai Soung Park, *Bucheon*
 Noh Hyuck Park, *Kyunggi*
 Sang-Hyun Park, *Daejeon*
 Joon Beom Seo, *Seoul*
 Ji-Hoon Shin, *Seoul*
 Jin-Suck Suh, *Seoul*
 Hong-Gyun Wu, *Seoul*



Spain

Eduardo J Aguilar, *Valencia*
 Miguel Alcaraz, *Murcia*
 Juan Luis Alcazar, *Pamplona*
 Gorka Bastarrika, *Pamplona*
 Rafael Martínez-Monge, *Pamplona*
 Alberto Muñoz, *Madrid*
 Joan C Vilanova, *Girona*



Switzerland

Nicolau Beckmann, *Basel*
 Silke Grabherr, *Lausanne*
 Karl-Olof Lövblad, *Geneva*
 Tilo Niemann, *Basel*
 Martin A Walter, *Basel*



Thailand

Sudsriluk Sampatchalit, *Bangkok*



Turkey

Olus Api, *Istanbul*
 Kubilay Aydin, *Istanbul*
 Işıl Bilgen, *Izmir*
 Zulkif Bozgeyik, *Elazig*
 Barbaros E Çil, *Ankara*
 Gulgun Engin, *Istanbul*
 M Fatih Evcimik, *Malatya*
 Ahmet Kaan Gündüz, *Ankara*
 Tayfun Hakan, *Istanbul*
 Adnan Kabaalioglu, *Antalya*
 Fehmi Kaçmaz, *Ankara*
 Musturay Karcaaltincaba, *Ankara*
 Osman Kizilkilic, *Istanbul*
 Zafer Koc, *Adana*
 Cem Onal, *Adana*
 Yahya Paksoy, *Konya*
 Bunyamin Sahin, *Samsun*
 Ercument Unlu, *Edirne*
 Ahmet Tuncay Turgut, *Ankara*
 Ender Uysal, *Istanbul*



United Kingdom

K Faulkner, *Wallsend*
 Peter Gaines, *Sheffield*
 Balaji Ganeshan, *Brighton*
 Nagy Habib, *London*
 Alan Jackson, *Manchester*
 Pradesh Kumar, *Portsmouth*
 Tarik F Massoud, *Cambridge*
 Igor Meglinski, *Bedfordshire*
 Robert Morgan, *London*
 Ian Negus, *Bristol*
 Georgios A Plataniotis, *Aberdeen*
 N J Raine-Fenning, *Nottingham*
 Manuchehr Soleimani, *Bath*
 MY Tseng, *Nottingham*
 Edwin JR van Beek, *Edinburgh*
 Feng Wu, *Oxford*



United States

Athanassios Argiris, *Pittsburgh*
 Stephen R Baker, *Newark*
 Lia Bartella, *New York*
 Charles Bellows, *New Orleans*
 Walter L Biffl, *Denver*
 Homer S Black, *Houston*
 Wessam Bou-Assaly, *Ann Arbor*
 Owen Carmichael, *Davis*
 Shelton D Caruthers, *St Louis*
 Yuhchayau Chen, *Rochester*
 Melvin E Clouse, *Boston*
 Ezra Eddy Wyssam Cohen, *Chicago*
 Aaron Cohen-Gadol, *Indianapolis*
 Patrick M Colletti, *Los Angeles*
 Kassa Darge, *Philadelphia*
 Abhijit P Datir, *Miami*
 Delia C DeBuc, *Miami*
 Russell L Deter, *Houston*
 Adam P Dicker, *Phil*
 Khaled M Elsayes, *Ann Arbor*
 Steven Feigenberg, *Baltimore*
 Christopher G Filippi, *Burlington*
 Victor Frenkel, *Bethesda*
 Thomas J George Jr, *Gainesville*
 Patrick K Ha, *Baltimore*
 Robert I Haddad, *Boston*
 Walter A Hall, *Syracuse*
 Mary S Hammes, *Chicago*

John Hart Jr, *Dallas*
 Randall T Higashida, *San Francisco*
 Juebin Huang, *Jackson*
 Andrei Iagaru, *Stanford*
 Craig Johnson, *Milwaukee*
 Ella F Jones, *San Francisco*
 Csaba Juhasz, *Detroit*
 Riyadh Karmy-Jones, *Vancouver*
 Daniel J Kelley, *Madison*
 Amir Khan, *Longview*
 Euishin Edmund Kim, *Houston*
 Vikas Kundra, *Houston*
 Kenneth F Layton, *Dallas*
 Rui Liao, *Princeton*
 CM Charlie Ma, *Philadelphia*
 Nina A Mayr, *Columbus*
 Thomas J Meade, *Evanston*
 Steven R Messé, *Philadelphia*
 Nathan Olivier Mewton, *Baltimore*
 Feroze B Mohamed, *Philadelphia*
 Koenraad J Morteale, *Boston*
 Mohan Natarajan, *San Antonio*
 John L Noshier, *New Brunswick*
 Chong-Xian Pan, *Sacramento*
 Dipanjan Pan, *St Louis*
 Martin R Prince, *New York*
 Reza Rahbar, *Boston*
 Carlos S Restrepo, *San Antonio*
 Veronica Rooks, *Honolulu*
 Maythem Saeed, *San Francisco*
 Edgar A Samaniego, *Palo Alto*
 Kohkan Shamsi, *Doylestown*
 Jason P Sheehan, *Charlottesville*
 William P Sheehan, *Willmar*
 Charles Jeffrey Smith, *Columbia*
 Monvadi B Srichai-Parsia, *New York*
 Dan Stoianovici, *Baltimore*
 Janio Szklaruk, *Houston*
 Dian Wang, *Milwaukee*
 Jian Z Wang, *Columbus*
 Shougang Wang, *Santa Clara*
 Wenbao Wang, *New York*
 Aaron H Wolfson, *Miami*
 Gayle E Woloschak, *Chicago*
 Ying Xiao, *Philadelphia*
 Juan Xu, *Pittsburgh*
 Benjamin M Yeh, *San Francisco*
 Terry T Yoshizumi, *Durham*
 Jinxing Yu, *Richmond*
 Jianhui Zhong, *Rochester*



Contents

Monthly Volume 4 Number 1 January 28, 2012

EDITORIAL

- 1 Value of MR contrast media in image-guided body interventions
Saeed M, Wilson M

REVIEW

- 13 CT and MR imaging patterns for pancreatic carcinoma invading the
extrapancreatic neural plexus. Part II : Imaging of pancreatic carcinoma
nerve invasion
Zuo HD, Tang W, Zhang XM, Zhao QH, Xiao B

BRIEF ARTICLES

- 21 Radiation dose reduction with application of non-linear adaptive filters for
abdominal CT
Singh S, Kalra MK, Sung MK, Back A, Blake MA
- 29 Aortic ostia of the bronchial arteries and tracheal bifurcation: MDCT analysis
*Ziyawudong J, Kawai N, Sato M, Ikoma A, Sanda H, Takeuchi T, Minamiguchi H, Nakai M,
Tanaka T, Sonomura T*

Contents

World Journal of Radiology
Volume 4 Number 1 January 28, 2012

ACKNOWLEDGMENTS I Acknowledgments to reviewers of *World Journal of Radiology*

APPENDIX I Meetings

I-V Instructions to authors

ABOUT COVER Editor-in-Chief of *World Journal of Radiology*, Filippo Cademartiri, MD, PhD, FESC, FSCCT, Professor, Cardio-Vascular Imaging Unit-Giovanni XXIII Hospital, Via Giovanni XXIII, 7-31050-Monastier di Treviso (TV), Italy

AIM AND SCOPE

World Journal of Radiology (*World J Radiol*, *WJR*, online ISSN 1949-8470, DOI: 10.4329) is a monthly peer-reviewed, online, open-access, journal supported by an editorial board consisting of 319 experts in radiology from 40 countries.

The major task of *WJR* is to rapidly report the most recent improvement in the research of medical imaging and radiation therapy by the radiologists. *WJR* accepts papers on the following aspects related to radiology: Abdominal radiology, women health radiology, cardiovascular radiology, chest radiology, genitourinary radiology, neuroradiology, head and neck radiology, interventional radiology, musculoskeletal radiology, molecular imaging, pediatric radiology, experimental radiology, radiological technology, nuclear medicine, PACS and radiology informatics, and ultrasound. We also encourage papers that cover all other areas of radiology as well as basic research.

FLYLEAF I-III Editorial Board

EDITORS FOR THIS ISSUE

Responsible Assistant Editor: *Jian-Xia Cheng*
Responsible Electronic Editor: *LJ Xiong*
Proofing Editor-in-Chief: *Lian-Sheng Ma*

Responsible Science Editor: *Jian-Xia Cheng*

NAME OF JOURNAL

World Journal of Radiology

ISSN

ISSN 1949-8470 (online)

LAUNCH DATE

December 31, 2009

FREQUENCY

Monthly

EDITING

Editorial Board of *World Journal of Radiology*, Room 903, Building D, Ocean International Center, No. 62 Dongsihuan Zhonglu, Chaoyang District, Beijing 100025, China
Telephone: +86-10-59080039
Fax: +86-10-85381893
E-mail: wjr@wjgnet.com
<http://www.wjgnet.com>

EDITOR-IN-CHIEF

Filippo Cademartiri, MD, PhD, FESC, FSCCT, Professor, Cardio-Vascular Imaging Unit-Giovanni XXIII Hospital, Via Giovanni XXIII, 7-31050-Monastier di Treviso (TV), Italy

EDITORIAL OFFICE

Jian-Xia Cheng, Director
World Journal of Radiology
Room 903, Building D, Ocean International Center, No. 62 Dongsihuan Zhonglu, Chaoyang District, Beijing 100025, China
Telephone: +86-10-59080039
Fax: +86-10-85381893
E-mail: wjr@wjgnet.com
<http://www.wjgnet.com>

PUBLISHING

Baishideng Publishing Group Co., Limited, Room 1701, 17/F, Henan Building, No.90 Jaffe Road, Wanchai, Hong Kong, China
Fax: +852-31158812
Telephone: +852-58042046

PUBLICATION DATE

January 28, 2012

COPYRIGHT

© 2012 Baishideng. Articles published by this Open-Access journal are distributed under the terms of the Creative Commons Attribution Non-commercial License, which permits use, distribution, and reproduction in any medium, provided the original work is properly cited, the use is non commercial and is otherwise in compliance with the license.

SPECIAL STATEMENT

All articles published in this journal represent the viewpoints of the authors except where indicated otherwise.

INSTRUCTIONS TO AUTHORS

Full instructions are available online at http://www.wjgnet.com/1949-8470/g_info_20100316162358.htm.

ONLINE SUBMISSION

<http://www.wjgnet.com/1949-8470office>



Value of MR contrast media in image-guided body interventions

Maythem Saeed, Mark Wilson

Maythem Saeed, Mark Wilson, Department of Radiology and Biomedical Imaging, University of California San Francisco, San Francisco, CA 94107-5705, United States

Author contributions: Saeed M contributed to the conception and design, acquisition of data, drafting the article, writing and revising it critically for intellectual content; Wilson M contributed to the acquisition of data, revising the article critically for intellectual content and approving the final version.

Correspondence to: Maythem Saeed, Professor of Radiology and Biomedical Imaging, Department of Radiology and Biomedical Imaging, University of California San Francisco, 185 Berry Street, Suite 350, Campus Box 0946, San Francisco, CA 94107-5705, United States. maythem.saeed@ucsf.edu

Telephone: +1-415-5146221 Fax: +1-415-3539423

Received: August 6, 2011 Revised: October 28, 2011

Accepted: November 4, 2011

Published online: January 28, 2012

Abstract

In the past few years, there have been multiple advances in magnetic resonance (MR) instrumentation, *in vivo* devices, real-time imaging sequences and interventional procedures with new therapies. More recently, interventionists have started to use minimally invasive image-guided procedures and local therapies, which reduce the pain from conventional surgery and increase drug effectiveness, respectively. Local therapy also reduces the systemic dose and eliminates the toxic side effects of some drugs to other organs. The success of MR-guided procedures depends on visualization of the targets in 3D and precise deployment of ablation catheters, local therapies and devices. MR contrast media provide a wealth of tissue contrast and allows 3D and 4D image acquisitions. After the development of fast imaging sequences, the clinical applications of MR contrast media have been substantially expanded to include pre- during- and post-interventions. Prior to intervention, MR contrast media have the potential to localize and delineate pathologic tissues of vital organs, such as the brain, heart, breast, kidney, prostate, liver and uterus. They also offer other options such as label-

ing therapeutic agents or cells. During intervention, these agents have the capability to map blood vessels and enhance the contrast between the endovascular guidewire/catheters/devices, blood and tissues as well as direct therapies to the target. Furthermore, labeling therapeutic agents or cells aids in visualizing their delivery sites and tracking their tissue distribution. After intervention, MR contrast media have been used for assessing the efficacy of ablation and therapies. It should be noted that most image-guided procedures are under preclinical research and development. It can be concluded that MR contrast media have great value in pre-clinical and some clinical interventional procedures. Future applications of MR contrast media in image-guided procedures depend on their safety, tolerability, tissue specificity and effectiveness in demonstrating success of the interventions and therapies.

© 2012 Baishideng. All rights reserved.

Key words: Magnetic resonance imaging; Contrast media; Magnetic resonance-guided interventions; Tissue ablation; Local therapy

Peer reviewers: Yahya Paksoy, MD, Professor, Department of Radiology, Selcuk University Meram School of Medicine, 42085 Konya, Turkey; Dr. Monvadi Barbara Srichai-Parsia, Department of Radiology and Medicine, NYU School of Medicine, 530 First Avenue, HCC-C48, New York 11211, United States

Saeed M, Wilson M. Value of MR contrast media in image-guided body interventions. *World J Radiol* 2012; 4(1): 1-12 Available from: URL: <http://www.wjgnet.com/1949-8470/full/v4/i1/1.htm> DOI: <http://dx.doi.org/10.4329/wjr.v4.i1.1>

INTRODUCTION

Image-guided procedures are a minimally invasive form of treatment for diseased vessels and organs. Catheters, devices and therapies are introduced into internal organs *via* different routes and can be guided by real-time

imaging. Image-guided procedures are consequently less invasive than surgical procedures and demonstrate similar patient outcomes^[1]. Recent percutaneous intervention studies showed steady increase in the usage of contrast media. Iodinated contrast media are routinely utilized in procedures guided by X-ray fluoroscopy and computed tomography, but these agents have nephrotoxic effects and require ionizing radiation to be visualized, which elevates cancer risk^[2,3].

In the early 1980 magnetic resonance (MR) contrast media were introduced. MR contrast media exhibit paramagnetic properties that lead to contrast enhancement by shortening the longitudinal (T₁) or transverse (T₂) relaxation times. These agents rapidly pass to the extracellular compartment and are quickly eliminated by glomerular filtration. Unlike iodinated contrast media, they do not require ionizing radiation to be visualized. These agents are pivotal for accurate disease detection, pathology characterization and treatment planning. MR contrast media provide a wealth of tissue contrast that can be manipulated by the acquisition sequences. Refinements in imaging sequences can reduce the required dose of MR contrast media. This editorial summarizes the important applications of MR contrast media in MR-guided interventions and therapies.

MR CONTRAST MEDIA

MR contrast media represent alternative diagnostic options in patients at risk for adverse reactions to iodinated contrast media. In the early phase of using MR contrast media, the main problem was their toxicity because investigators used pure paramagnetic heavy metal ions. Later paramagnetic ions were chelated with DTPA, DOTA or BOPTA to reduce their toxicity. The chelation, however, reduced some of the paramagnetic properties of free ions. MR contrast media improve diagnostic accuracy, tissue contrast and visibility of inflammation, necrosis, tumor and vascular plaques.

In the late 1980 and early 1990 the first gadolinium-chelate was approved for clinical routine. Currently, the FDA has approved several extracellular gadolinium-chelates and only one gadolinium-based intravascular agent (gadofosveset trisodium)^[4]. Other preclinical gadolinium-based intravascular media, which are used to extract physiologic and morphologic information are Gadomer 17^[5] and P792^[6]. Extravasation and elimination of intravascular contrast media are very slow compared with extracellular contrast media.

In general extracellular gadolinium chelate and blood pool iron oxide particle MR contrast media have been safely and successfully used in patients. In 2005 the observation of nephrogenic systemic fibrosis (NSF), however, cautioned the handling of gadolinium-based MR contrast media^[7,8]. NSF describes a systemic body collagenosis, most likely evoked by the deposition of gadolinium ions in the tissue. NSF was observed in patients with reduced renal function (eGFR < 30 mL/min) after the repeated injection of high doses of gadolinium-chelates^[7]. Besides

the dose, the chemical structure of the chelate (defining the complex stability) has a major impact in increasing the risk of developing NSF. Thus, there is a strong need to minimize the dose of MR contrast media, especially in interventional procedures, where patients are subjected to repeated contrast injections.

Classification of MR contrast media is based on: (1) their distribution in the tissue compartments, namely the extracellular compartment (low molecular weight; < 2 kDa), intravascular compartment (high molecular weight; > 50 kDa), or intracellular compartment or (2) their effects on longitudinal (T₁), transverse (T₂) relaxation times and susceptibility shift (T₂^{*}) of tissues and thereby change tissue signal intensity^[9,10]. While T₁ shortening increases signal intensity, T₂ shortening does the opposite. Extracellular or low molecular weight MR contrast media were widely used in interventional procedures, while intravascular or high molecular weight media, such as iron oxide particles, were used for cell labeling.

Iron oxide particles have been used as T₁ and T₂^{*} MR contrast media to increase and decrease signal intensity of the region of interest on magnetic resonance imaging (MRI). Due to their size and composition, the particles remain in the intravascular compartment for a prolonged period. This class of agents has a high safety index and is not associated with NSF. There are two types of iron particles: (1) superparamagnetic iron oxide particles; and (2) ultrasmall superparamagnetic iron oxide particles. These agents are promising since their properties can be tuned for specific applications, such as cell labeling, drug targeting^[11-13], tissue ablation^[14] and cancer therapy^[15]. They have also become MR markers of inflammatory and degenerative disorders associated with a high macrophage phagocytic activity^[16].

APPLICATIONS OF MR CONTRAST MEDIA IN BODY INTERVENTIONS

Endovascular catheters and devices

A considerable research effort is directed at improving the detection of vascular disease with different imaging modalities, such as X-ray, computed tomography, intravascular ultrasound and MR angiography. Because of lack of harmful radiation and high soft tissue contrast, MR angiography is considered the most patient-friendly among these techniques. The main challenge for MR angiography is derived from the fact that the signal originates from water protons, which are abundant in the body. Inevitably, this leads to a background signal in the image and the blood pool cannot exclusively be seen.

Clinical and experimental studies showed that contrast enhanced MR angiography is possible for a selective and exclusive visualization of the vasculature. Delivering MR contrast media during catheter navigation can reduce image blurring and artifacts resulting from the movement of flowing blood, which allows for reaching the steady state earlier. Endovascular catheters and devices appear as dark objects in these cases. Furthermore, intravenous

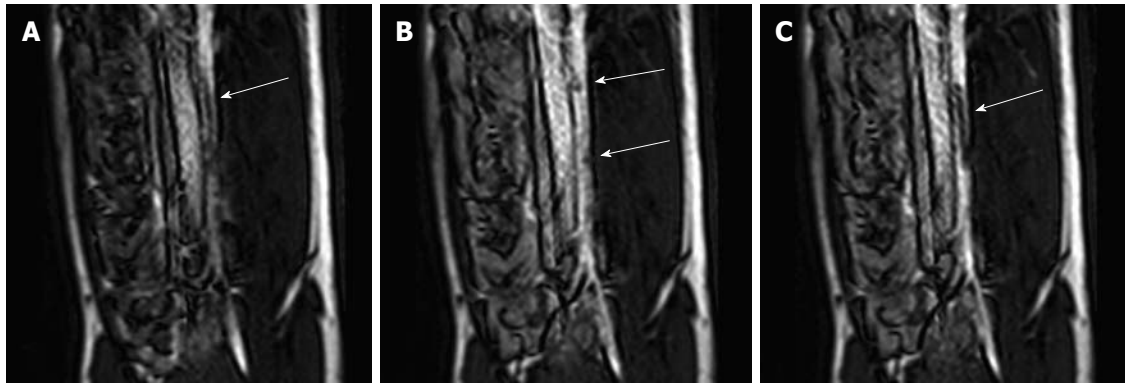


Figure 1 Selected magnetic resonance-guided images of the abdominal aorta prior to the administration of intravascular gadolinium-based (T1 enhancing agent) magnetic resonance contrast medium, the inflated balloon on the catheter is evident (arrow), but suffers substantial downstream signal loss (A). After a blood pool magnetic resonance (MR) contrast medium administration (B), the MR dysprosium-chelate (markers placed on the catheter shaft) becomes evident (arrows, B) and, following inflation, the spatial extent of the balloon is better delineated (arrow, C).

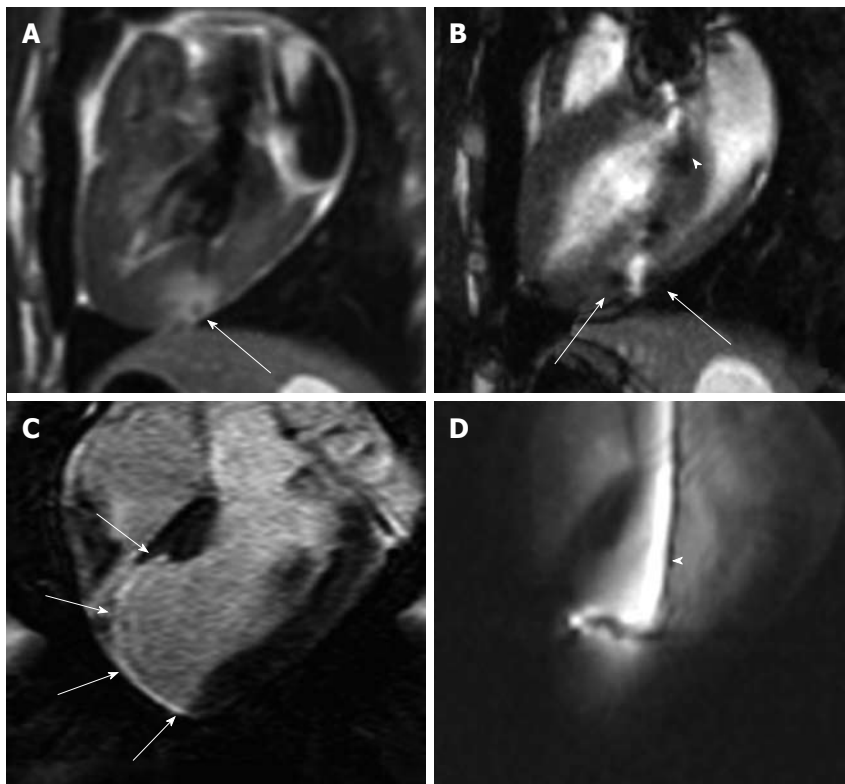


Figure 2 Gadolinium-based magnetic resonance contrast media (T1 enhancing agent) have been used for multiple purposes in cardiac interventions. A: These agents (at a low concentration) have been used to create a target in the myocardium; B: Gadolinium oxide powder was used to coat the endovascular catheter to facilitate navigation into the LV (white arrowhead); C: Magnetic resonance (MR) contrast medium was also used for enhancing and measuring the target (myocardial infarct) (white arrows); D: Selected MR-guided images show an active catheter hitting the infarcted target.

injection of MR contrast media during vascular intervention ensures procedure safety by enhancing the contrast between the vascular wall and endovascular catheter^[17] (Figure 1) and may prevent vascular perforation^[18]. Investigators coated the shaft and tip of endovascular catheters with either T₂* or T₁^[19,20] MR contrast media to enhance the contrast between the blood pool and endovascular catheter, in which the devices appear either hypoenhanced or hyperenhanced based on the sequence and contrast media.

Defining targets

A central challenge for the field of local therapy in tumors and cardiovascular diseases is the capability to visualize the catheter, target and targeting penumbra. MR contrast media showed promising results in visualizing, sizing and targeting penumbra (Figure 2), thereby allowing the interventionalists to determine the dose of the therapy based on size of the pathology. Furthermore, mixing MR contrast media with therapies may assist in ensuring tissue delivery and track its distribution over

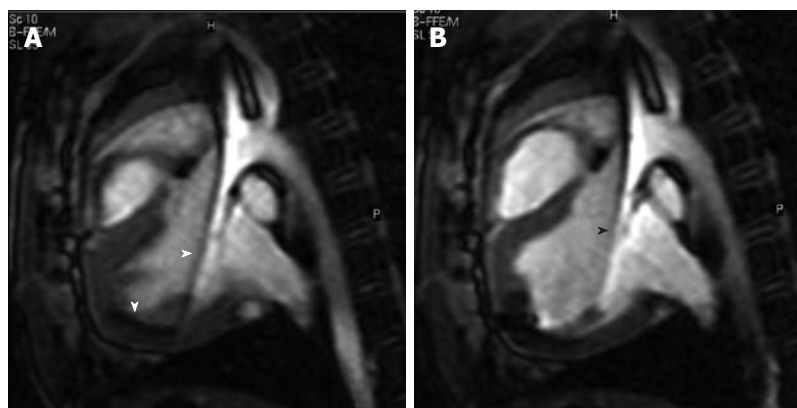


Figure 3 Selected magnetic resonance-guided images showing the advancement of a passive injecting catheter (arrowheads) in the left ventricle prior to (A) and after injecting dysprosium-chelate (T2* enhancing agent) magnetic resonance contrast medium (B, arrowhead) to ensure delivery in the targeted myocardium.

time (Figures 2 and 3).

MR contrast media are useful in evaluating the efficacy of therapy by allowing the determination of tissue perfusion, blood volume, vascular permeability, angiogenesis and cellular integrity^[21,22]. For example, after effective chemotherapy there is a decrease in the size of the lesion and number of microvessels, which can be detected on contrast enhanced MR images.

Body Interventions

Transcatheter embolization of the uterine arteries for treatment of uterine fibroids was introduced 1995 in France and has been performed in the United States since 1996. This technique is currently used for treatment of symptomatic uterine fibroids^[23] and hepatocellular tumors^[24]. The standard protocol for evaluation of this intervention consists of dynamic gadolinium-enhanced 3D pelvic MR angiography and delayed contrast enhanced MRI^[25]. Prior to transcatheter embolization of the uterine arteries, contrast enhanced MRI is performed to confirm the diagnosis, map (determine the size, number and location of the pathology), predict treatment response (high signal intensity associated with poor response) and road-map the pelvic vasculature^[26]. Embolization follow up showed that the procedure was successful when fibroids were unenhanced and the uterine arteries were invisible on perfusion MRI^[27]. In a rabbit tumor model, Chung *et al.*^[28] used intra-arterial bolus injection of gadolinium-based MR contrast medium to measure uterine fibroid perfusion before and after uterine artery embolization. After positioning a catheter within the uterine artery and injecting the microemboli, they found that uterine tumor perfusion decreased by 76% on MRI. Others found that patchy perfusion suggests incomplete uterine artery occlusion and treatment failure^[29,30]. This contrast enhanced MRI technique could be used to determine an optimal embolic endpoint with the long-term goals of improving uterine artery embolization success rates and minimizing procedure-related ischemic pain.

A major limitation of transcatheter arterial embolization is the inability to image and determine the *in vivo*

fate of the injected emboli. Assessment of embolization relies on interpretation of visual blood flow information^[23,31] and operator inferences. The limitations of transcatheter arterial embolization were demonstrated in a study probing the perceived and real completeness of uterine fibroid embolization. Investigators found incomplete embolization in 20% of cases despite indications by angiography of complete occlusion. They also found that incomplete embolization of uterine fibroids has led to tumor recurrence and persistence of symptoms^[32], while exceeding the endpoint by injecting too much embolic material increases the chances of uterine damage^[31]. Until recently, there has been no noninvasive technique to track/map the distribution of embolic materials after intervention, which represents a significant disadvantage. Therefore, Fidelman *et al.*^[33] impregnated the embolic materials (300-500 and 500-700 μm in diameters) with gadolinium-chelate by diffusion of the contrast medium into the core of the porous particles to visualize their distribution. Wilson *et al.*^[34] used these impregnated embolic materials in visualizing the obstruction of different diameter blood vessels in the kidneys. These materials provided wave-front renal enhancement for > 1 h after injection. Large microemboli preferentially deposited in the medulla, while small microemboli deposited in the cortex. Renal blood flow was significantly reduced after the administration of 300-500 μm microspheres (from 3.9 to 1.0 mL/min per gram) and 500-700 μm microspheres (from 3.5 to 0.2 mL/min per gram)^[34] (Figure 4).

In 2008, Cilliers *et al.*^[35] synthesized and characterized polyvinyl alcohol embolic particles modified with a clinically approved gadolinium-chelate MR contrast media. The investigators used these particles during transcatheter arterial embolization procedures. The polyvinyl alcohol particles are injected into tumor vessels and prevent blood flow, which results in tumor attenuation. They found that MRI of embolic particles facilitate determination of the endpoint of embolization, observe nontarget embolization, and improve the success rate of the procedure.

In 2011, Bartling *et al.*^[36] presented embolization con-

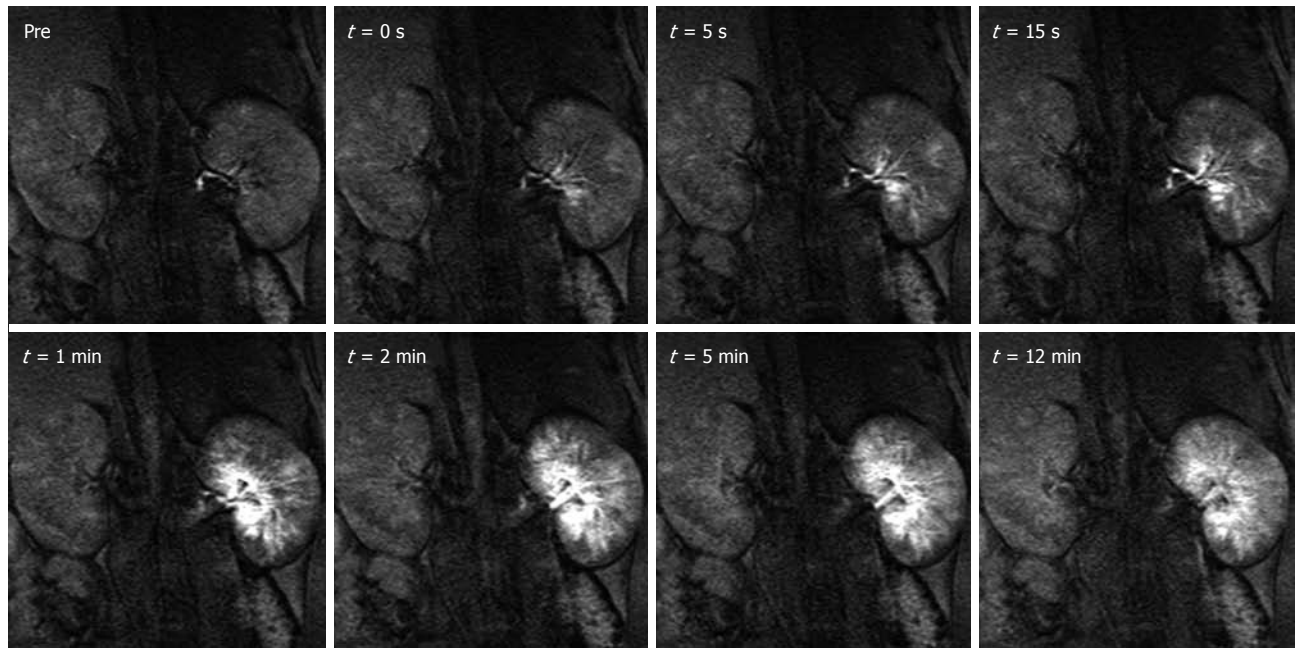


Figure 4 Distribution of magnetic resonance labeled embolic materials as a function of time in the left kidney. Gadolinium-impregnated microspheres caused a steep increase in signal intensity over the cortical and medullary regions. Less than 5 min after the injection, as excess free gadolinium was excreted in the urine, the signal intensities began to decrease but still remained substantially above baseline for both particle sizes. Administration of magnetic resonance contrast media after the procedure confirmed the hypothesis that the injection of microspheres halts blood flow to targeted tissues. Hyperenhanced foci corresponding to microsphere location persisted for at least 1hr after injections. The smaller particles tended to settle more peripherally in the renal cortex, whereas the larger microspheres were lodged in the inner cortical and medullary regions. This new labeling technique may be useful for embolotherapy procedures, such as uterine fibroid embolization, hepatic tumor embolization, and preoperative meningioma embolization.

trast media with a property of being visible on MRI and X-ray/computed tomography, namely iodine and iron particles. They proposed that implementation of this new material in clinical radiology will provide optimization of embolization procedures with regard to prevention of particle misplacement and direct intraprocedural visualization, while improving follow-up examinations by utilizing the complementary characteristics of CT and MRI.

An important clinical application of MR contrast media is that shown by Wilson *et al*^[34], where patients with inoperable hepatocellular carcinoma were successfully treated using iron particles bound to doxorubicin. The particles ranged from 0.5-5.0 μm in diameter and were able to leave the vasculature under the influence of the force provided by the external magnet. Once the particles are outside the vasculature, doxorubicin desorbs from them, resulting in a local response with no systemic toxicity. Figures 5 and 6 show the setting of this clinical trial. Drug-bound iron particles can be precisely directed to selective organs by placement of an external magnet. In this study, MR contrast media showed the need for more therapy because of the lack of coverage of the entire tumor in the initial administration. MR images obtained after each dose of the chemotherapeutic agent showed increasing areas of signal intensity loss due to a magnetic susceptibility artifact caused by the iron.

Tissue ablation

Thermal ablation therapies (radiofrequency ablation, interstitial laser thermotherapy, microwave, cryotherapy and

high-intensity focused ultrasound) are minimally invasive or non-invasive alternatives to conventional surgical resection. Ablation has been widely implemented in treating arrhythmia in the heart and tumors in the prostate, lung, liver, kidneys, *etc.* Contrast enhanced MRI has been successfully used to assess the success of ablation^[37-39]. The diagnostic benefits of MR contrast media in differentiating ablated from non-ablated tissue have been confirmed in multiple centers^[40,41]. Prior to the administration of MR contrast media, the appearance of thermally ablated tissue varies between hypointense, isointense and hyperintense. After ablation, MR contrast media provide moderate to intense enhancement of the rim surrounding the thermally ablated tissue. In a prostate cancer study, RFA ablated lesions appear hypoenhanced after gadolinium injection^[42]. Similarly, Goldberg and Dupuy observed a lack of contrast enhancement after gadolinium injection in ablated liver metastasis^[43]. Accordingly, changes in signal intensity, size, and internal contours of ablated tissue on contrast enhanced MRI gives important clues about the success of therapy^[44].

Contrast enhanced MRI is also useful for arrhythmic substrate identification^[45,46]. This technique has the ability to encompass the target volume through direct imaging of signal enhancement after tissue ablation in patients^[47]. Clinical studies have demonstrated the association between infarct scar, peri-infarcted zone and the risk of monomorphic ventricular tachycardia^[46,48,49]. An integrated 3D scar reconstruction from delayed gadolinium-enhanced MRI was used to facilitate ventricular tachycar-

Magnetically targeted carrier (MTC-DOX)

1-2 μm Fe-activated carbon complexes bound to doxorubicin

Delivered through arterial catheter

Drawn into tissue by portable external magnet

Readily visible on MRI (Fe susceptibility artifact)

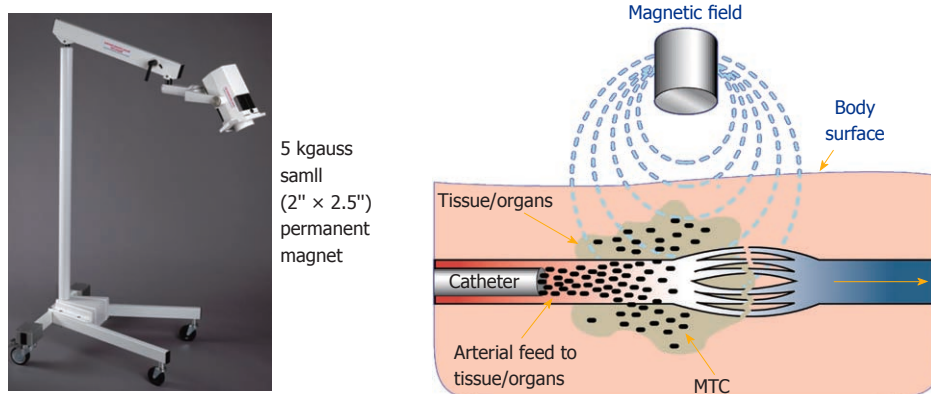


Figure 5 This figure shows a portable magnet (left) and a diagram (right) depicts the mode of action of magnetic targeted therapy in the target. The overall height of the magnet and holding apparatus is 1.4 m. The intra-arterial injected magnetic targeted carrier (iron particles) bound to doxorubicin (MTC-DOX), which is drawn out of the artery into surrounding tumor and/or liver tissue by the influence of the local magnetic field (Image courtesy of FeRx.). MRI: Magnetic resonance imaging.

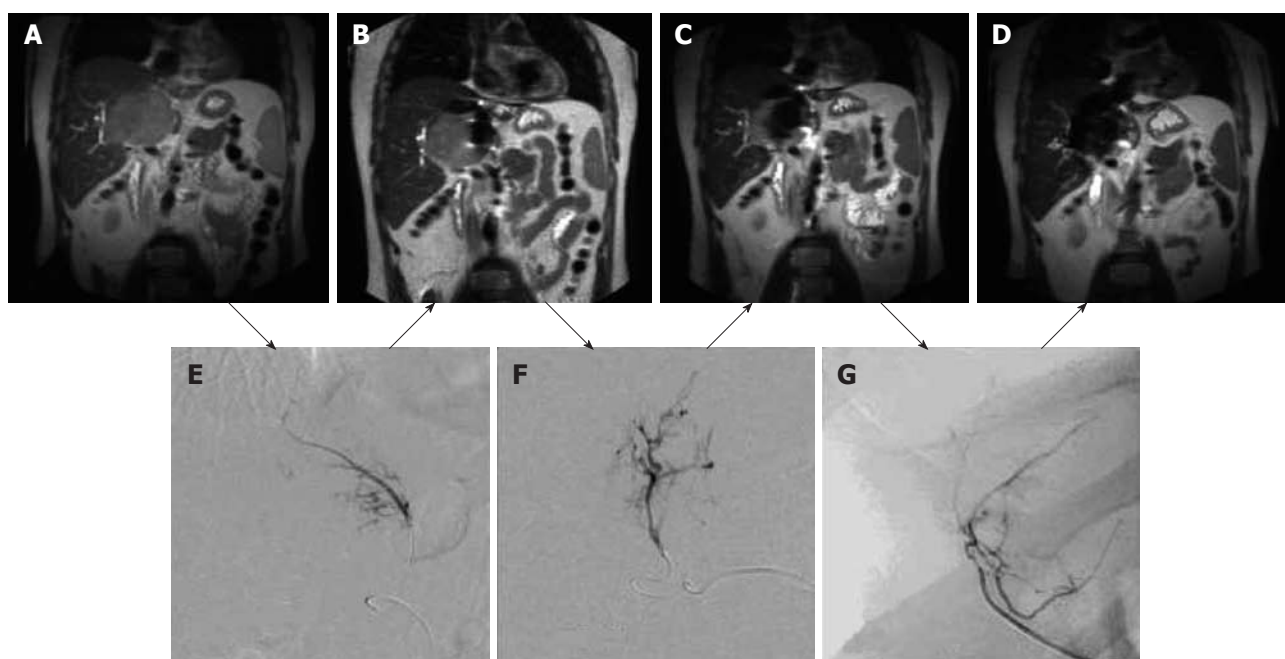


Figure 6 Coronal magnetic resonance images of large hepatocellular carcinoma obtained before magnetic targeted carrier bound to doxorubicin administration (A) and after the first (B), second (C) and third (D) dose of magnetic targeted carrier bound to doxorubicin. The selective hepatic arterial catheter was repositioned between each dose. The initial DSA image (E) was obtained during the injection of magnetic targeted carrier bound to doxorubicin (MTC-DOX) into the left hepatic artery supplying the tumor. The next dose was injected into the hepatic artery branch segment (F), while the third dose was injected into a branch of the right hepatic artery (G). As a result, progressively larger areas of the tumor were affected by MTC-DOX, as documented by the progressive loss of signal intensity due to iron susceptibility artifacts (T_2^*) on the intra-procedural coronal magnetic resonance images obtained after each injection.

dia ablation^[50]. van Dockum *et al*^[51] evaluated myocardial infarction induced by percutaneous transluminal septal myocardial ablation in symptomatic patients with hypertrophic obstructive cardiomyopathy using contrast-enhanced MRI.

Device deployment

A recent experimental study showed the value of MR

contrast media in providing diagnostic information on an atrial septal defect, a congenital heart defect in which the wall that separates the atria does not close completely. Schalla *et al*^[52] found in an experimental study that gadolinium-filled balloon sizing is a useful method for detecting and sizing the atrial septal defects. They also used MR contrast media to demonstrate intracardiac left-to-right shunt prior to the placement of atrial septal defect device

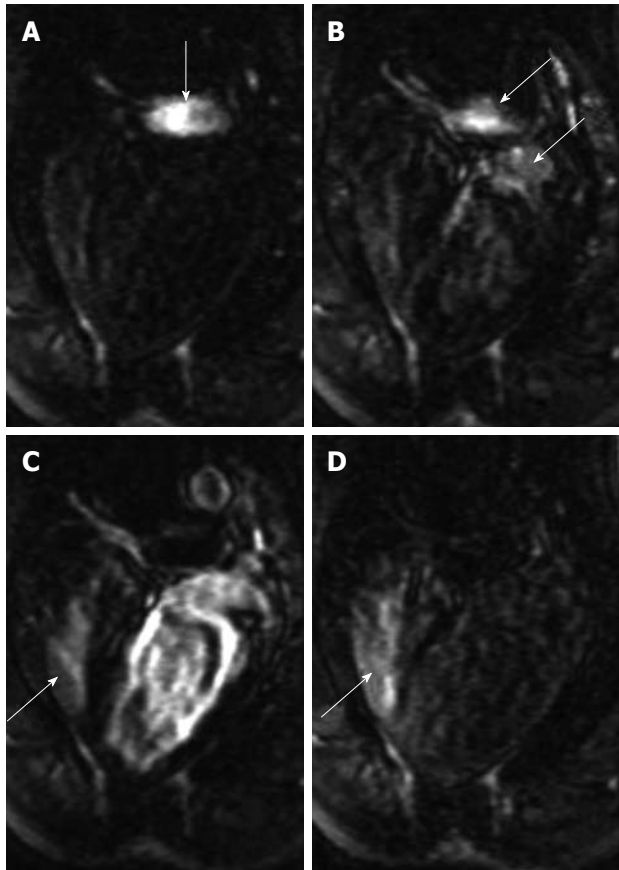


Figure 7 Bolus administration of gadolinium-chelate demonstrates atrial septal defect on cardiac magnetic resonance four-chamber view images. At the time of administration of the contrast medium, the right atrium was enhanced (A, arrow). Images acquired 1-2 s later show the contrast medium in both the pulmonary artery and left atrium (B, arrows) and subsequently in both right (arrow) and left ventricles (C). As a sign of an intracardiac left-to-right shunt, enhancement of the right ventricle is detected simultaneously with enhancement of the left ventricle. The re-enhancement of the right ventricle (D, arrow) as a result of recirculation of the contrast medium was acquired 12 s after image A.

closure, where contrast enhancement of the right ventricle is detected simultaneously with enhancement of the LV (Figure 7).

Therapy

Transendocardial and transvascular routes have been recently used to deliver MR labeled gene and cell therapies. The advantages of labeled therapies are: (1) targeting only pathologic regions; (2) delivering effective doses; and (3) reducing systemic side effects compared with IV injection^[53-55]. Unlike intramyocardial injection, intracoronary artery injection of stem cells causes microinfarct, which was confirmed by increase in serum troponin I concentration and electrophysiologic abnormalities detected on electrocardiogram^[56]. Recent MR and MDCT studies showed the effectiveness of MR and CT contrast media in detecting and measuring microinfarct size^[57,58].

MR contrast media showed great promise in detecting specific biological processes involved in the initiation and progression of atherosclerosis that may require intravascular intervention^[59,60]. von Bary *et al.*^[61] experimentally demonstrated the feasibility of noninvasive assessment of

coronary remodeling, using elastin-binding gadolinium. Such data could facilitate the interpretation of clinical findings, enhance risk stratification and provide a means for local therapy. Monitoring extracellular matrix changes by contrast-enhanced MRI appears promising for the assessment of plaque burden in atherosclerosis or neointimal hyperplasia after coronary angioplasty and other therapies^[62].

MR contrast media have also been used in quantifying the sizes of the area at risk, myocardial infarct and visualizing therapeutic delivery in the target. Saeed *et al.*^[63] used MR contrast media in measuring ischemic and infarcted myocardium prior to and after transendocardial delivery of hepatocyte growth factor gene and endothelial growth factor gene using MR-guided procedures. They found that gene treated animals have better perfusion and significantly smaller infarct size than control animals on contrast enhanced MRI (Figure 8).

MR contrast media have also been used to label cells in order to track their distribution in myocardium after intramyocardial injection under MR-guidance^[64] or intracoronary infusion^[65,66]. Graham *et al.*^[66] were able to follow the distribution of iron oxide labeled bone marrow progenitor cells for 42 d after intracoronary infusion. The transendocardial delivery route has been shown to be safe in patients with end-stage heart failure^[67]. Recent preclinical and clinical studies showed the importance of MR contrast media in determining the efficacy of stem cells^[68-70]. First pass MR contrast media passage documented the benefits of angiogenic growth factors^[71] and angiogenic genes^[72] in increasing regional myocardial perfusion (Figure 9). Pearlman *et al.*^[71] were the first to demonstrate the recruitment of collateral vessels after local delivery of angiogenic genes, using perfusion MRI.

Angiography

Visualization of vascular anatomy, pathology (stenosis, aneurism, plaque) or implants (stents, filters, atrio-septal occluders or prosthetic heart valves) is crucial in interventional procedures. MR contrast media have been used in road mapping blood vessels^[73,74], demonstrating vascular diseases and easing visualization of endovascular devices^[21]. These agents were delivered intravenously or intraarterially to enhance arterial^[74,75] or venous vessels^[76].

Inflammation is a key process in atherosclerotic progression and has been associated with increased frequency of plaque rupture^[77]. Ultrasmall superparamagnetic iron oxide particles have been used in characterizing atherosclerotic plaques from many different perspectives. These agents are effective markers of plaque inflammation. Different plaque tissues can then be characterized based on their enhancement properties^[78].

Cell labeling

Both gadolinium and iron oxide based contrast media are useful for labeling different types of cells that assist in cell tracking^[79,80]. These agents have no negative effects on cell viability, proliferation or differentiation^[81,82]. The toxicity of iron oxide particles is less than free gadolinium because free iron particles released from dead iron

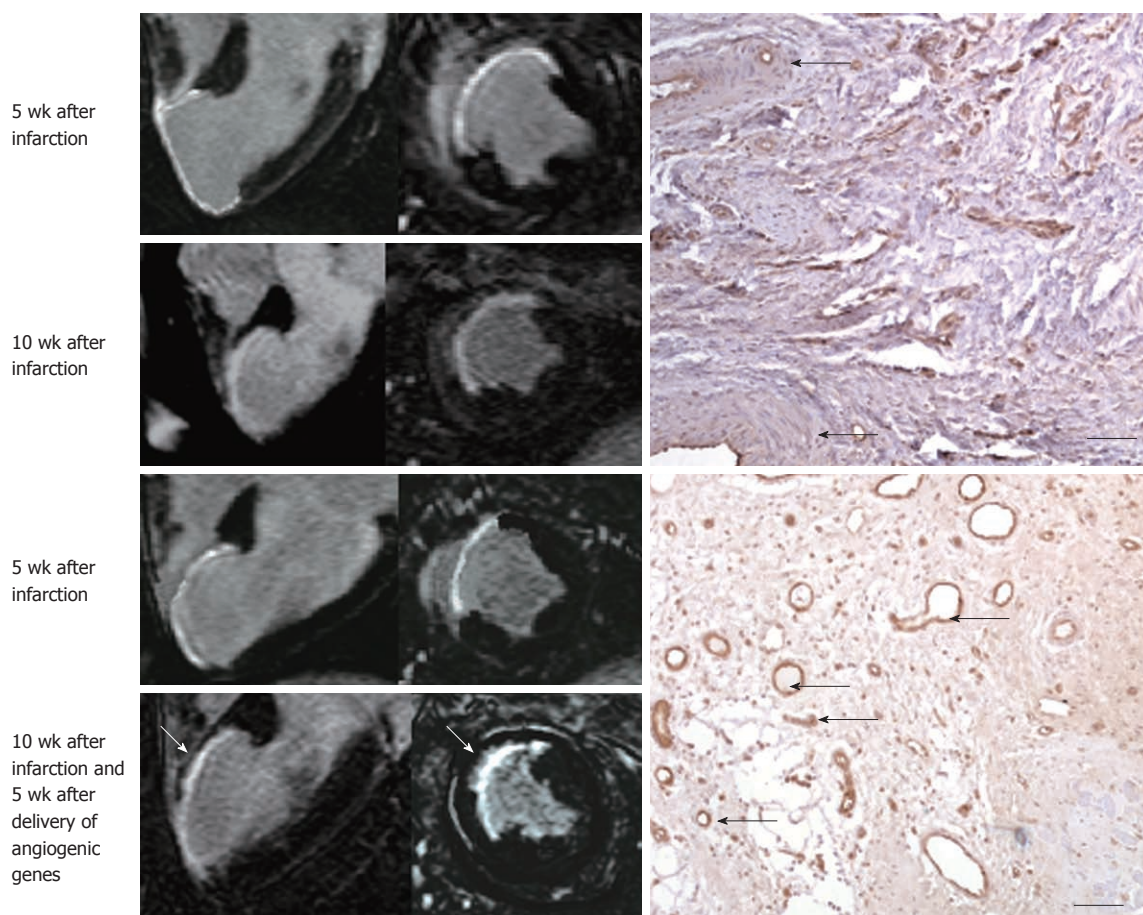


Figure 8 Gadolinium-enhanced magnetic resonance long-axis (left column) and short-axis (right column) images illustrate the extent of myocardial infarct (hyperenhanced myocardium) at 5 wk after infarction and 5 wk after injection of saline (top block, 4 magnetic resonance images) and angiogenic gene (bottom block, 4 magnetic resonance images). Gadolinium-enhanced magnetic resonance (MR) images delineated myocardial infarct and showed substantial reduction in infarct extent and transmural extent 5 wk after treatment (bottom block, bottom row, white arrows) compared with control animal (top block, bottom row). The angiogenic gene was delivered transendocardially under MR-guidance as shown in Figure 2. The histopathologic sections (right) show very few blood vessels in control animal (top right, black arrows) and the formation of abundant new blood vessels in gene treated animal (bottom right, black arrows).

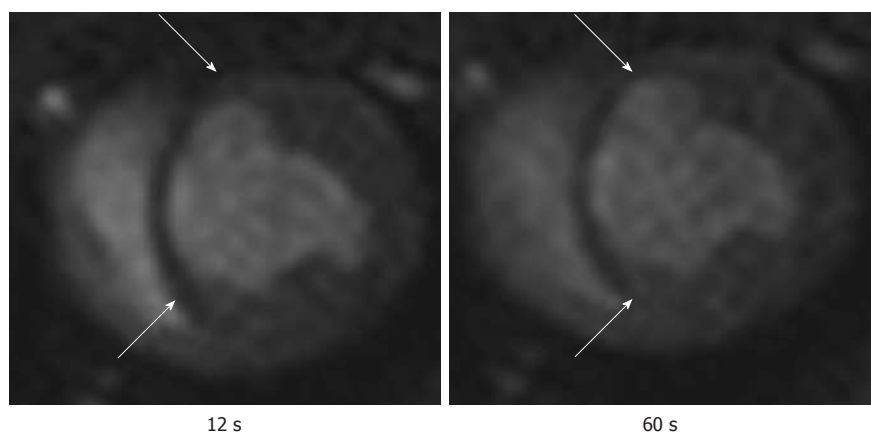


Figure 9 First pass perfusion magnetic resonance imaging shows the hypoperfused infarct scar (arrows) after bolus administration of Gd-DTPA. The magnetic resonance (MR) images illustrate the delay in the enhancement of infarcted myocardium (arrows) compared with remote myocardium. The images were acquired at 12 s (left) and 60 s (right) after bolus administration of MR contrast media.

labeled cells are recycled in the body and not associated with NSF.

MR contrast media can be introduced into the intracellular compartments by endocytosis, phagocytosis or magnetoelectroporation. Investigators found that the

duration of detection of labeled cells on MRI varies from 5 wk for embolic stem cells^[83] to 16 wk for skeletal myoblasts^[84]. Modo *et al*^[85] observed that gadolinium chelate labeling allows *in vivo* identification of transplanted neural cells up to 1 year after transplantation in rats with

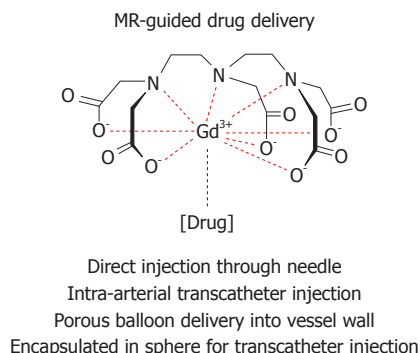


Figure 10 Schematic representation of magnetic resonance labeled therapy and their routes of delivery.

middle cerebral artery occlusion. Bulte *et al.*^[86] found that the reliable detection limit of a cluster of iron oxide-labeled cells in beating hearts at clinical field strengths is on the order of 100 000 cells. Iron labeling of stem cells generates a hypointense signal (dark region), related to the susceptibility effect of the particles, on T2*-weighted images. Iron oxide particles provide T2* parametric map for up to 3 wk^[79,86,87]. In the future, accurate depiction of treated regions with MR labeled cells may permit rapid adjustments of the therapeutic regimen to improve clinical outcomes.

FUTURE PERSPECTIVES

The usage of MR contrast media in MR guided procedures represents a promising modality, beyond traditional anatomical and functional indices. Figure 10 shows a schematic presentation of MR labeled therapy and their routes of delivery.

Saeed *et al.*^[21] demonstrated the advantageous effects of vascular endothelial growth factor and hepatocyte growth factor genes, delivered transendocardially under MR-guidance, in creating new blood vessels and reducing the size of infarcted myocardium using gadolinium-based MR contrast media^[22]. Others used contrast enhanced MRI for determining the effects of intracoronary stem cell therapy on left ventricular function^[88]. The investigators did not observe evidence of positive effects for intracoronary stem cells compared with placebo therapy with respect to left ventricular ejection fraction, volume indexes or infarct size. Other investigators found intracoronary cell delivery cause microinfarction^[50]. MR contrast media have been recently used to visualize myocardial microinfarct caused by coronary microemboli^[57,58] and in the validation of manual thrombectomy devices^[89]. Technical developments in mid-field MR interventional units will lead to reduction of the dose of MR contrast media and result in better visualization of interventional devices.

CONCLUSION

MR contrast media are useful in interventional procedures and therapy evaluation. They allow for character-

ization of tissue and vascular pathologies. In the follow-up they allow for monitoring of treatment success that is not available on X-ray fluoroscopy and limits the harmful effects of iodinated contrast media. Labeling therapies with MR contrast media may be the future development that will hasten the deployment of effective therapies.

REFERENCES

- 1 Chertova E, Chertov O, Coren LV, Roser JD, Trubey CM, Bess JW, Sowder RC, Barsov E, Hood BL, Fisher RJ, Nagashima K, Conrads TP, Veenstra TD, Lifson JD, Ott DE. Proteomic and biochemical analysis of purified human immunodeficiency virus type 1 produced from infected monocyte-derived macrophages. *J Virol* 2006; **80**: 9039-9052
- 2 Wagner LK, Eifel P, Geise R. Effects of ionizing radiation. *J Vasc Interv Radiol* 1995; **6**: 988-989
- 3 Zhou W, Parent LJ, Wills JW, Resh MD. Identification of a membrane-binding domain within the amino-terminal region of human immunodeficiency virus type 1 Gag protein which interacts with acidic phospholipids. *J Virol* 1994; **68**: 2556-2569
- 4 Freed EO. HIV-1 Gag: flipped out for PI(4,5)P(2). *Proc Natl Acad Sci USA* 2006; **103**: 11101-11102
- 5 Saad JS, Miller J, Tai J, Kim A, Ghanam RH, Summers MF. Structural basis for targeting HIV-1 Gag proteins to the plasma membrane for virus assembly. *Proc Natl Acad Sci USA* 2006; **103**: 11364-11369
- 6 Hermida-Matsumoto L, Resh MD. Human immunodeficiency virus type 1 protease triggers a myristoyl switch that modulates membrane binding of Pr55(gag) and p17MA. *J Virol* 1999; **73**: 1902-1908
- 7 Naghavi MH, Goff SP. Retroviral proteins that interact with the host cell cytoskeleton. *Curr Opin Immunol* 2007; **19**: 402-407
- 8 Tomita Y, Noda T, Fujii K, Watanabe T, Morikawa Y, Kawakawa Y. The cellular factors Vps18 and Mon2 are required for efficient production of infectious HIV-1 particles. *J Virol* 2011; **85**: 5618-5627
- 9 Dong X, Li H, Derdowski A, Ding L, Burnett A, Chen X, Peters TR, Dermody TS, Woodruff E, Wang JJ, Spearman P. AP-3 directs the intracellular trafficking of HIV-1 Gag and plays a key role in particle assembly. *Cell* 2005; **120**: 663-674
- 10 Camus G, Segura-Morales C, Molle D, Lopez-Vergès S, Begon-Pescia C, Cazeville C, Schu P, Bertrand E, Berlioz-Torrent C, Basyuk E. The clathrin adaptor complex AP-1 binds HIV-1 and MLV Gag and facilitates their budding. *Mol Biol Cell* 2007; **18**: 3193-3203
- 11 Parent LJ. New insights into the nuclear localization of retroviral Gag proteins. *Nucleus* 2011; **2**: 92-97
- 12 Dupont S, Sharova N, DéHoratius C, Virbasius CM, Zhu X, Bukrinskaya AG, Stevenson M, Green MR. A novel nuclear export activity in HIV-1 matrix protein required for viral replication. *Nature* 1999; **402**: 681-685
- 13 Jouvenet N, Bieniasz PD, Simon SM. Imaging the biogenesis of individual HIV-1 virions in live cells. *Nature* 2008; **454**: 236-240
- 14 Hadjipanayis CG, Bonder MJ, Balakrishnan S, Wang X, Mao H, Hadjipanayis GC. Metallic iron nanoparticles for MRI contrast enhancement and local hyperthermia. *Small* 2008; **4**: 1925-1929
- 15 Pornillos O, Ganer-Pornillos BK, Kelly BN, Hua Y, Whitby FG, Stout CD, Sundquist WI, Hill CP, Yeager M. X-ray structures of the hexameric building block of the HIV capsid. *Cell* 2009; **137**: 1282-1292
- 16 Cortines JR, Monroe EB, Kang S, Prevelige PE. A retroviral chimeric capsid protein reveals the role of the N-terminal β -hairpin in mature core assembly. *J Mol Biol* 2011; **410**: 641-652

- 17 **Paillart JC**, Shehu-Xhilaga M, Marquet R, Mak J. Dimerization of retroviral RNA genomes: an inseparable pair. *Nat Rev Microbiol* 2004; **2**: 461-472
- 18 **Saeed M**, Henk CB, Weber O, Martin A, Wilson M, Shunk K, Saloner D, Higgins CB. Delivery and assessment of endovascular stents to repair aortic coarctation using MR and X-ray imaging. *J Magn Reson Imaging* 2006; **24**: 371-378
- 19 **Wyma DJ**, Jiang J, Shi J, Zhou J, Lineberger JE, Miller MD, Aiken C. Coupling of human immunodeficiency virus type 1 fusion to virion maturation: a novel role of the gp41 cytoplasmic tail. *J Virol* 2004; **78**: 3429-3435
- 20 **Unal O**, Li J, Cheng W, Yu H, Strother CM. MR-visible coatings for endovascular device visualization. *J Magn Reson Imaging* 2006; **23**: 763-769
- 21 **Saeed M**, Martin A, Jacquier A, Bucknor M, Saloner D, Do L, Ursell P, Su H, Kan YW, Higgins CB. Permanent coronary artery occlusion: cardiovascular MR imaging is platform for percutaneous transcatheter delivery and assessment of gene therapy in canine model. *Radiology* 2008; **249**: 560-571
- 22 **Zhang H**, Zhao Q, Bhattacharya S, Waheed AA, Tong X, Hong A, Heck S, Curreli F, Goger M, Cowburn D, Freed EO, Debnath AK. A cell-penetrating helical peptide as a potential HIV-1 inhibitor. *J Mol Biol* 2008; **378**: 565-580
- 23 **Adamson CS**, Freed EO. Novel approaches to inhibiting HIV-1 replication. *Antiviral Res* 2010; **85**: 119-141
- 24 **Castrucci M**, Sironi S, De Cobelli F, Salvioni M, Del Maschio A. Plain and gadolinium-DTPA-enhanced MR imaging of hepatocellular carcinoma treated with transarterial chemoembolization. *Abdom Imaging* 1996; **21**: 488-494
- 25 **Mueller GC**, Gemmete JJ, Carlos RC. Diagnostic imaging and vascular embolization for uterine leiomyomas. *Semin Reprod Med* 2004; **22**: 131-142
- 26 **Kelly BN**, Kyere S, Kinde I, Tang C, Howard BR, Robinson H, Sundquist WI, Summers MF, Hill CP. Structure of the antiviral assembly inhibitor CAP-1 complex with the HIV-1 CA protein. *J Mol Biol* 2007; **373**: 355-366
- 27 **Freed EO**. HIV-1 and the host cell: an intimate association. *Trends Microbiol* 2004; **12**: 170-177
- 28 **Chung JC**, Wang D, Lewandowski RJ, Tang R, Chrisman HB, Vogelzang RL, Woloschak GE, Larson AC, Omary RA, Ryu RK. Four-dimensional transcatheter intra-arterial perfusion MR imaging before and after uterine artery embolization in the rabbit VX2 tumor model. *J Magn Reson Imaging* 2010; **31**: 1137-1143
- 29 **Pornillos O**, Alam SL, Davis DR, Sundquist WI. Structure of the Tsg101 UEV domain in complex with the PTAP motif of the HIV-1 p6 protein. *Nat Struct Biol* 2002; **9**: 812-817
- 30 **Liu F**, Stephen AG, Waheed AA, Aman MJ, Freed EO, Fisher RJ, Burke TR. SAR by oxime-containing peptide libraries: application to Tsg101 ligand optimization. *ChemBiochem* 2008; **9**: 2000-2004
- 31 **Huang JY**, Kafy S, Dugas A, Valenti D, Tulandi T. Failure of uterine fibroid embolization. *Fertil Steril* 2006; **85**: 30-35
- 32 **Dorenberg EJ**, Novakovic Z, Smith HJ, Hafsahl G, Jakobsen JA. Uterine fibroid embolization can still be improved: observations on post-procedure magnetic resonance imaging. *Acta Radiol* 2005; **46**: 547-553
- 33 **Fidelman N**, Wilson MW, Weber OM, Martin AJ, Kerlan RK, LaBerge JM, Gordon RL. Real-time MR properties of particulate embolic agents tested in a dynamic flow model. *J Vasc Interv Radiol* 2002; **13**: 613-618
- 34 **Wilson MW**, Fidelman N, Weber OM, Martin AJ, Gordon RL, LaBerge JM, Kerlan RK, Wolanske KA, Saeed M. Experimental renal artery embolization in a combined MR imaging/angiographic unit. *J Vasc Interv Radiol* 2003; **14**: 1169-1175
- 35 **Cilliers R**, Song Y, Kohlmeir EK, Larson AC, Omary RA, Meade TJ. Modification of embolic-PVA particles with MR contrast agents. *Magn Reson Med* 2008; **59**: 898-902
- 36 **Bartling SH**, Budjan J, Aviv H, Haneder S, Kraenzlin B, Michaely H, Margel S, Diehl S, Semmler W, Gretz N, Schönb erg SO, Sadick M. First multimodal embolization particles visible on x-ray/computed tomography and magnetic resonance imaging. *Invest Radiol* 2011; **46**: 178-186
- 37 **Carrillo A**, Duerk JL, Lewin JS, Wilson DL. Semiautomatic 3-D image registration as applied to interventional MRI liver cancer treatment. *IEEE Trans Med Imaging* 2000; **19**: 175-185
- 38 **Quesson B**, de Zwart JA, Moonen CT. Magnetic resonance temperature imaging for guidance of thermotherapy. *J Magn Reson Imaging* 2000; **12**: 525-533
- 39 **Salomir R**, Vimeux FC, de Zwart JA, Grenier N, Moonen CT. Hyperthermia by MR-guided focused ultrasound: accurate temperature control based on fast MRI and a physical model of local energy deposition and heat conduction. *Magn Reson Med* 2000; **43**: 342-347
- 40 **Bruix J**, Sherman M, Llovet JM, Beaugrand M, Lencioni R, Burroughs AK, Christensen E, Pagliaro L, Colombo M, Rodés J. Clinical management of hepatocellular carcinoma. Conclusions of the Barcelona-2000 EASL conference. European Association for the Study of the Liver. *J Hepatol* 2001; **35**: 421-430
- 41 **Forner A**, Ayuso C, Varela M, Rimola J, Hessheimer AJ, de Lope CR, Reig M, Bianchi L, Llovet JM, Bruix J. Evaluation of tumor response after locoregional therapies in hepatocellular carcinoma: are response evaluation criteria in solid tumors reliable? *Cancer* 2009; **115**: 616-623
- 42 **Djavan B**, Zlotta AR, Susani M, Heinz G, Shariat S, Silverman DE, Schulman CC, Marberger M. Transperineal radiofrequency interstitial tumor ablation of the prostate: correlation of magnetic resonance imaging with histopathologic examination. *Urology* 1997; **50**: 986-992; discussion 992-993
- 43 **Nahum Goldberg S**, Dupuy DE. Image-guided radiofrequency tumor ablation: challenges and opportunities—part I. *J Vasc Interv Radiol* 2001; **12**: 1021-1032
- 44 **Dromain C**, de Baere T, Elias D, Kuoch V, Ducreux M, Boige V, Petrow P, Roche A, Sigal R. Hepatic tumors treated with percutaneous radio-frequency ablation: CT and MR imaging follow-up. *Radiology* 2002; **223**: 255-262
- 45 **Babu-Narayan SV**, Goktekin O, Moon JC, Broberg CS, Pantely GA, Pennell DJ, Gatzoulis MA, Kilner PJ. Late gadolinium enhancement cardiovascular magnetic resonance of the systemic right ventricle in adults with previous atrial redirection surgery for transposition of the great arteries. *Circulation* 2005; **111**: 2091-2098
- 46 **Nazarian S**, Bluemke DA, Lardo AC, Zviman MM, Watkins SP, Dickfeld TL, Meininger GR, Roguin A, Calkins H, Tomaselli GF, Weiss RG, Berger RD, Lima JA, Halperin HR. Magnetic resonance assessment of the substrate for inducible ventricular tachycardia in nonischemic cardiomyopathy. *Circulation* 2005; **112**: 2821-2825
- 47 **McGann CJ**, Kholmovski EG, Oakes RS, Blauer JJ, Daccret M, Segerson N, Airey KJ, Akoum N, Fish E, Badger TJ, DiBella EV, Parker D, MacLeod RS, Marrouche NF. New magnetic resonance imaging-based method for defining the extent of left atrial wall injury after the ablation of atrial fibrillation. *J Am Coll Cardiol* 2008; **52**: 1263-1271
- 48 **Bello D**, Fieno DS, Kim RJ, Pereles FS, Passman R, Song G, Kadish AH, Goldberger JJ. Infarct morphology identifies patients with substrate for sustained ventricular tachycardia. *J Am Coll Cardiol* 2005; **45**: 1104-1108
- 49 **Schmidt A**, Azevedo CF, Cheng A, Gupta SN, Bluemke DA, Foo TK, Gerstenblith G, Weiss RG, Márban E, Tomaselli GF, Lima JA, Wu KC. Infarct tissue heterogeneity by magnetic resonance imaging identifies enhanced cardiac arrhythmia susceptibility in patients with left ventricular dysfunction. *Circulation* 2007; **115**: 2006-2014
- 50 **Dickfeld T**, Tian J, Ahmad G, Jimenez A, Turgeman A, Kuk R, Peters M, Saliaris A, Saba M, Shorofsky S, Jeudy J. MRI-Guided ventricular tachycardia ablation: integration of late gadolinium-enhanced 3D scar in patients with implantable cardioverter-defibrillators. *Circ Arrhythm Electrophysiol* 2011;

- 4: 172-184
- 51 **van Dockum WG**, ten Cate FJ, ten Berg JM, Beek AM, Twisk JW, Vos J, Hofman MB, Visser CA, van Rossum AC. Myocardial infarction after percutaneous transluminal septal myocardial ablation in hypertrophic obstructive cardiomyopathy: evaluation by contrast-enhanced magnetic resonance imaging. *J Am Coll Cardiol* 2004; **43**: 27-34
 - 52 **Schalla S**, Saeed M, Higgins CB, Weber O, Martin A, Moore P. Balloon sizing and transcatheter closure of acute atrial septal defects guided by magnetic resonance fluoroscopy: assessment and validation in a large animal model. *J Magn Reson Imaging* 2005; **21**: 204-211
 - 53 **Allen KB**, Dowling RD, Fudge TL, Schoettle GP, Selinger SL, Gangahar DM, Angell WW, Petracek MR, Shaar CJ, O'Neill WW. Comparison of transmyocardial revascularization with medical therapy in patients with refractory angina. *N Engl J Med* 1999; **341**: 1029-1036
 - 54 **Ruel M**, Laham RJ, Parker JA, Post MJ, Ware JA, Simons M, Sellke FW. Long-term effects of surgical angiogenic therapy with fibroblast growth factor 2 protein. *J Thorac Cardiovasc Surg* 2002; **124**: 28-34
 - 55 **Stamm C**, Kleine HD, Choi YH, Dunkelmann S, Lauffs JA, Lorenzen B, David A, Liebold A, Nienaber C, Zurakowski D, Freund M, Steinhoff G. Intramyocardial delivery of CD133+ bone marrow cells and coronary artery bypass grafting for chronic ischemic heart disease: safety and efficacy studies. *J Thorac Cardiovasc Surg* 2007; **133**: 717-725
 - 56 **Vulliet PR**, Greeley M, Halloran SM, MacDonald KA, Kittleson MD. Intra-coronary arterial injection of mesenchymal stromal cells and microinfarction in dogs. *Lancet* 2004; **363**: 783-784
 - 57 **Saeed M**, Hetts SW, Do L, Wilson MW. MRI study on volume effects of coronary emboli on myocardial function, perfusion and viability. *Int J Cardiol* 2011; Epub ahead of print
 - 58 **Saeed M**, Hetts SW, Ursell PC, Do L, Kolli KP, Wilson MW. Evaluation of the acute effects of distal coronary microembolization using multidetector computed tomography and magnetic resonance imaging. *Magn Reson Med* 2011; Epub ahead of print
 - 59 **Maintz D**, Ozgun M, Hoffmeier A, Fischbach R, Kim WY, Stuber M, Manning WJ, Heindel W, Botnar RM. Selective coronary artery plaque visualization and differentiation by contrast-enhanced inversion prepared MRI. *Eur Heart J* 2006; **27**: 1732-1736
 - 60 **Yeon SB**, Sabir A, Clouse M, Martinezclark PO, Peters DC, Hauser TH, Gibson CM, Nezafat R, Maintz D, Manning WJ, Botnar RM. Delayed-enhancement cardiovascular magnetic resonance coronary artery wall imaging: comparison with multislice computed tomography and quantitative coronary angiography. *J Am Coll Cardiol* 2007; **50**: 441-447
 - 61 **von Bary C**, Makowski M, Preissel A, Keithahn A, Warley A, Spuentrup E, Buecker A, Lazewatsky J, Cesati R, Onthank D, Schickl N, Schachoff S, Hausleiter J, Schömig A, Schwaiger M, Robinson S, Botnar R. MRI of coronary wall remodeling in a swine model of coronary injury using an elastin-binding contrast agent. *Circ Cardiovasc Imaging* 2011; **4**: 147-155
 - 62 **Brasselet C**, Durand E, Addad F, Al Haj Zen A, Smeets MB, Laurent-Maquin D, Bouthors S, Bellon G, de Kleijn D, Godeau G, Garnotel R, Gogly B, Lafont A. Collagen and elastin cross-linking: a mechanism of constrictive remodeling after arterial injury. *Am J Physiol Heart Circ Physiol* 2005; **289**: H2228-H2233
 - 63 **Saeed M**, Saloner D, Do L, Wilson M, Martin A. Cardiovascular magnetic resonance imaging in delivering and evaluating the efficacy of hepatocyte growth factor gene in chronic infarct scar. *Cardiovasc Revasc Med* 2011; **12**: 111-122
 - 64 **Dick AJ**, Lederman RJ. MRI-guided myocardial cell therapy. *Int J Cardiovasc Intervent* 2005; **7**: 165-170
 - 65 **Baklanov DV**, Demuinck ED, Thompson CA, Pearlman JD. Novel double contrast MRI technique for intramyocardial detection of percutaneously transplanted autologous cells. *Magn Reson Med* 2004; **52**: 1438-1442
 - 66 **Graham JJ**, Foltz WD, Vaags AK, Ward MR, Yang Y, Connelly KA, Vijayaraghavan R, Detsky JS, Hough MR, Stewart DJ, Wright GA, Dick AJ. Long-term tracking of bone marrow progenitor cells following intracoronary injection post-myocardial infarction in swine using MRI. *Am J Physiol Heart Circ Physiol* 2010; **299**: H125-H133
 - 67 **Perin EC**, Dohmann HF, Borojevic R, Silva SA, Sousa AL, Mesquita CT, Rossi MI, Carvalho AC, Dutra HS, Dohmann HJ, Silva GV, Belém L, Vivacqua R, Rangel FO, Esporcate R, Geng YJ, Vaughn WK, Assad JA, Mesquita ET, Willerson JT. Transendocardial, autologous bone marrow cell transplantation for severe, chronic ischemic heart failure. *Circulation* 2003; **107**: 2294-2302
 - 68 **Assmus B**, Honold J, Schächinger V, Britten MB, Fischer-Rasokat U, Lehmann R, Teupe C, Pistorius K, Martin H, Abolmaali ND, Tonn T, Dimmeler S, Zeiher AM. Transcortical transplantation of progenitor cells after myocardial infarction. *N Engl J Med* 2006; **355**: 1222-1232
 - 69 **Menasché P**, Alfieri O, Janssens S, McKenna W, Reichenspurner H, Trinquart L, Vilquin JT, Marolleau JP, Seymour B, Larghero J, Lake S, Chatellier G, Solomon S, Desnos M, Hagege AA. The Myoblast Autologous Grafting in Ischemic Cardiomyopathy (MAGIC) trial: first randomized placebo-controlled study of myoblast transplantation. *Circulation* 2008; **117**: 1189-1200
 - 70 **Narazaki G**, Uosaki H, Teranishi M, Okita K, Kim B, Matsuo S, Yamanaka S, Yamashita JK. Directed and systematic differentiation of cardiovascular cells from mouse induced pluripotent stem cells. *Circulation* 2008; **118**: 498-506
 - 71 **Pearlman JD**, Hibberd MG, Chuang ML, Harada K, Lopez JJ, Gladstone SR, Friedman M, Sellke FW, Simons M. Magnetic resonance mapping demonstrates benefits of VEGF-induced myocardial angiogenesis. *Nat Med* 1995; **1**: 1085-1089
 - 72 **Saeed M**, Saloner D, Martin A, Do L, Weber O, Ursell PC, Jacquier A, Lee R, Higgins CB. Adeno-associated viral vector-encoding vascular endothelial growth factor gene: effect on cardiovascular MR perfusion and infarct resorption measurements in swine. *Radiology* 2007; **243**: 451-460
 - 73 **Omary RA**, Green JD, Fang WS, Viöl I, Finn JP, Li D. Use of internal coils for independent and direct MR imaging-guided endovascular device tracking. *J Vasc Interv Radiol* 2003; **14**: 247-254
 - 74 **Omary RA**, Green JD, Schirf BE, Li Y, Finn JP, Li D. Real-time magnetic resonance imaging-guided coronary catheterization in swine. *Circulation* 2003; **107**: 2656-2659
 - 75 **Serfaty JM**, Yang X, Aksit P, Quick HH, Solaiyappan M, Atalar E. Toward MRI-guided coronary catheterization: visualization of guiding catheters, guidewires, and anatomy in real time. *J Magn Reson Imaging* 2000; **12**: 590-594
 - 76 **Paetzel C**, Zorger N, Bachthaler M, Hamer OW, Stehr A, Feuerbach S, Lenhart M, Völkl M, Herold T, Kasprzak P, Nitz WR. Magnetic resonance-guided percutaneous angioplasty of femoral and popliteal artery stenoses using real-time imaging and intra-arterial contrast-enhanced magnetic resonance angiography. *Invest Radiol* 2005; **40**: 257-262
 - 77 **Jeziorska M**, Woolley DE. Local neovascularization and cellular composition within vulnerable regions of atherosclerotic plaques of human carotid arteries. *J Pathol* 1999; **188**: 189-196
 - 78 **Kerwin WF**, Paz O. Cardiac resynchronization therapy: overcoming ventricular dyssynchrony in dilated heart failure. *Cardiol Rev* 2003; **11**: 221-239
 - 79 **Hill JM**, Dick AJ, Raman VK, Thompson RB, Yu ZX, Hinds KA, Pessanha BS, Guttman MA, Varney TR, Martin BJ, Dunbar CE, McVeigh ER, Lederman RJ. Serial cardiac magnetic resonance imaging of injected mesenchymal stem cells. *Circulation* 2003; **108**: 1009-1014
 - 80 **Kraitchman DL**, Tatsumi M, Gilson WD, Ishimori T, Kedzior

- rek D, Walczak P, Segars WP, Chen HH, Fritzges D, Izbudak I, Young RG, Marcelino M, Pittenger MF, Solaiyappan M, Boston RC, Tsui BM, Wahl RL, Bulte JW. Dynamic imaging of allogeneic mesenchymal stem cells trafficking to myocardial infarction. *Circulation* 2005; **112**: 1451-1461
- 81 **Amsalem Y**, Mardor Y, Feinberg MS, Landa N, Miller L, Daniels D, Ocherashvilli A, Holbova R, Yosef O, Barbash IM, Leor J. Iron-oxide labeling and outcome of transplanted mesenchymal stem cells in the infarcted myocardium. *Circulation* 2007; **116**: I38-I45
- 82 **Carr CA**, Stuckey DJ, Tatton L, Tyler DJ, Hale SJ, Sweeney D, Schneider JE, Martin-Rendon E, Radda GK, Harding SE, Watt SM, Clarke K. Bone marrow-derived stromal cells home to and remain in the infarcted rat heart but fail to improve function: an in vivo cine-MRI study. *Am J Physiol Heart Circ Physiol* 2008; **295**: H533-H542
- 83 **Himes N**, Min JY, Lee R, Brown C, Shea J, Huang X, Xiao YF, Morgan JP, Burstein D, Oettgen P. In vivo MRI of embryonic stem cells in a mouse model of myocardial infarction. *Magn Reson Med* 2004; **52**: 1214-1219
- 84 **Cahill KS**, Germain S, Byrne BJ, Walter GA. Non-invasive analysis of myoblast transplants in rodent cardiac muscle. *Int J Cardiovasc Imaging* 2004; **20**: 593-598
- 85 **Modo M**, Beech JS, Meade TJ, Williams SC, Price J. A chronic 1 year assessment of MRI contrast agent-labelled neural stem cell transplants in stroke. *Neuroimage* 2009; **47** Suppl 2: T133-T142
- 86 **Bulte JW**, Kraitchman DL. Monitoring cell therapy using iron oxide MR contrast agents. *Curr Pharm Biotechnol* 2004; **5**: 567-584
- 87 **Frank JA**, Miller BR, Arbab AS, Zywicke HA, Jordan EK, Lewis BK, Bryant LH, Bulte JW. Clinically applicable labeling of mammalian and stem cells by combining superparamagnetic iron oxides and transfection agents. *Radiology* 2003; **228**: 480-487
- 88 **Wöhrle J**, Merkle N, Mailänder V, Nusser T, Schauwecker P, von Scheidt F, Schwarz K, Bommer M, Wiesneth M, Schrezenmeier H, Hombach V. Results of intracoronary stem cell therapy after acute myocardial infarction. *Am J Cardiol* 2010; **105**: 804-812
- 89 **Sardella G**, Mancone M, Bucciarelli-Ducci C, Agati L, Scardala R, Carbone I, Francone M, Di Roma A, Benedetti G, Conti G, Fedele F. Thrombus aspiration during primary percutaneous coronary intervention improves myocardial reperfusion and reduces infarct size: the EXPIRA (thrombectomy with export catheter in infarct-related artery during primary percutaneous coronary intervention) prospective, randomized trial. *J Am Coll Cardiol* 2009; **53**: 309-315

S- Editor Cheng JX L- Editor O'Neill M E- Editor Zheng XM



CT and MR imaging patterns for pancreatic carcinoma invading the extrapancreatic neural plexus (Part II): Imaging of pancreatic carcinoma nerve invasion

Hou-Dong Zuo, Wei Tang, Xiao-Ming Zhang, Qiong-Hui Zhao, Bo Xiao

Hou-Dong Zuo, Wei Tang, Xiao-Ming Zhang, Qiong-Hui Zhao, Bo Xiao, Sichuan Key Laboratory of Medical Imaging, Department of Radiology, Affiliated Hospital of North Sichuan Medical College, Nanchong 637000, Sichuan Province, China
Author contributions: Zhang XM was responsible for checking the manuscript and provided financial support for this work; Zhao QH and Xiao B provided the collection of all the material; Zuo HD and Tang W designed the study and wrote the manuscript.
Supported by National Nature Science Foundation of China, No. 30370436

Correspondence to: Xiao-Ming Zhang, MD, PhD, Professor, Head of Sichuan Key Laboratory of Medical Imaging, Department of Radiology, Affiliated Hospital of North Sichuan Medical College, Nanchong 637000, Sichuan Province, China. cjr.zhxm@vip.163.com

Telephone: +86-817-2262218 Fax: +86-817-2222856

Received: July 30, 2011 Revised: November 17, 2011

Accepted: November 24, 2011

Published online: January 28, 2012

© 2012 Baishideng. All rights reserved.

Key words: Computed tomography; Magnetic resonance imaging; Pancreatic carcinoma; Extrapancreatic neural plexus

Peer reviewer: Kazushi Kishi, Dr, Wakayama Medical University, Kimiidera 811-1, Wakayama City 641-8510, Japan

Zuo HD, Tang W, Zhang XM, Zhao QH, Xiao B. CT and MR imaging patterns for pancreatic carcinoma invading the extrapancreatic neural plexus. Part II: Imaging of pancreatic carcinoma nerve invasion. *World J Radiol* 2012; 4(1): 13-20 Available from: URL: <http://www.wjgnet.com/1949-8470/full/v4/i1/13.htm> DOI: <http://dx.doi.org/10.4329/wjr.v4.i1.13>

Abstract

Computed tomography (CT) and magnetic resonance imaging (MRI) are excellent modalities which have the ability to detect, depict and stage the nerve invasion associated with pancreatic carcinoma. The aim of this article is to review the CT and MR patterns of pancreatic carcinoma invading the extrapancreatic neural plexus and thus provide useful information which could help the choice of treatment methods. Pancreatic carcinoma is a common malignant neoplasm with a high mortality rate. There are many factors influencing the prognosis and treatment options for those patients suffering from pancreatic carcinoma, such as lymphatic metastasis, adjacent organs or tissue invasion, *etc.* Among these factors, extrapancreatic neural plexus invasion is recognized as an important factor when considering the management of the patients.

INTRODUCTION

Pancreatic carcinoma is a common malignant neoplasm with a high mortality rate. There are many factors influencing the prognosis and the selection of treatment methods for those patients suffering pancreatic carcinoma, such as lymphatic metastasis, adjacent organs or tissue invasion, *etc.* Among these factors, extrapancreatic neural plexus invasion is recognized as an important factor when considering the management of the patients.

We all know that neurotropic growth is one of the important biologic features of pancreatic carcinoma; cancer cells possibly spread and metastasize through the perineural space leading to recurrence after surgery^[1-7]. Extrapancreatic neural plexus invasion can be found in the early stage and in small sizes of tumor, even in those less than 2 cm in size^[8,9]. Neural invasion has been found at operation in 91% of patients with pancreatic carcinoma^[10]. Nakao *et al*^[11] found that 90% of intrapancreatic nerve and 69% of extrapancreatic neural plexus were involved in 204 patients with pancreatic carcinoma through

10 years of follow-up; the survival rate in the latter group was markedly lower than that in the former after surgical resection.

The mechanisms of extrapancreatic nerve invasion have been described as follows: (1) destroying perineurium directly; (2) getting into the perineural space through perineurial vessels and reticular fibers; and (3) destroying nerve terminal synapse adventitia. In general, carcinomas in the head, uncinate process and tail of pancreas mainly invade the right coeliac plexus, superior mesentery artery (SMA) **nerve plexus and splenic plexus, respectively**^[5-7,12].

It has been reported that the application of coronal and sagittal multiplanar reformatted images or curved planar reformations enhances the performance of multi-detector row computed tomography (MDCT), especially for the evaluation of local extension of pancreatic adenocarcinoma^[13-15]. It is likely that diagnosis of extrapancreatic neural plexus invasion by pancreatic carcinoma would be more precise and exact using MDCT^[16]. Furthermore, high resolution computed tomography (CT) and dynamic enhanced scanning are of great help to reveal the nerve invasion.

Magnetic resonance imaging (MRI) is a valuable tool in the assessment of the full spectrum of pancreatic diseases, including effective detection, diagnosis, and evaluation of the stage of pancreatic carcinoma^[17]. The sequences including coronal and axial single shot fast spin-echo (SSFSE) T2-weighted MR images, spoiled gradient-echo (SPGR) T1-weighted in- and out-of-phase MR images; as well as fat saturation three-dimensional enhanced SPGR dynamic MR images, axial fat-saturated fast recovery fast spin-echo (FRFSE) T2-weighted images, *etc.*, are used routinely in the diagnosis of pancreatic carcinoma invasion. Dynamic enhanced MRI has an ideal sensitivity and specificity for the detection of local tumor extension and vascular involvement^[18].

Currently, the techniques of enhanced CT, T1-weighted imaging (SPGR), T2-weighted imaging (FRFSE) and MR dynamic enhanced scanning are proving to be the most useful methods^[8,18]. The characteristics of imaging are listed as follows.

IMAGING TECHNIQUES

CT techniques

Plain and contrast-enhanced CT is often used to aid the diagnosis of pancreatic carcinoma and help evaluate the extension including the nerve and vascular invasion. Contrast-enhanced CT can show the tumor and the mass (nerve invasion) clearly during rapid bolus injection of large amounts of iodinated urographic contrast. Also, the results have shown correlation between CT and pathological findings^[8,13,19].

The introduction of multidetector-row scanners has facilitated the acquisition of images during multiple phases of intravenous contrast administration. Utilization of the arterial dominant phase (first phase), using a scan delay of 40 s has resulted in superior pancreatic parenchy-

mal enhancement. This has led to superior tumor-to-pancreatic enhancement differences, facilitating superior tumor detection and diagnosis, when compared to portal venous (second phase, 70 s delay) or delayed phases (third phase, 150 s delay) of imaging. All the images obtained are used to reconstruct and to observe pancreatic carcinoma and the extrapancreatic invasion^[15,16].

MRI techniques

Current MR techniques using phased-array torso coils, thin slices, and dynamic gadolinium-enhanced breath-hold gradient-echo (GRE) sequences are optimal for imaging of pancreatic carcinoma, and each has its own advantages in the detection of smaller tumors and the extension of carcinoma. For a comprehensive assessment of pancreatic carcinoma and extrapancreatic invasion, it is necessary and important to use different series, including T1-weighted imaging (e.g., fast spin-echo imaging with multiple breath-hold acquisitions or single-breath-hold gradient echo imaging); T2-weighted imaging (e.g. FRFSE or SSFSE imaging) and fat saturation three-dimensional enhanced SPGR dynamic MR images. The most helpful sequences are the T1-weighted fat-suppressed and fat saturation three-dimensional gadolinium-enhanced GRE sequences. On the T1-weighted fat-suppressed images, the pancreatic parenchyma usually shows high signal intensity due to its abundant proteinaceous element while the tumor is of low signal intensity. On the gadolinium-enhanced GRE images, pancreatic carcinomas enhance less than the surrounding parenchyma due the lack of blood supply; when the signal of adipose tissue is very low, the enhanced pancreatic parenchyma and vessels render the ideal setting for observation. Furthermore, MRI has high sensitivity in the detection of small tumors, vascular metastasis and nerve invasion^[20-23].

Dynamic imaging is performed with four breath-hold sequences- before the injection (corresponding to unenhanced imaging), immediately after the injection (arterial dominant phase of enhancement), 30 s afterward (early venous phase of enhancement), and 1 min afterward (late venous phase of enhancement). An additional delayed phase was acquired using a two-dimensional single-section SPGR technique in a study performed by our group^[22]. All the MRI pictures were taken from our hospital patients, and all the examinations were conducted on 1.5-T MR imagers (Signa, GE Healthcare).

CT PATTERNS OF PANCREATIC CARCINOMA INVADING EXTRAPANCREATIC NEURAL PLEXUS

CT has been used to study the extrapancreatic neural plexus invasion in common bile duct carcinoma^[8,24,25] and pancreatic carcinoma^[26]. Miura^[24] reported that a mass-like lesion located between the medial portion of the uncinate process and the SMA or celiac artery could diagnose extrapancreatic neural plexus invasion around

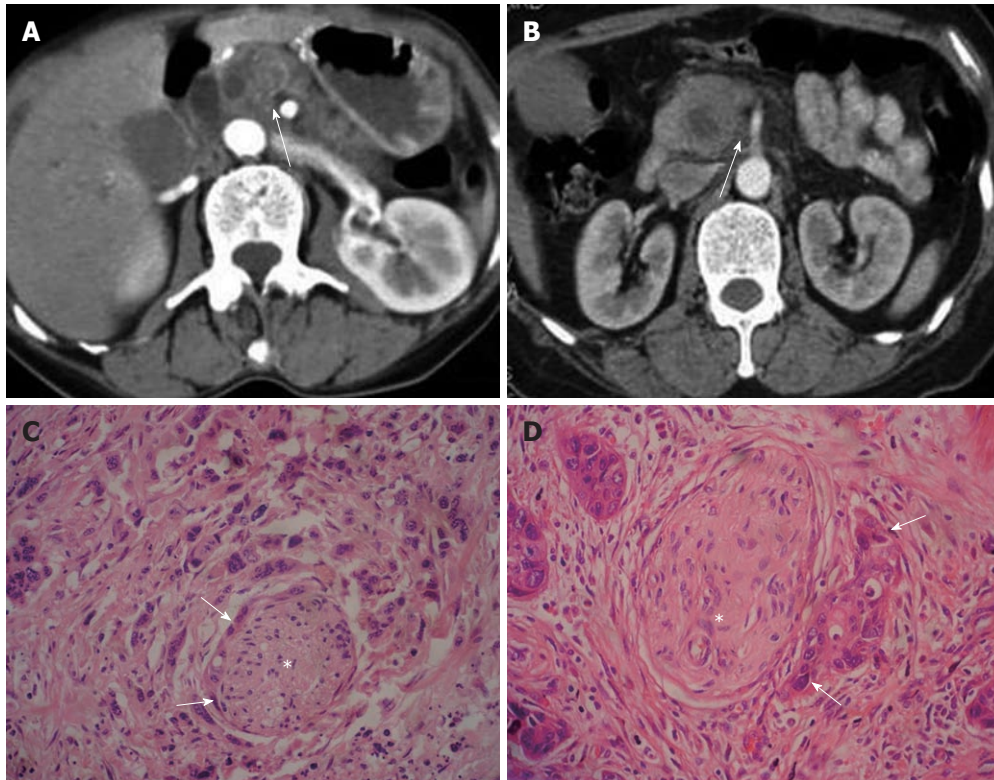


Figure 1 Examples of patterns of extrapancreatic neural invasion by pancreatic carcinoma visualized by computed tomography. A: Sixty-three-year-old male with pancreatic carcinoma in the pancreas body. Contrast-enhanced computed tomography (CT) images during the arterial dominant phase show strand-like structure (arrow) around the superior mesenteric artery; B: Sixty-seven-year-old female with pancreatic carcinoma in the pancreas head. Contrast-enhanced CT images during the arterial dominant phase show strand-like structure (arrow) around celiac trunk; C: Histopathology confirmed extrapancreatic neural (asterisk) invasion by pancreatic carcinoma (arrows) (HE, 200 \times); D: Histopathology confirmed extrapancreatic neural (asterisk) invasion by pancreatic carcinoma (arrows) (HE, 200 \times).

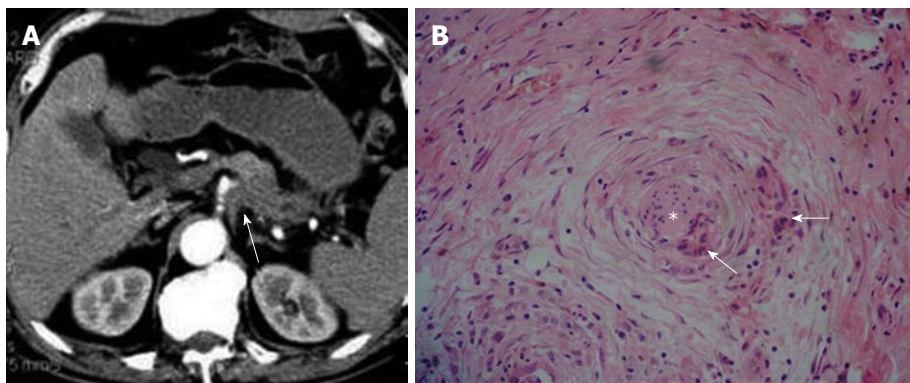


Figure 2 Patterns of extrapancreatic neural invasion by pancreatic carcinoma: Computed tomography images in a 70-year-old male with pancreatic carcinoma in the pancreas body and tail. A: Contrast-enhanced computed tomography image shows the coeliac plexus invasion (arrow) by the tumor; B: Histological image shows the extrapancreatic perineural (asterisk) invasion by the pancreatic carcinoma (arrows) (HE, 200 \times).

the SMA and celiac artery with an accuracy of 63% on CT using 5 mm slice table incremental CE-CT, when performed on eight patients with pancreatic head carcinoma.

The main patterns of extrapancreatic neural invasion by pancreatic carcinoma on CT have been seen to include: (1) peripancreatic retroperitoneal adipose tissue space disappeared and irregular soft tissue found in adipose tissue space; (2) adipose tissue space around SMA or superior mesenteric vein (SMV) disappeared; (3) adipose tissue space around celiac trunk disappeared; and (4) adipose tissue space behind spleen vein became narrow

or disappeared^[8,16]. The second portion of the extrapancreatic neural plexus (PLX-II) is more susceptible to be invaded by carcinoma of pancreatic head^[10,27] (Figure 1). The coeliac plexus is preferentially invaded by carcinoma of the head and body of the pancreas (Figure 2). The splenic neural plexus is often invaded by carcinoma of the pancreatic tail^[6,12] (Figures 3 and 4).

Tian *et al*^[8] studied 41 patients with carcinoma of pancreatic head, establishing two levels of criteria (A and B) for the assessment of neural plexus invasion on thin-section helical CT imaging. Criterion A was with respect

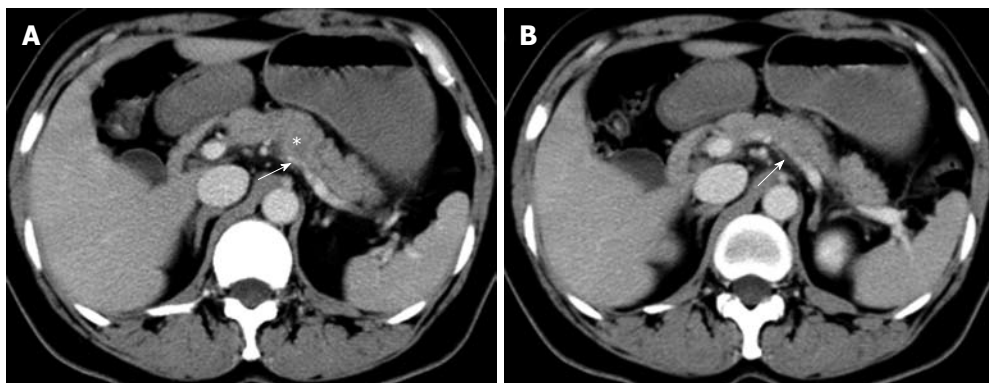


Figure 3 Patterns of extrapancreatic neural invasion by pancreatic carcinoma visualized by computed tomography in a 56-year-old female with pancreatic carcinoma in the pancreas body. Contrast-enhanced computed tomography images (A, B) show the splenic plexus invasion (arrows) by the tumor (asterisk) in the body of pancreas. The appearance of plexus invasion is streaky structure.

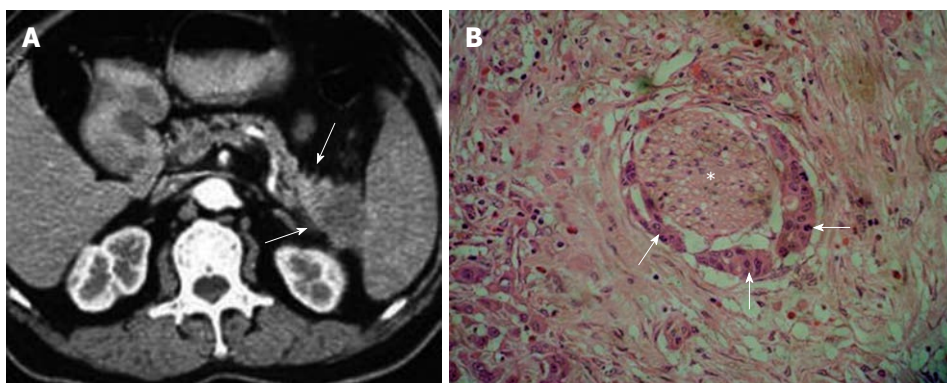


Figure 4 Characteristics of extrapancreatic neural invasion by pancreatic carcinoma on computed tomography image. A: Imaging shows the streaky and strand-like structure (arrows) around the tail of pancreas; B: The histological picture confirmed the invasion (asterisk) by the carcinoma (arrows) (HE, 200 \times).

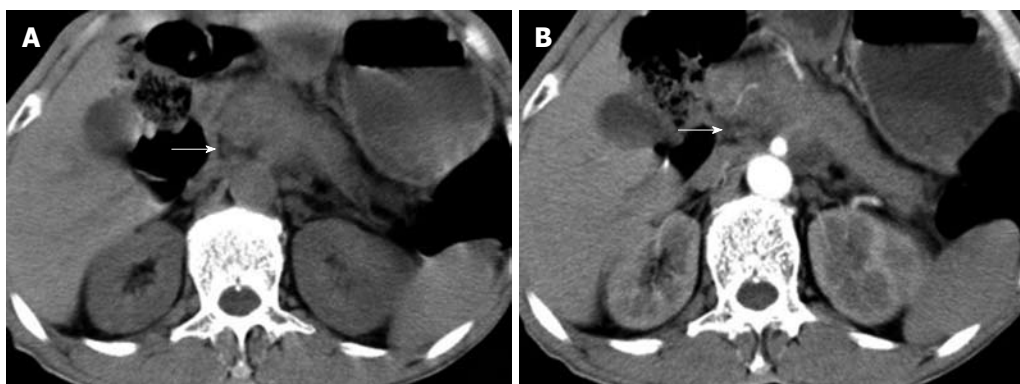


Figure 5 Characteristics of extrapancreatic neural invasion by pancreatic carcinoma on computed tomography image in a 62-year-old male with pancreatic ductal carcinoma. Non-enhanced computed tomography (CT) imaging (A) and contrast-enhanced CT imaging (B) during the arterial dominant phase shows the tumor was located in the head of pancreas and invaded medial to pancreas forming a mass (arrows).

to changes in the area around the SMA and inferior pancreaticoduodenal artery (IPDA), because the IPDA was mostly visualized on thin-section helical CT and was included in the PLX- II: A0, no change in fat attenuation; A1, increase in fat attenuation, such as a streaky and strand-like structure (Figures 1, 3 and 4); A2, mass formation (Figures 2, 5 and 6)^[16,28,29]. Criterion B was defined based on the status of the jejunal trunk (JT) because JT's

are exclusively visualized on thin-section helical CT and run across the PLX- II: V-, normal JT; V+, stenosis or obstruction of the JT^[30].

Tian *et al*^[8] reported that neural plexus was invaded in 85% of pancreatic carcinoma, and that there was no correlation between carcinoma size and the incidence of carcinoma invasion to the PLX- II. The sensitivity, specificity and accuracy were, respectively, 100%, 91% and

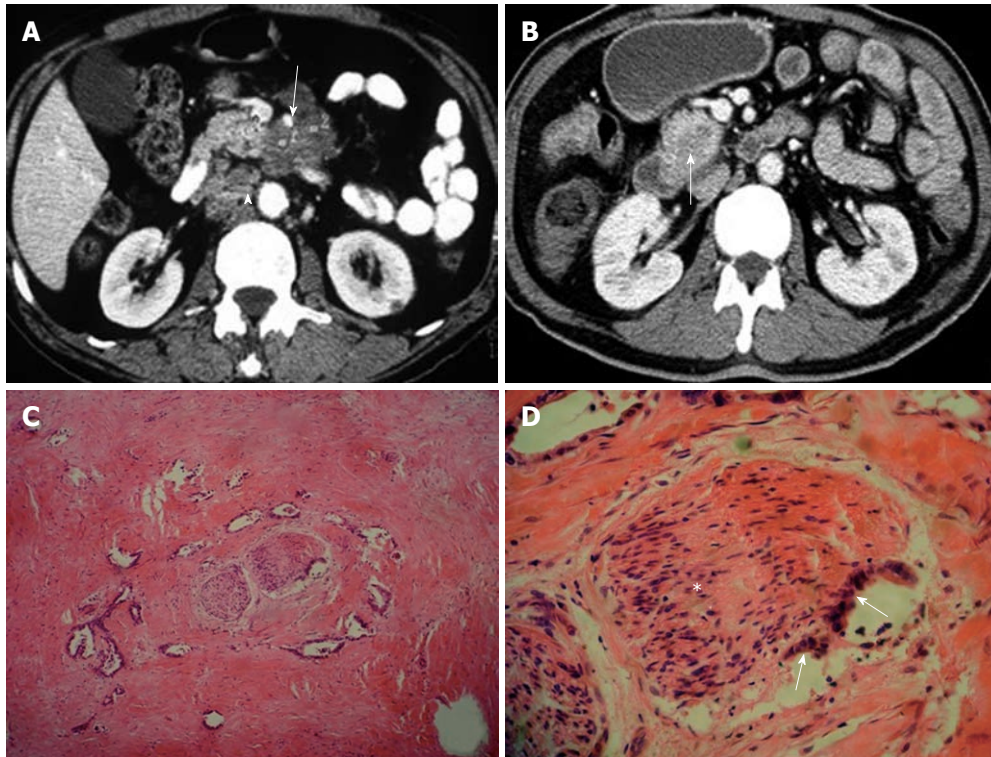


Figure 6 Contrast-enhanced computed tomography images of features of extrapancreatic neural invasion by pancreatic carcinoma. A and B: Imaging shows tumor (arrows) forming the mass (arrowhead) in the space around abdominal aorta, superior mesenteric artery, superior mesenteric vein and inferior vena cava (A) and in the space between superior mesenteric artery and inferior vena cava (B); C and D: Histological pictures demonstrate the peripancreatic invasion (asterisk) by the carcinoma (arrows) (C, HE, 40 \times ; D, HE, 200 \times).

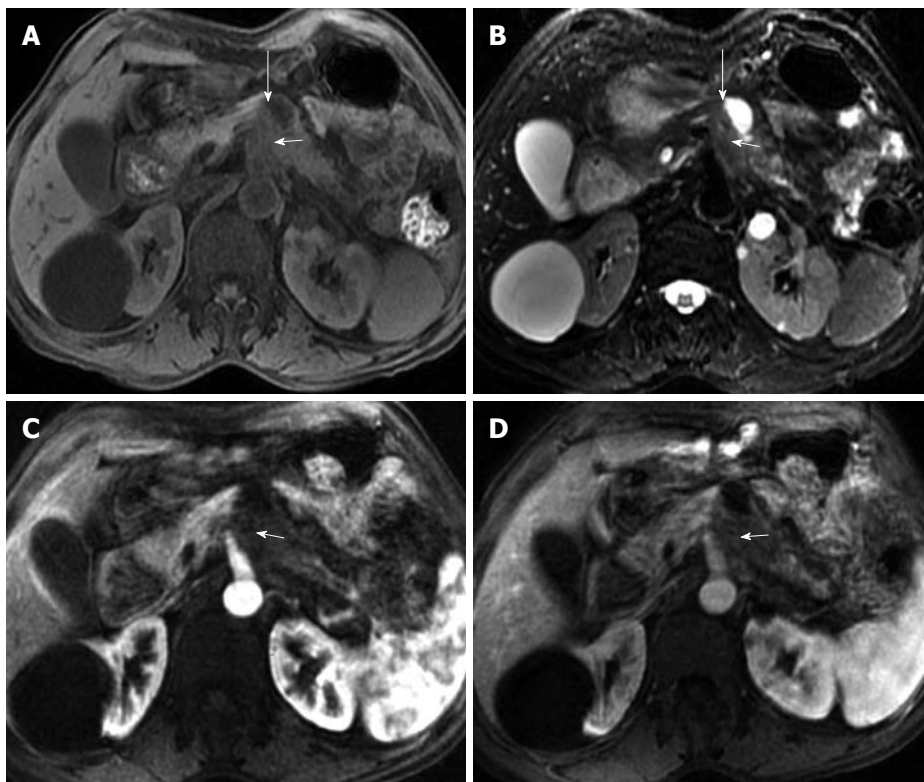


Figure 7 Example of patterns of extrapancreatic neural invasion by pancreatic carcinoma and the characteristics as visualized by magnetic resonance imaging. Fifty-seven-year-old female with pancreatic body carcinoma: magnetic resonance images. The tumor (short arrows) was located at the body of the pancreas which showed hypointensity on T1-weighted imaging (A), arterial phase (C) and venous phase (D), while it showed hyperintensity on T2-weighted imaging (B); there was streak-like signal intensity structure (long arrows) between pancreatic body and abdominal aorta.

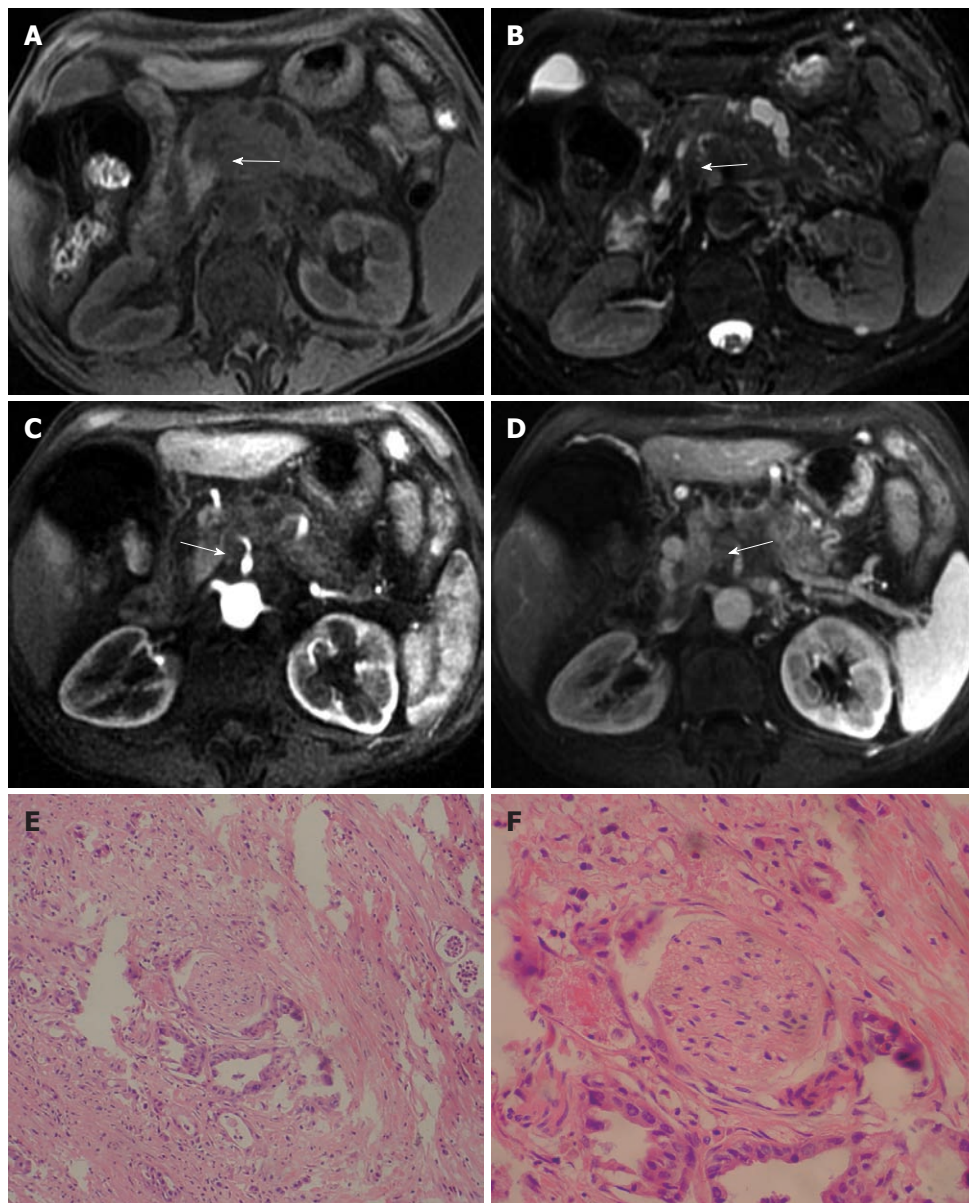


Figure 8 Characteristics of tumor and the extrapancreatic neural invasion by pancreatic carcinoma on magnetic resonance images in an 80-year-old female. The tumor was located at the region between head and body of the pancreas and invaded medial to pancreas forming a mass (arrows). A: 3D gradient-echo (GRE) T1-weighted precontrast image; B: Fat-saturated fast recovery fast spin-echo T2-weighted image; C and D: 3D GRE T1-weighted Gd-enhanced arterial and venous phases. Histopathology confirmed extrapancreatic neural invasion by pancreatic carcinoma (arrows); E: HE, 40 \times ; F: HE, 200 \times .

95% according to criterion A; and 18%, 100% and 62% according to criterion B, for evaluating the PLX-II invasion. They concluded that criterion A had higher sensitivity and accuracy, while criterion B had higher specificity.

MR IMAGING PATTERNS OF PANCREATIC CARCINOMA INVADING EXTRAPANCREATIC NEURAL PLEXUS

The potential invasion to the extrapancreatic neural region near to pancreatic carcinoma on MR imaging was seen to include regions posterior and media to the pancreatic head, posterior to body of the pancreas, and also included the involvement of major vessels adjacent to

the tumor, including the SMV and/or portal vein, SMA, celiac axis artery, common and/or proper hepatic artery, and splenic artery^[22].

On MR imaging, the degree of the extrapancreatic neural invasion might be classified into three grades^[8,17]: NV0, no change in fat signal intensity; NV1, streaky and strand-like signal intensity structure in fat tissue (Figure 7); NV2, irregular masses (diameter larger than 10 mm) adjacent to the lesions (Figure 8).

Pancreatic carcinoma local invasion or extension has been shown as irregular signal intensity in the peripancreatic fat layer, spicular formations with hypointensity on the pancreatic surface, streaky and strand-like signal intensity structures, and mass forming in the peripancreatic fat space on MR imaging^[23,31-33].

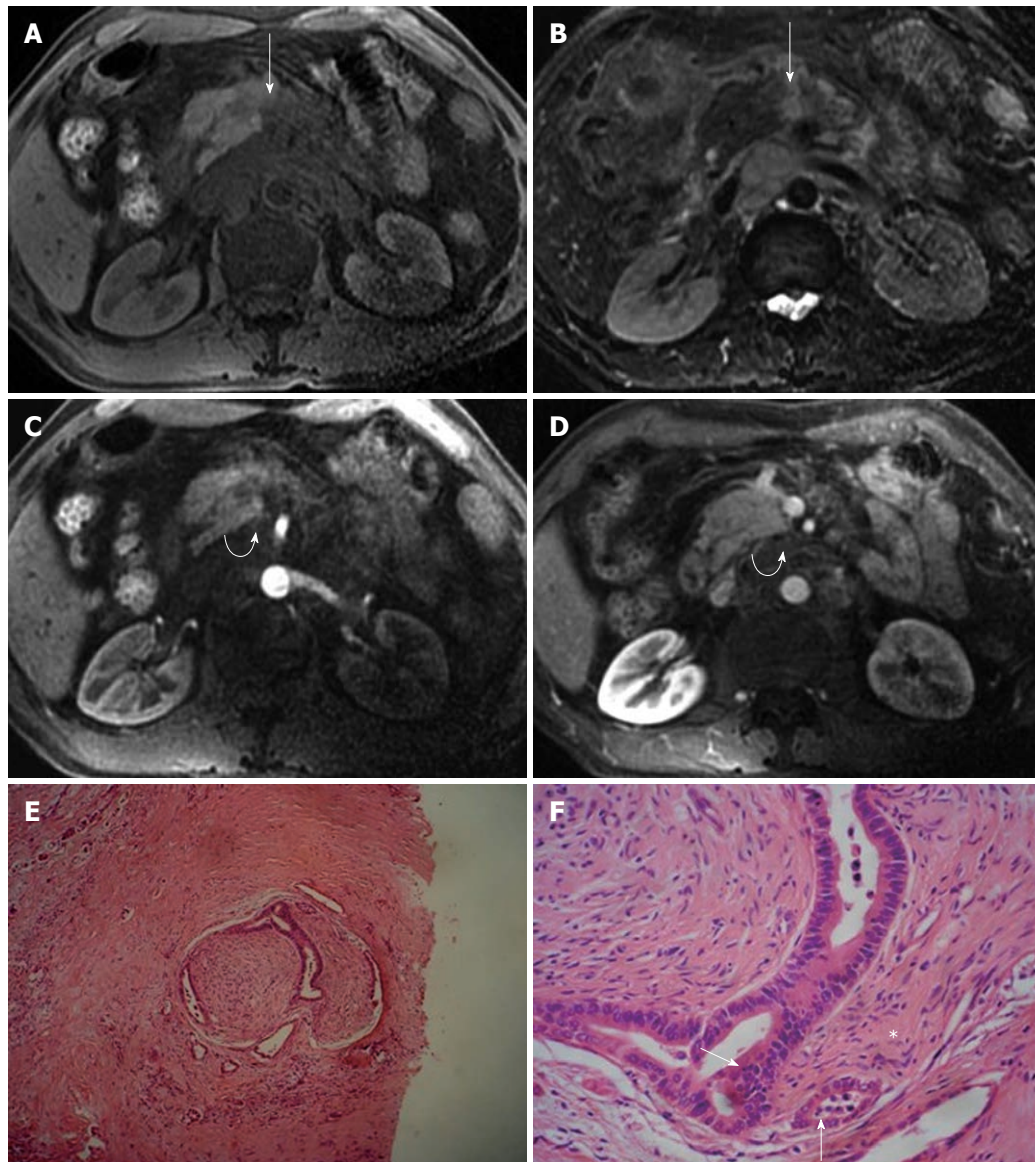


Figure 9 Magnetic resonance imaging characteristics of extrapancreatic neural invasion by pancreatic carcinoma in a 48-year-old male. The tumor (arrows) was located at the body of the pancreas and invaded the extrapancreatic neural plexus, forming a mass (curved arrows), and the adjacent celiac trunk. A: 3D gradient-echo (GRE) T1-weighted non-enhanced image; B: Fat-saturated fast recovery fast spin-echo T2-weighted image; C and D: 3D GRE T1-weighted Gd-enhanced arterial and venous phases. Histopathological images showed extrapancreatic neural (asterisk) invasion by pancreatic carcinoma (arrows); E: HE, 40 \times ; F: HE, 200 \times .

The signal intensity of the nerve invasion is similar to that of pancreatic carcinoma on MR imaging^[17,18], mostly showing hypointensity on T1-weighted, isointensity or a little hyperintensity on T2-weighted, hypointensity on arterial phase, and isointensity on delayed phase images after Gd-DTPA contrast enhancement^[31,34,35].

We have previously studied 20 patients with pancreatic carcinoma by MR imaging, and found the signs of extrapancreatic neural plexus invasion in 16 of the 20 patients (80%); 50% of patients showed streaky and strand-like signal intensity structures in fatty tissue, and 30% showed masses near the tumor. The signal intensity of the nerve invasion was hypointense on T1-weighted imaging and isointense on T2-weighted imaging in 88% of the patients, hypointense on arterial phase and isointense on delayed phase in 94% of the patients. Furthermore,

vascular invasion was often demonstrated in the setting of nerve invasion (Figure 9), and the degree of vascular invasion was correlated with that of nerve invasion ($r = 0.58$, $P < 0.005$)^[22].

CONCLUSION

Extrapancreatic neural plexus invasion by pancreatic carcinoma on CT and MR imaging appears as streaky and strand-like signal intensity structures in fat tissue and irregular masses adjacent to the tumor, with accompanying vascular invasion. CT and MRI are excellent modalities which are of great importance to detect, depict and stage the nerve invasion associated with pancreatic carcinoma. Imaging is beneficial to the management of patients with pancreatic carcinoma.

REFERENCES

- 1 **Pour PM**, Bell RH, Batra SK. Neural invasion in the staging of pancreatic cancer. *Pancreas* 2003; **26**: 322-325
- 2 **Makino I**, Kitagawa H, Ohta T, Nakagawara H, Tajima H, Ohnishi I, Takamura H, Tani T, Kayahara M. Nerve plexus invasion in pancreatic cancer: spread patterns on histopathologic and embryological analyses. *Pancreas* 2008; **37**: 358-365
- 3 **Liu B**, Lu KY. Neural invasion in pancreatic carcinoma. *Hepatobiliary Pancreat Dis Int* 2002; **1**: 469-476
- 4 **Hirai I**, Kimura W, Ozawa K, Kudo S, Suto K, Kuzu H, Fuse A. Perineural invasion in pancreatic cancer. *Pancreas* 2002; **24**: 15-25
- 5 **Noto M**, Miwa K, Kitagawa H, Kayahara M, Takamura H, Shimizu K, Ohta T. Pancreas head carcinoma: frequency of invasion to soft tissue adherent to the superior mesenteric artery. *Am J Surg Pathol* 2005; **29**: 1056-1061
- 6 **Nano M**, Lanfranco G, Ferronato M, Dal Corso H, Solej M. [Contribution to the study of innervation of the pancreas with a view to its relevance to neoplasm surgery]. *Chir Ital* 2001; **53**: 587-594
- 7 **Mitsunaga S**, Hasebe T, Kinoshita T, Konishi M, Takahashi S, Gotohda N, Nakagohri T, Ochiai A. Detail histologic analysis of nerve plexus invasion in invasive ductal carcinoma of the pancreas and its prognostic impact. *Am J Surg Pathol* 2007; **31**: 1636-1644
- 8 **Tian H**, Mori H, Matsumoto S, Yamada Y, Kiyosue H, Ohta M, Kitano S. Extrapaneatic neural plexus invasion by carcinomas of the pancreatic head region: evaluation using thin-section helical CT. *Radiat Med* 2007; **25**: 141-147
- 9 **Takahashi T**, Ishikura H, Kato H, Tanabe T, Yoshiki T. Intra-pancreatic, extra-tumoral perineural invasion (nex). An indicator for the presence of retroperitoneal neural plexus invasion by pancreas carcinoma. *Acta Pathol Jpn* 1992; **42**: 99-103
- 10 **Kayahara M**, Nagakawa T, Konishi I, Ueno K, Ohta T, Miyazaki I. Clinicopathological study of pancreatic carcinoma with particular reference to the invasion of the extrapancreatic neural plexus. *Int J Pancreatol* 1991; **10**: 105-111
- 11 **Nakao A**, Harada A, Nonami T, Kaneko T, Takagi H. Clinical significance of carcinoma invasion of the extrapancreatic nerve plexus in pancreatic cancer. *Pancreas* 1996; **12**: 357-361
- 12 **Yi SQ**, Miwa K, Ohta T, Kayahara M, Kitagawa H, Tanaka A, Shimokawa T, Akita K, Tanaka S. Innervation of the pancreas from the perspective of perineural invasion of pancreatic cancer. *Pancreas* 2003; **27**: 225-229
- 13 **Ichikawa T**, Erturk SM, Sou H, Nakajima H, Tsukamoto T, Motosugi U, Araki T. MDCT of pancreatic adenocarcinoma: optimal imaging phases and multiplanar reformatted imaging. *AJR Am J Roentgenol* 2006; **187**: 1513-1520
- 14 **Nino-Murcia M**, Jeffrey RB, Beaulieu CF, Li KC, Rubin GD. Multidetector CT of the pancreas and bile duct system: value of curved planar reformations. *AJR Am J Roentgenol* 2001; **176**: 689-693
- 15 **Vargas R**, Nino-Murcia M, Trueblood W, Jeffrey RB. MDCT in Pancreatic adenocarcinoma: prediction of vascular invasion and resectability using a multiphasic technique with curved planar reformations. *AJR Am J Roentgenol* 2004; **182**: 419-425
- 16 **Mochizuki K**, Gabata T, Kozaka K, Hattori Y, Zen Y, Kitagawa H, Kayahara M, Ohta T, Matsui O. MDCT findings of extrapancreatic nerve plexus invasion by pancreas head carcinoma: correlation with en bloc pathological specimens and diagnostic accuracy. *Eur Radiol* 2010; **20**: 1757-1767
- 17 **Pamuklar E**, Semelka RC. MR imaging of the pancreas. *Magn Reson Imaging Clin N Am* 2005; **13**: 313-330
- 18 **Fayad LM**, Mitchell DG. Magnetic resonance imaging of pancreatic adenocarcinoma. *Int J Gastrointest Cancer* 2001; **30**: 19-25
- 19 **Grenacher L**, Klauss M. [Computed tomography of pancreatic tumors]. *Radiologe* 2009; **49**: 107-123
- 20 **Wang DQ**, Zeng MS, Jin DY, Lou WH, Ji Y, Rao SX, Chen CZ, Li RC. [Evaluation of 2D and 3D MRI imaging in the diagnosis of pancreatic carcinoma]. *Zhonghua Zhongliu Zazhi* 2007; **29**: 216-220
- 21 **Chandarana H**, Babb J, Macari M. Signal characteristic and enhancement patterns of pancreatic adenocarcinoma: evaluation with dynamic gadolinium enhanced MRI. *Clin Radiol* 2007; **62**: 876-883
- 22 **Zhang XM**, Mitchell DG, Witkiewicz A, Verma S, Bergin D. Extrapaneatic neural plexus invasion by pancreatic carcinoma: characteristics on magnetic resonance imaging. *Abdom Imaging* 2009; **34**: 634-641
- 23 **Zhang XM**, Mitchell DG, Byun JH, Verma SK, Bergin D, Witkiewicz A. MR imaging for predicting the recurrence of pancreatic carcinoma after surgical resection. *Eur J Radiol* 2010; **73**: 572-578
- 24 **Miura K**. [The evaluation of thin slice incremental CE-CT for diagnosis of extension of pancreatic carcinoma--comparison of CT and pathological findings]. *Nihon Igaku Hoshusen Gakkai Zasshi* 1991; **51**: 245-259
- 25 **Ochotorena IJ**, Kiyosue H, Hori Y, Yokoyama S, Yoshida T, Mori H. The local spread of lower bile duct cancer: evaluation by thin-section helical CT. *Eur Radiol* 2000; **10**: 1106-1113
- 26 **Fukuda T**, Iwanaga S, Sakamoto I, Aso N, Nagaoki K, Hayashi K, Yamaguchi H, Okudaira S, Tomioka T, Okimoto T. CT of neural plexus invasion in common bile duct carcinoma. *J Comput Assist Tomogr* 1998; **22**: 351-356
- 27 **Kaneko T**, Nakao A, Inoue S, Nomoto S, Nagasaka T, Nakashima N, Harada A, Nonami T, Takagi H. Extrapaneatic nerve plexus invasion by carcinoma of the head of the pancreas. Diagnosis with intraportal endovascular ultrasonography. *Int J Pancreatol* 1996; **19**: 1-7
- 28 **Tezel E**, Kaneko T, Sugimoto H, Takeda S, Inoue S, Nagasaka T, Nakao A. Clinical significance of intraportal endovascular ultrasonography for the diagnosis of extrapancreatic nerve plexus invasion by pancreatic carcinoma. *Pancreatol* 2004; **4**: 76-81
- 29 **Shioyama Y**, Kimura M, Horihata K, Masuda M, Hagiwara T, Okumura T, Yoshimi F, Amemiya R, Kishi K, Terada M, Sato M. Peripaneatic arteries in thin-section multislice helical CT. *Abdom Imaging* 2001; **26**: 234-242
- 30 **Yamada Y**, Mori H, Kiyosue H, Matsumoto S, Hori Y, Maeda T. CT assessment of the inferior peripaneatic veins: clinical significance. *AJR Am J Roentgenol* 2000; **174**: 677-684
- 31 **Irie H**, Honda H, Kaneko K, Kuroiwa T, Yoshimitsu K, Masuda K. Comparison of helical CT and MR imaging in detecting and staging small pancreatic adenocarcinoma. *Abdom Imaging* 1997; **22**: 429-433
- 32 **Ichikawa T**, Haradome H, Hachiya J, Nitatori T, Ohtomo K, Kinoshita T, Araki T. Pancreatic ductal adenocarcinoma: preoperative assessment with helical CT versus dynamic MR imaging. *Radiology* 1997; **202**: 655-662
- 33 **Nishiharu T**, Yamashita Y, Abe Y, Mitsuzaki K, Tsuchigame T, Nakayama Y, Takahashi M. Local extension of pancreatic carcinoma: assessment with thin-section helical CT versus with breath-hold fast MR imaging--ROC analysis. *Radiology* 1999; **212**: 445-452
- 34 **Lu DS**, Reber HA, Krasny RM, Kadell BM, Sayre J. Local staging of pancreatic cancer: criteria for unresectability of major vessels as revealed by pancreatic-phase, thin-section helical CT. *AJR Am J Roentgenol* 1997; **168**: 1439-1443
- 35 **Sironi S**, De Cobelli F, Zerbi A, Balzano G, Di Carlo V, Del-Maschio A. Pancreatic carcinoma: MR assessment of tumor invasion of the peripaneatic vessels. *J Comput Assist Tomogr* 1995; **19**: 739-744

S- Editor Cheng JX L- Editor Logan S E- Editor Zheng XM



Radiation dose reduction with application of non-linear adaptive filters for abdominal CT

Sarabjeet Singh, Mannudeep K Kalra, Mi Kim Sung, Anni Back, Michael A Blake

Sarabjeet Singh, Mannudeep K Kalra, Michael A Blake, Massachusetts General Hospital, Department of Radiology, Harvard Medical School, Boston, MA 02114, United States

Mi Kim Sung, Myongji Hospital, Kwandong University, 522 Naegok-dong, Gangneung-si, Gangwon-do 220-801, South Korea

Anni Back, ContextVision AB, Linköping 58002, Sweden

Author contributions: Singh S helped in patient recruitment, organizing study, literature search, manuscript writing; Kalra MK helped in overall study design and manuscript writing; Sung MK helped in manuscript revision; Back A helped in image processing; Blake MA helped in image quality evaluation and manuscript editing.

Correspondence to: Dr. Sarabjeet Singh, Massachusetts General Hospital, Department of Radiology, Harvard Medical School, 55 Fruit St, Boston, MA 02114,

United States. ssingh6@partners.org

Telephone: +1-617-6430264 Fax: +1-617-6430111

Received: February 10, 2011 Revised: July 8, 2011

Accepted: July 15, 2011

Published online: January 28, 2012

Abstract

AIM: To evaluate the effect of non-linear adaptive filters (NLAF) on abdominal computed tomography (CT) images acquired at different radiation dose levels.

METHODS: Nineteen patients (mean age 61.6 ± 7.9 years, M:F = 8:11) gave informed consent for an Institutional Review Board approved prospective study involving acquisition of 4 additional image series (200, 150, 100, 50 mAs and 120 kVp) on a 64 slice multidetector row CT scanner over an identical 10 cm length in the abdomen. The CT images acquired at 150, 100 and 50 mAs were processed with the NLAF. Two radiologists reviewed unprocessed and processed images for image quality in a blinded randomized manner. CT dose index volume, dose length product, patient weight, transverse diameters, objective noise and CT numbers were

recorded. Data were analyzed using Analysis of Variance and Wilcoxon signed rank test.

RESULTS: Of the 31 lesions detected in abdominal CT images, 28 lesions were less than 1 cm in size. Subjective image noise was graded as unacceptable in unprocessed images at 50 and 100 mAs, and in NLAF processed images at 50 mAs only. In NLAF processed images, objective image noise was decreased by 21% ($14.4 \pm 4/18.2 \pm 4.9$) at 150 mAs, 28.3% ($15.7 \pm 5.6/21.9 \pm 4$) at 100 mAs and by 39.4% ($18.8 \pm 9/30.4 \pm 9.2$) at 50 mAs compared to unprocessed images acquired at respective radiation dose levels. At 100 mAs the visibility of smaller structures improved from suboptimal in unprocessed images to excellent in NLAF processed images, whereas diagnostic confidence was respectively improved from probably confident to fully confident.

CONCLUSION: NLAF lowers image noise, improves the visibility of small structures and maintains lesion conspicuity at down to 100 mAs for abdominal CT.

© 2012 Baishideng. All rights reserved.

Key words: Noise reduction filters; Computed tomography radiation dose reduction; Abdominal computed tomography image quality; Non-linear adaptive filters

Peer reviewers: Ioannis Tsalafoutas, PhD, Medical Physics Department, Anticancer Hospital "Agios Savvas", 171 Alexandras Avenue, 115 22 Athens, Greece; Wazir Muhammad, PhD, Nuclear Energy Application Laboratory, Department of Physics, Kyungpook National University, Sankuk-dong, Buk-gu, Daegu 702-701, South Korea

Singh S, Kalra MK, Sung MK, Back A, Blake MA. Radiation dose reduction with application of non-linear adaptive filters for abdominal CT. *World J Radiol* 2012; 4(1): 21-28 Available from: URL: <http://www.wjgnet.com/1949-8470/full/v4/i1/21.htm> DOI: <http://dx.doi.org/10.4329/wjr.v4.i1.21>

INTRODUCTION

As the use of computed tomography (CT) is increasing, with an estimated 62 million scans per year in the United States in the year 2006^[1,2], the concerns associated with radiation exposure have also increased in both the news media^[3] and the medical literature^[4]. The primary concern of radiation dose associated with CT scanning is radiation-induced carcinogenesis. The probability of radiation-induced cancer is directly related to the radiation dose absorbed by tissues and organs and hence the reduction of dose is of paramount importance.

In CT, reduction of dose results in images with larger image noise or mottle and hence raises the possibility of missing lesions or other diagnostic findings. Efforts have been made to reduce radiation dose while maintaining image quality, which have led to several changes in CT hardware and software technologies^[5-8]. From the software point of view, image post-processing with linear and non-linear filters have been developed and assessed for lowering image noise and improving or maintaining lesion conspicuity on low dose images^[9,10]. Previous clinical studies have reported the use of non-linear image filters for reducing radiation dose for chest and abdominal CT examinations. However, some of these filters lower image noise at the expense of image contrast or visibility of smaller structures^[11-13]. New non-linear adaptive filters (NLAF) have been developed and studied using phantom and simulated CT images^[14-19].

The purpose of our prospective clinical study was to evaluate the effect of a NLAF on abdominal CT images acquired at different dose levels.

MATERIALS AND METHODS

Patients

This prospective clinical study was approved by the Human Research Committee of our Institutional Review Board and was conducted in compliance with Health Insurance Portability and Accountability Act guidelines. All 19 patients (mean age 61.6 ± 7.9 years, male:female = 8:11) gave written informed consent for the acquisition of four additional sets of research images for this study, in addition to their standard-of-care, clinically indicated abdominal CT examinations.

The inclusion criteria for the study included: patients scheduled for clinically indicated abdominal CT examinations, older than 50 years, hemodynamic stability (conscious, oriented, regular respiration rate of 12-40 breaths/min, pulse rate of 60-90 bpm without dysrhythmia, systolic blood pressure of 100-140 mmHg), able to provide written informed consent, able to hold breath for a duration of at least 10 s, and able to understand and follow verbal commands for breath-holding and to remain still for the scanning duration.

Scanning techniques

For all patients included in this study a standard abdominal CT examination was initially performed on a commer-

cially available 64 channel multidetector row CT scanner (Discovery CT750 HD, GE Healthcare, Waukesha, WI.) with administration of an intravenous contrast medium (80-100 mL of Iopamidol 370 mg % Bracco Diagnostics, Princeton, NJ). Subsequently, four additional sets of images were acquired in each patient, through an identical scan length of 10 cm in the abdomen. Selection of the location of the acquisition of these additional image datasets was based on review (by Singh S) of the patient's prior (available and reviewed in 18/19 patients) and current routine (reviewed in 1/19 patients) abdominal CT images to select the most subtle (first preference) or smallest (second preference) lesion in the abdomen. These research image data sets were thus acquired through the most subtle or smallest abdominal lesion immediately after acquisition of standard-of-care abdominal CT images. The maximum time period between the standard-of-care abdominal CT and the research image acquisition was less than 15-30 s. As all research scan series were planned prior to the acquisition of standard-of-care CT images, the maximum interval between the acquisition of the four different research image series was approximately 10 s.

Abdominal CT images were acquired at four different levels of radiation dose by selecting four different fixed tube current-time products (200, 150, 100 and 50 mAs) for abdominal CT. The acquisition sequence of the four research CT datasets was randomized in order to avoid contrast enhancement bias due to the delay in scanning from start of injection. No additional intravenous contrast medium was administered for acquisition of the research image series since it is not feasible to inject contrast media four times to a patient for acquiring images at identical contrast enhancement phase.

With the exception of tube current, reconstruction kernel and section thickness were held constant and included 120 kVp, 0.984:1 pitch, 39.37 mm table speed per gantry rotation, helical acquisition mode, $64 * 0.625$ mm detector configuration and 0.5 s gantry rotation time. All image series were reconstructed at 5 mm section thickness and 5 mm section interval using standard reconstruction kernel as per our routine abdominal CT protocol.

Image post processing

Technical details of the NLAF (ContextVision AB, Linköping, Sweden) used in our study are described in Appendix 1.

Of the 4 additional research abdominal series (acquired at 200, 150, 100, 50 mAs), three lower dose image series (150, 100 and 50 mAs) were processed with NLAF. For post processing with NLAF, the DICOM image series were de-identified and exported to an external USB storage media. These DICOM image series were processed with NLAF to generate six series (three low dose unprocessed series and three NLAF processed image series). The image processing time with NLAF for image series was less than 2 s. Thus, 7 CT image series were available for evaluation (unprocessed 200, 150, 100, 50 mAs and processed 150, 100, 50 mAs) in each patient. Unprocessed images at 200 mAs were used as standard

of reference for lesion detection and image quality assessment.

Each image data set was coded, de-identified and randomized on Microsoft EXCEL 2003 (© Microsoft Corporation, Redmond, WA) by a study co-author (Singh S) to enable double blinded evaluation.

Subjective image quality

All CT image series were reviewed on a Picture Archiving and Communication System diagnostic workstation (AGFA Impax ES, AGFA Technical Imaging Systems, Ridgefield Park, NJ, USA) for assessment of subjective image quality in a randomized manner. All abdominal CT image series were presented to two experienced abdominal radiologists (MAB with 12 years and MKK with 8 years of experience, respectively) for evaluation of image quality. Both radiologists were trained on two image datasets for the grading of different aspects of subjective image quality as well as lesion assessment in order to understand the evaluation system, in addition to improving inter-observer agreement.

Subjective image quality was assessed in terms of subjective image noise on a five point scale (1 = minimal image noise, 2 = less than average noise, 3 = average image noise, 4 = above average noise, 5 = unacceptable image noise). Visibility of smaller structures for abdominal CT (small blood vessels, adrenal glands, small lymph nodes, ducts and walls of hollow structures) was ranked on a five point scale (1 = excellent visualization, 2 = above average visibility, 3 = acceptable visibility, 4 = suboptimal visibility, and 5 = unacceptable visualization of small structures) using abdominal soft tissue window width 400 HU and window level 40 HU. Artifacts were graded on a four point scale (1 = no artifacts; 2 = minor artifacts not interfering with diagnostic decision making; 3 = major artifacts affecting visualization of major structures, diagnosis still possible; 4 = artifacts affecting diagnostic information), while each type of the following artifacts was assessed (helical or windmill artifacts; streak artifacts due to metals and leads; beam hardening artifacts due to arms by body side; rarely, large body size and truncation due to large body size or off centering, and blotchy pixilated appearance). Lesion size was measured on a four point scale (1 = focal and less than 1 cm, 2 = focal and 1-5 cm, 3 = focal and more than 5 cm, 4 = diffuse lesion), lesion conspicuity was assessed on a five point scale (1 = well-seen lesion with well-visualized margins, 2 = well-seen lesion with poorly visualized margins, 3 = subtle lesions, 4 = probably an artifact mimicking a lesion and 5 = definite artifact mimicking a lesion) and diagnostic confidence (1 = completely confident, 2 = probably confident, 3 = confident only for limited clinical situations such as kidney stones, calcified lesions or a large lesion, and 4 = poor confidence). Image quality attributes assessed in our study have been described in the European Guidelines on Quality Criteria for Computerized Tomography document (EUR 16262 www.dr.dk/guidelines/ct/quality/index.htm) and have been used in multiple prior studies in the radiology literature^[7,20-22].

Radiologists were first asked to assess the subjective image noise in the seven image sets of each patient (unprocessed and NLAF processed) and then to assess lesion detection starting from the image series with the highest image noise to avoid bias in lesion detection and characterization.

Objective measurements

Each subject was weighed on a digital weighing machine just prior to the abdominal CT examination. Circular regions of interest (20-30 mm in diameter) were drawn in the homogenous area of the right lobe of liver. Circular regions of interest (20-30 mm in diameter) were also drawn in the abdominal aorta, without touching the lumen walls, to cover at least two thirds of its lumen. The skin-to-skin maximum transverse diameter of abdomen was measured from localizer radiographs, as transverse images are often reconstructed with a smaller field of view and may not include the skin. Objective image noise (standard deviation) and CT numbers (HU) were measured for all 133 CT image series.

CT radiation dose descriptors such as CT dose index volume (CTDI_{vol}, described in mGy) and dose length product (DLP, described in mGy.cm) were recorded from the dose page following completion of the abdominal CT examination for all image series.

Statistical analysis

Data were analyzed using analysis of variance (ANOVA) and Wilcoxon signed rank test. Intraobserver variability was not estimated as each radiologist assessed the images only once. Interobserver variability was estimated using both κ statistics as well as percentage agreement between the two radiologists for each of the assessed subjective image quality and lesion assessment parameters.

RESULTS

There was variable interobserver agreement between the two radiologists ($\kappa = 0.2-1$) for abdominal CT. However, the percentage agreement between the two radiologists ranged from 68.4% (13/19 scores with agreement for visibility of smaller structures) to 100% (19/19 scores in perfect agreement for criteria such as image noise, lesion conspicuity and diagnostic confidence) for the abdominal CT.

Subjective assessment

Detailed subjective lesion detection and image quality scores are summarized in Table 1.

All 31 abdominal lesions detected in 19 patients were seen on both unprocessed and NLAF processed image series at all tube current-time product levels. Twenty-eight lesions (28/31, 90%) were less than 1 cm in maximum dimension and 2 (2/31, 6%) lesions measured 1-5 cm in maximum dimension. Detected lesions included renal cysts and masses ($n = 7$ lesions), abdominal lymph nodes ($n = 5$), adrenal lesions ($n = 4$), gall bladder stones ($n = 3$), focal liver lesions ($n = 2$), peri-renal stranding ($n = 2$), cho-

Table 1 Lesion detection and subjective image quality scores for abdominal computed tomography examinations for non-linear adaptive filters processed and unprocessed image groups at four different radiation dose levels

	Baseline (200 mAs)	Unpro (150 mAs)	Pro (150 mAs)	Unpro (100 mAs)	Pro (100 mAs)	Unpro (50 mAs)	Pro (50 mAs)
No. of lesions	31	31	31	31	31	31	31
Lesion size (< 1 cm)	28	28	28	28	28	28	28
Lesion conspicuity	1	1	1	1	1	1	1
Image noise	2	3	2	4	2	5	4
Visibility of small structures	3	3	3	4	3	4	4
Image contrast	3	3	3	3	3	3	3
Diagnostic confidence	1	1	1	2	1	4	3

Image noise was lowered and visibility of small structures was enhanced with non-linear adaptive filters processing. Since discrete values cannot be averaged, the table presents the lowest or similar modal scores for lesion conspicuity, image noise, contrast and diagnostic confidence given by radiologists. Unpro: Unprocessed; Pro: Processed.

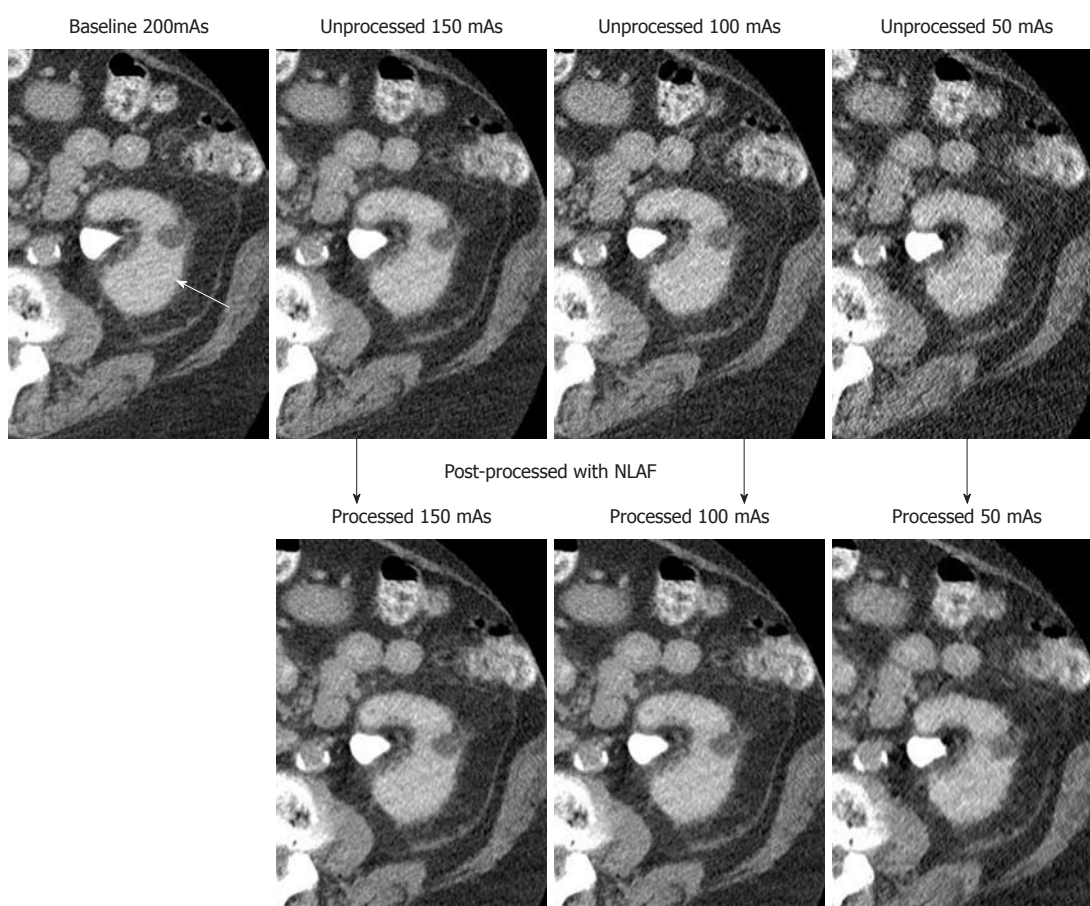


Figure 1 Transverse abdominal computed tomography images in a 72-year-old woman who underwent radiofrequency ablation for renal cell carcinoma showing a renal cyst (white arrow) in the left kidney at four different tube current-time product levels (200, 150, 100 and 50 mAs). Three lower tube current-time products (150, 100 and 50 mAs) when processed with 2D-non-linear adaptive filters showed lower image noise without affecting image contrast.

lecystectomy ($n = 1$), minimal ascites ($n = 1$), surgical clip ($n = 1$), IVC graft ($n = 1$), peri IVC soft tissue stranding ($n = 1$), splenic calcification ($n = 1$), calcified atherosclerotic plaque ($n = 1$) and hydronephrosis ($n = 1$).

Subjective image noise was unacceptable in unprocessed images at 50 and 100 mAs. With NLAF processing, noise was lowered to below average or acceptable at 100 mAs ($P < 0.0001$) but at 50 mAs was still rated as unacceptable (Figure 1). At 50 mAs, abdominal CT

images processed with NLAF were still rated as unacceptable. Visibility of smaller structures, such as small blood vessels, small lymph nodes, ducts or walls of hollow organs, was found to be suboptimal in unprocessed image series at 100 mAs and was improved to acceptable in processed image series. No major artifacts were seen on any of the NLAF processed CT images. Minor beam hardening or photon starvation artifacts were noted in both unprocessed and processed image series in 5 out of

Table 2 Average objective image noise and HU values in abdominal computed tomography examinations for non-linear adaptive filters processed and unprocessed image series at four different radiation dose levels (mean \pm SD)

	Baseline (200 mAs)	Unpro (150 mAs)	Pro (150 mAs)	Unpro (100 mAs)	Pro (100 mAs)	Unpro (50 mAs)	Pro (50 mAs)
Liver							
Objective noise	15.5 \pm 3.9	18.2 \pm 4.9	14.4 \pm 4.0	21.9 \pm 5.6	15.7 \pm 4.0	30.4 \pm 9.2	18.8 \pm 5.0
HU values	70.9 \pm 15.0	70.5 \pm 16.9	70.6 \pm 16.0	71.2 \pm 16.0	71.0 \pm 16.0	70.1 \pm 16.0	70.1 \pm 16.0
Abdominal Aorta							
Objective noise	17.4 \pm 4.2	20.5 \pm 5.4	16.0 \pm 3.8	24.8 \pm 6.2	18.5 \pm 4.2	34.3 \pm 9.3	22.0 \pm 6.0
HU values	80.5 \pm 29.0	81.6 \pm 37.0	81.5 \pm 31.0	82.0 \pm 33.7	82.1 \pm 33.0	80.3 \pm 31.0	80.0 \pm 31.0

Objective image noise was decreased in non-linear adaptive filters processed image as opposed to unprocessed image series with no significant change in average HU values. Unpro: Unprocessed; Pro: Processed.

Table 3 Weight and maximum transverse diameter distribution of number of subjects with acceptable and unacceptable subjective image noise in abdominal computed tomography examinations for unprocessed and non-linear adaptive filters processed image series at 150, 100 and 50 mAs tube current-time product levels (mean \pm SD)

	Unprocessed images		Processed images	
	Acceptable noise	Unacceptable noise	Acceptable noise	Unacceptable noise
150 mAs	14/19	5/19	19/19	0/19
Weight (kg)	74.5 \pm 14.8	95.2 \pm 11.1	79.9 \pm 16.5	-
Transverse diameter (cm)	34.2 \pm 4.3	42.9 \pm 4.5	36.5 \pm 5.8	-
100 mAs	4/19	15/19	17/19	2/19
Weight (kg)	77.1 \pm 4.0	80.7 \pm 18.6	76.9 \pm 14.6	106.0 \pm 4.3
Transverse diameter (cm)	32.5 \pm 3.5	37.6 \pm 5.9	35.7 \pm 5.6	43.5 \pm 0.7
50 mAs	0/19	19/19	5/19	14/19
Weight (kg)	-	79.9 \pm 16.5	66.2 \pm 13.0	91.4 \pm 15.1
Transverse diameter (cm)	-	36.5 \pm 5.8	33.0 \pm 3.4	40.6 \pm 6.1

Subjects with unacceptable image noise in processed images were significantly heavier and had greater transverse diameter than subjects with acceptable image noise.

19 image series at 50 and 100 mAs. These artifacts were minor and did not interfere with diagnostic confidence. Diagnostic confidence was suboptimal on unprocessed images at 100 mAs and it improved to fully acceptable in NLAF processed image series at 100 mAs. At 50 mAs both unprocessed and processed images were rated as unacceptable for diagnostic confidence. Weight distribution of subjects with acceptable and unacceptable image noise in both unprocessed and processed images is summarized in Table 2.

Objective image quality

Detailed objective image quality scores for abdominal CT have been summarized in Table 3. Average objective image noise (\pm standard deviation of the average) in the liver was decreased by 21% (14.4 \pm 4/18.2 \pm 4.9) at 150 mAs, by 29% (15.7 \pm 4/21.9 \pm 5.6) at 100 mAs and by 39.4% (18.8 \pm 5.7/30.4 \pm 9.2) at 50 mAs processed images as compared to unprocessed image series at corresponding mAs levels ($P < 0.0001$), whereas in the abdominal aorta noise decreased by 22% (16 \pm 3.8/20.5 \pm 5.4) at 150 mAs, by 26% (18.5 \pm 4.2/24.8 \pm 6.2) at 100 mAs and by 38% (22 \pm 6/34.3 \pm 9.3) at 50 mAs processed images ($P < 0.0001$).

There was no significant change in the average CT number (for liver and aorta) in unprocessed and processed abdominal CT image series ($P > 0.05$).

Radiation doses

CTDIvol for abdominal CT image series at 200 mAs, 150 mAs, 100 mAs and 50 mAs were 16.8, 12.6, 8.4, 4.2 mGy, respectively. The respective DLP values were 245.6, 141.8, 95.7, and 49.7 mGy-cm.

DISCUSSION

Since lowering of radiation dose increases the image noise, an approach to reduce radiation dose associated with CT is to post process low dose noisy images in order to lower image noise and enhance diagnostic confidence. In the CT source data domain, users can change the CT image reconstruction technique; for example, filtered back projection with smoother or sharper reconstruction kernel. Use of smoother kernel does entail some loss of spatial resolution or image sharpness, whereas use of sharper kernels increases image noise at the expense of higher spatial resolution and improved image sharpness. Recent studies and commercial release of iterative reconstruction techniques allows scanning at lower radiation dose, as these techniques provide images with less image noise^[21-23]. However, presently these iterative reconstruction techniques are somewhat slower in reconstruction time and are only available on the latest high end (64 slices or higher) CT scanners with substantial cost increments for both hardware and software upgrades. On the

other hand, image post processing filters have also been developed to lower image noise^[12-14]. These filters work in the DICOM image space domain and are less computationally intense compared to the iterative reconstruction techniques. Unlike the iterative reconstruction techniques, which are applied to the CT scanner user interface, NLAF used in our study is a server-based application that identifies and processes low dose CT images automatically as they transit from CT user interface to the PACS network. To the best of our knowledge, there is no head to head comparison available to date between the iterative reconstruction techniques and the image post-processing filters.

Different types of image post processing filters have been used to reduce image noise in low radiation dose CT images^[12-14]. We used a NLAF for the purpose of our study. For abdominal CT images, NLAF post processing of 100 mAs image series changed image noise to acceptable from unacceptable in unprocessed images. However at 50 mAs, both processed and unprocessed images were found to be suboptimal. Lowering of image noise with NLAF did not affect the image contrast or lesion conspicuity in abdominal CT images. This trend was confirmed with objective image noise measurements in abdominal CT images. In addition to lowering of image noise, NLAF enhanced the visibility of smaller structures at 100 mAs. Our results are in contradiction to prior non-linear filters described by Kalra *et al*^[11-13]. Contrary to the loss of visibility of small structures and demeaned lesion conspicuity noted on prior studies, NLAF used in our study was not associated with these disadvantages. Hence, application of NLAF in abdominal CT allows radiation dose reduction while maintaining constant image quality and diagnostic confidence.

Our findings are consistent with those reported in a phantom study performed by Funama *et al*^[14], who found that 80 to 100 mAs images were acceptable following post processing with a different vendor's NLAF. We believe that the inherently high contrast in the chest from air and fat helped in achieving greater dose reduction with NLAF. In another study, Funama *et al*^[19] found that adaptive filters can improve image noise and diagnostic acceptability of abdominal CT images acquired at 60 to 100 mAs based on the size of the patients. We also noted that 5/19 abdominal CT images acquired at 50 mAs in subjects weighing less than 66 kg were acceptable, whereas the subjects with unacceptable image quality at 50 mAs were considerably heavier (weight greater than 91 kg) ($P < 0.0001$).

Results of our study are also in agreement with Kröpil *et al*^[18], who used the same NLAF as in our study to post process simulated upper abdomen MDCT phantom images and found that 50% radiation dose reduction is possible with post processing. We also found that image noise in 100 mAs abdominal CT images following post processing is similar to image noise in unprocessed 200 mAs images. Our results are also similar to another phantom study from Martinsen *et al*^[15], also using the

same NLAF, which showed acceptable lowering of tube current-time product down to only 112 mAs for detection of 2 mm-7 mm simulated liver lesions.

Our study has limitations. Foremost, the small sample size of our study is due to the difficulty in recruiting patients, which could be due to many reasons, such as rising concern of radiation-induced cancer. Another limitation of our study is that we did not use automatic exposure technique to evaluate the effect of NLAF on radiation dose reduction, although automatic exposure control techniques are routinely used for dose modulation in routine clinical practice. We used fixed tube current settings to reduce radiation dose for the following reasons: firstly, to obtain four levels of radiation dose with automatic exposure control, we would have been required to adjust the noise index (desired image noise for adjusting tube current) and minimum and maximum tube current for each dose level as well as for different patient size, as automatic exposure control would have increased radiation dose to larger subjects and decreased the radiation dose for slimmer subjects. To further complicate the matter, change in radiation dose with automatic exposure control is non-linear to the body size in order to avoid inadvertent use of high tube currents in larger subjects and too low tube currents in slimmer subjects.

Also, we did not investigate the effect of NLAF post processing in patients of different sizes due to our small sample size. Although it is very difficult to blind the experienced radiologist between unprocessed and processed images due to differences in image noise, we randomized the image sets acquired at varying dose levels (16.8-4.2 mGy). Another possible limitation of our study is the fact that CT images were acquired in equilibrium phase and not in non-contrast or dynamic phase. An additional consideration with our study is the fact that we used 4 image datasets of each patient at four different radiation dose levels and this repetitive reviewing of images may have biased the radiologists for the lesion conspicuity assessment component of our study. However, in order to minimize this bias in image assessment, each radiologist was asked separately to first assess the lesion conspicuity on the image series with the greatest image noise or those image datasets acquired at lowest dose levels and then assess the other dose levels. Although NLAF works on DICOM images from all vendors, we did not perform side by side comparisons for the role of NLAF on CT images from other vendors. Also, we did not compare NLAF filters with other available commercial CT image filters.

Implications of our study include potential for reducing radiation dose by 50% with the application of NLAF as used in our study. Further studies will however be needed to determine the actual noise reduction effect of NLAF on patients of different sizes, in particular for large patients.

In conclusion, substantial CT radiation dose reduction is feasible for abdominal CT images (down to 100 mAs) following processing with NLAF.

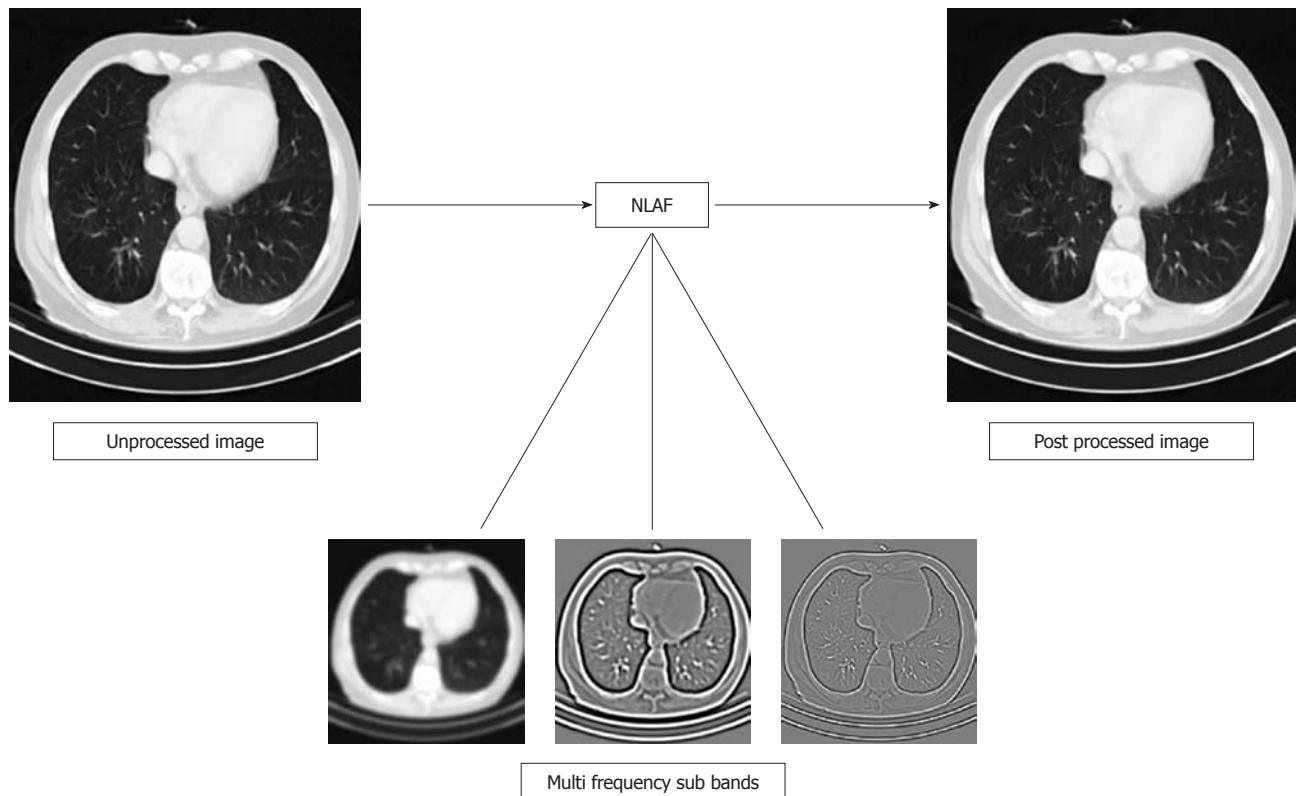


Figure 2 Non-linear adaptive filters divides the original image into a number of frequency bands, which are processed separately and ultimately re-combined into a resultant final image. NLAF: Non-linear adaptive filters.

APPENDIX

The two dimensional NLAF used in this study are based on the General Operator Processor technology^[24]. The algorithm divides the data into several frequency bands that are processed separately and then re-combined. The number of frequency bands varies between cases, depending on the scanner and anatomy of intent (as described in Figure 2, where chest image has been parsed into three frequency bands). Each band usually contains similar size structures, which allows it to process anatomical structures by size. The low-pass band on the left consists mainly of the amplitude of the 2D signal and low frequent variations. The high-pass band contains predominantly small structures and noise. The remaining band cover structures of mid size and low frequency noise. After processing each frequency band, NLAF adaptively combines the enhanced bands to yield a resultant filtered image.

During the filter's hierarchical process, each pixel is examined in relation to its surroundings. Local features are estimated by using a set of filters in different directions. The filters are designed so that the combined filter response is completely rotational invariant. During the analysis of the filter responses a number of simple, complex and hypercomplex features are estimated. These features can be for example variance, orientation, phase, energy and curvature. When a local NLAF feature has been estimated, the feature is estimated also on a higher abstraction level to get robust results for the neighbour-

hood. From this information one can decide if the pixel is part of the same structure as its neighbours. Moreover, certainty values on the feature estimations are always generated to further obtain robust results. One example is two crossing lines where there is high signal energy in the crossing point but low certainty on orientation since there is more than one orientation present.

The compiled set of these features forms the contextual information for every location in the image. This contextual information is fused to generate a specific filtering method, which adapts to the image signal in every location and individually optimizes each pixel. The unique nature of NLAF is the possibility of adapting desired behavior to the image content, allowing for simultaneous noise reduction and edge enhancement. For example, edge enhancement in high frequency areas such as lung and bones, and selective noise reduction in other soft tissue regions within a single image. Finally, the parameters may be adjusted for the anatomical region scanned, as for example the abdominal CT images (more noise reduction or smoothing is required) need different parameters than those needed in chest images (where greater edge enhancement with limited smoothing is required). The enhancement is performed in different intensity value ranges, corresponding to tissue-type-specific Hounsfield Units. Also these parameters can be adjusted based on user preference, as some radiologists prefer smooth images while others prefer sharp, crisp images.

COMMENTS

Background

As the use of computed tomography (CT) is increasing, with an estimated 62 million scans per year in the United States in the year 2006, the concerns associated with radiation exposure have also increased in both the news media and the medical literature. The primary concern of radiation dose associated with CT scanning is radiation-induced carcinogenesis. The probability of radiation-induced cancer is directly related to the radiation dose absorbed by tissues and organs and hence the reduction of dose is of paramount importance. In CT, reduction of dose results in images with larger image noise or mottle and hence raises the possibility of missing lesions or other diagnostic findings. Efforts have been made to reduce radiation dose while maintaining image quality which have led to several changes in CT hardware and software technologies. From the software point of view, image post processing with linear and non-linear filters have been developed and assessed for lowering image noise and improving or maintaining lesion conspicuity on low dose images. Previous clinical studies have reported the use of non-linear image filters for reducing radiation dose for chest and abdominal CT examinations. However, some of these filters lower image noise at the expense of image contrast or visibility of smaller structures. New non-linear adaptive filters (NLAF) have been developed and studied using phantom and simulated CT images.

Innovations and breakthroughs

Substantial CT radiation dose reduction is feasible for abdominal CT images (down to 100 mAs) following processing with NLAF.

Applications

Implications of our study include potential for reducing radiation dose by 50% with the application of NLAF as used in our study. Further studies will however be needed to determine the actual noise reduction effect of NLAF on patients of different sizes, in particular for large patients.

Peer review

This study presents the results of the application of NLAF software to abdominal CT images and demonstrates the prospect of dose reduction that can be achieved with the use of such filters. Overall, this is a very good paper. It is well designed, well implemented and well analyzed.

REFERENCES

- 1 Department of Health and Human Services. What's NEXT? Nationwide Evaluation of X-ray Trends: 2000 computed tomography. (CRCPD publication no. NEXT_2000CT-T.) Conference of Radiation Control Program Directors, 2006
- 2 Medical Information Division. IMV 2006 CT Market Summary Report. Des Plaines, IL: IMV Medical Information Division, 2006
- 3 Guthrie C. How dangerous are CT scans? Time Magazine. New York: Time Inc., 2008 Available from: URL: <http://www.time.com/time/health/article/0,8599,1818520,00.html> on January 17th 2011
- 4 Brenner DJ, Hall EJ. Computed tomography--an increasing source of radiation exposure. *N Engl J Med* 2007; **357**: 2277-2284
- 5 Kalra MK, Maher MM, Toth TL, Hamberg LM, Blake MA, Shepard JA, Saini S. Strategies for CT radiation dose optimization. *Radiology* 2004; **230**: 619-628
- 6 Rizzo S, Kalra M, Schmidt B, Dalal T, Suess C, Flohr T, Blake M, Saini S. Comparison of angular and combined automatic tube current modulation techniques with constant tube current CT of the abdomen and pelvis. *AJR Am J Roentgenol* 2006; **186**: 673-679
- 7 Singh S, Kalra MK, Moore MA, Shailam R, Liu B, Toth TL, Grant E, Westra SJ. Dose reduction and compliance with pediatric CT protocols adapted to patient size, clinical indication, and number of prior studies. *Radiology* 2009; **252**: 200-208
- 8 Cohnen M, Fischer H, Hamacher J, Lins E, Kötter R, Mödder U. CT of the head by use of reduced current and kilovolt-

age: relationship between image quality and dose reduction. *AJNR Am J Neuroradiol* 2000; **21**: 1654-1660

- 9 Keselbrener L, Shimoni Y, Akselrod S. Nonlinear filters applied on computerized axial tomography: theory and phantom images. *Med Phys* 1992; **19**: 1057-1064
- 10 Alvarez RE, Stonestrom JP. Optimal processing of computed tomography images using experimentally measured noise properties. *J Comput Assist Tomogr* 1979; **3**: 77-84
- 11 Kalra MK, Maher MM, Sahani DV, Blake MA, Hahn PF, Avinash GB, Toth TL, Halpern E, Saini S. Low-dose CT of the abdomen: evaluation of image improvement with use of noise reduction filters pilot study. *Radiology* 2003; **228**: 251-256
- 12 Rizzo SM, Kalra MK, Schmidt B, Raupach R, Maher MM, Blake MA, Saini S. CT images of abdomen and pelvis: effect of nonlinear three-dimensional optimized reconstruction algorithm on image quality and lesion characteristics. *Radiology* 2005; **237**: 309-315
- 13 Kalra MK, Maher MM, Blake MA, Lucey BC, Karau K, Toth TL, Avinash G, Halpern EF, Saini S. Detection and characterization of lesions on low-radiation-dose abdominal CT images postprocessed with noise reduction filters. *Radiology* 2004; **232**: 791-797
- 14 Funama Y, Awai K, Miyazaki O, Nakayama Y, Goto T, Omi Y, Shimonobo T, Liu D, Yamashita Y, Hori S. Improvement of low-contrast detectability in low-dose hepatic multidetector computed tomography using a novel adaptive filter: evaluation with a computer-simulated liver including tumors. *Invest Radiol* 2006; **41**: 1-7
- 15 Martinsen AC, Saether HK, Olsen DR, Skaane P, Olerud HM. Reduction in dose from CT examinations of liver lesions with a new postprocessing filter: a ROC phantom study. *Acta Radiol* 2008; **49**: 303-309
- 16 Okumura M, Ota T, Tsukagoshi S, Katada K. New method of evaluating edge-preserving adaptive filters for computed tomography (CT): digital phantom method. *Nihon Hoshasen Gijutsu Gakkai Zasshi* 2006; **62**: 971-978
- 17 Sato K, Goto M, Ishiya H, Oshita R, Mori I, Yanagawa I. [Evaluation of non-linear adaptive smoothing filter by digital phantom]. *Nihon Hoshasen Gijutsu Gakkai Zasshi* 2008; **64**: 434-441
- 18 Kröpil P, Lanzman RS, Walther C, Röhlen S, Godehardt E, Mödder U, Cohnen M. [Dose reduction and image quality in MDCT of the upper abdomen: potential of an adaptive post-processing filter]. *Rofo* 2010; **182**: 248-253
- 19 Funama Y, Awai K, Miyazaki O, Goto T, Nakayama Y, Shimamura M, Hiraishi K, Hori S, Yamashita Y. Radiation dose reduction in hepatic multidetector computed tomography with a novel adaptive noise reduction filter. *Radiat Med* 2008; **26**: 171-177
- 20 EUR 16262. European guidelines on quality criteria for computed tomography. Available from: URL: <http://www.drs.dk/guidelines/ct/quality>
- 21 Singh S, Kalra MK, Gilman MD, Hsieh J, Pien HH, Digumarthy SR, Shepard JA. Adaptive statistical iterative reconstruction technique for radiation dose reduction in chest CT: a pilot study. *Radiology* 2011; **259**: 565-573
- 22 Singh S, Kalra MK, Hsieh J, Licato PE, Do S, Pien HH, Blake MA. Abdominal CT: comparison of adaptive statistical iterative and filtered back projection reconstruction techniques. *Radiology* 2010; **257**: 373-383
- 23 Funama Y, Taguchi K, Utsunomiya D, Oda S, Yanaga Y, Yamashita Y, Awai K. Combination of a low-tube-voltage technique with hybrid iterative reconstruction (iDose) algorithm at coronary computed tomographic angiography. *J Comput Assist Tomogr* 2011; **35**: 480-485
- 24 Granlund GH. In search of a general picture processing operator. *Comput Graph Image Process* 1978; **8**: 155-173

S- Editor Cheng JX L- Editor Logan S E- Editor Zheng XM



Aortic ostia of the bronchial arteries and tracheal bifurcation: MDCT analysis

Julaii Ziyawudong, Nobuyuki Kawai, Morio Sato, Akira Ikoma, Hiroki Sanda, Taizo Takeuchi, Hiroki Minamiguchi, Motoki Nakai, Takami Tanaka, Tetsuo Sonomura

Julaii Ziyawudong, Nobuyuki Kawai, Morio Sato, Akira Ikoma, Hiroki Sanda, Taizo Takeuchi, Hiroki Minamiguchi, Motoki Nakai, Takami Tanaka, Tetsuo Sonomura, Department of Radiology, Wakayama Medical University, 811-1 Kimiidera, Wakayamashi, Wakayama 641-8510, Japan

Author contributions: Ziyawudong J and Kawai N performed the research; Ikoma A, Sanda H, Takeuchi T, Minamiguchi H, Nakai M, Tanaka T and Sonomura T analyzed the data; Ziyawudong J and Sato M wrote the paper.

Correspondence to: **Morio Sato, MD**, Department of Radiology, Wakayama Medical University, 811-1 Kimiidera, Wakayamashi, Wakayama 641-8510, Japan. morisato@mail.wakayama-med.ac.jp
Telephone: +81-73-4443110 Fax: +81-73-4410604

Received: July 8, 2011 Revised: September 21, 2011

Accepted: September 28, 2011

Published online: January 28, 2012

Abstract

AIM: To explore the anatomical relationships between bronchial artery and tracheal bifurcation using computed tomography angiography (CTA).

METHODS: One hundred consecutive patients (84 men, 16 women; aged 46-85 years) who underwent CTA using multi-detector row CT (MDCT) were investigated retrospectively. The distance between sites of bronchial artery ostia and tracheal bifurcation, and dividing directions were explored. The directions of division from the descending aorta were described as on a clock face.

RESULTS: We identified ostia of 198 bronchial arteries: 95 right bronchial arteries, 67 left bronchial arteries, 36 common trunk arteries. Of these, 172 (87%) divided from the descending aorta, 25 (13%) from the aortic arch, and 1 (0.5%) from the left subclavian artery. The right, left, and common trunk bronchial arteries divided at -1 to 2 cm from tracheal bifurcation with frequencies of 77% (73/95), 82% (54/66), and 70% (25/36), respectively. The dividing direction of right bronchial

arteries from the descending aorta was 9 to 10 o'clock with a frequency of 81% (64/79); that of left and common tract bronchial arteries was 11 to 1 o'clock with frequencies of 70% (43/62) and 77% (24/31), respectively.

CONCLUSION: CTA using MDCT provides details of the relation between bronchial artery ostia and tracheal bifurcation.

© 2012 Baishideng. All rights reserved.

Key words: Anatomy; Computed tomography; Bronchial artery; Medical imaging; Tracheal bifurcation

Peer reviewer: Ender Uysal, MD, Sisli Etfal Training and Research Hospital, Clinic of Radiology, Sisli Etfal Eğitim ve Araştırma Hastanesi Radyoloji Kliniği, Etfal sok. Sisli, Istanbul 34377, Turkey

Ziyawudong J, Kawai N, Sato M, Ikoma A, Sanda H, Takeuchi T, Minamiguchi H, Nakai M, Tanaka T, Sonomura T. Aortic ostia of the bronchial arteries and tracheal bifurcation: MDCT analysis. *World J Radiol* 2012; 4(1): 29-35 Available from: URL: <http://www.wjgnet.com/1949-8470/full/v4/i1/29.htm> DOI: <http://dx.doi.org/10.4329/wjr.v4.i1.29>

INTRODUCTION

Following recent advances in multi-detector row computed tomography (MDCT), which enables rapid visualization of thin-slice images with good resolution, computed tomography angiography (CTA) with MDCT is increasingly being used to identify the artery responsible for hemoptysis^[1-6]. Although in some instances non-bronchial arteries are involved in hemoptysis^[1,7,8], the main source of hemoptysis is a bronchial artery^[9]. Most interventional radiologists would be familiar with the dividing sites of the bronchial arteries based on their experience and

on trial and error, but they may encounter difficulty in catheterization of the bronchial artery. The relationships between the origin of bronchial arteries and the thoracic vertebrae are known from early studies^[10,11]. Remy-Jardin *et al.*^[1] coded bronchial arteries originating from the descending aorta between the T5 and T6 vertebral levels as orthotopic, and those originating outside levels T5-T6 as ectopic. However, because the tracheal bifurcation is visible fluoroscopically but the exact thoracic vertebral level is difficult to identify, it is clinically useful to know how the bronchial artery ostia relate to tracheal bifurcation rather than to the thoracic vertebrae. Dilatation of bronchial arteries and the development of collateral arteries are observed in patients with hemoptysis^[1-4]. In the present study, we explored the intact relation between bronchial artery ostia and tracheal bifurcation among a population with no cause to have enlarged bronchial arteries.

The purpose of this study is to explore the anatomical relationships between bronchial artery ostia and tracheal bifurcation using CTA with MDCT.

MATERIALS AND METHODS

Patients

The study was approved by the Ethics Committee of our institution, and informed consent was obtained from all patients. One hundred consecutive patients (84 men, 16 women; mean age, 68.6 years; age range, 46-85 years) with esophageal cancer who received dynamic CT between February 2009 and May 2010 were investigated retrospectively. No patient had an episode of hemoptysis; all underwent contrast-enhanced helical MDCT of the thorax for the purpose of identifying the esophageal and bronchial arteries prior to surgical treatment. The relation between the tracheal bifurcation and the bronchial arteries was analyzed using the same data that are obtained in MDCT of the thorax at our institute. Care was taken to avoid administration of contrast medium to patients with renal insufficiency (creatinine level > 1.5 mg/L) or iodine allergy.

MDCT protocol and contrast medium injection

CTA was conducted using an MDCT scanner (Light-Speed VCT 64, General Electric Healthcare, Milwaukee, WI) with a 64 mm × 0.625 mm detector configuration in which interspaced helical data sets were collected from 64 detector rows. The following parameters were used for unenhanced CT and the two phases of contrast-enhanced CT: gantry rotation speed of 0.5 s per rotation, 0.5 mm collimation, 15 mm/s table increment with helical pitch of 15, tube voltage of 120 kV, and tube current of 300 mA. Axial sections (0.5 mm thickness) were reconstructed at 0.5 mm intervals. The following MDCT protocol was employed for evaluation of the thorax. Using an automatic injector (Dual Shot GX, Nemotokyorindo, Tokyo, Japan), each patient received an intravenous bolus of non-ionic contrast medium at 580 mg I/kg of patient body

weight, containing 300 mg I/mL (Omnipaque, Daiichisankyo Pharmaceutical, Tokyo, Japan), for a duration of 25 s, through a 20-gauge angiocatheter placed in the antecubital vein.

The automatic bolus tracking method was used with Smart Prep software (GE Healthcare) to monitor contrast enhancement after injection of contrast medium. Unenhanced scans were obtained initially, and a region-of-interest cursor for bolus tracking was then placed in the ascending aorta. Scans were obtained from the level of the thoracic inlet to the caudal edge of the kidney. The triggering threshold CT value was set at 200 HU, and real-time low-dose (120 kVp, 50 mA) serial scanning for monitoring began 6 s after the start of the contrast medium injection. Two phases (arterial and venous) were obtained during breath-holding in each. The arterial phase was automatically performed after the CT value reached the triggering threshold of 200 HU. The following images were systematically reconstructed from the arterial phase data: contiguous transverse scans of thickness 0.5 mm viewed on mediastinal and lung window settings, oblique coronal and sagittal maximum intensity projections (MIPs), and three-dimensional volume-rendered images of the thoracic vascular structures. The venous phase was not utilized in this study.

Data analysis and image interpretation

The large number of images was interpreted at a remote workstation and analyzed using Aquarius NET (TeraRecon, San Mateo, CA). Three radiologists, each with 3 to 15 years of experience in CT image interpretation, performed image evaluation in consensus. CT values were measured at four points in the aorta: at the level of the ascending aorta, arch, descending aorta, and diaphragm. CT interpretation focused on evaluation of the bilateral bronchial arteries. Transverse slices from thoracic CTA were used in combination with the multiplanar reformatting images to identify dividing of the bronchial artery from the thoracic aorta and the aortic arch. The borderline between the aortic arch and the descending aorta was defined as the bottom of the aortic arch, as delineated on thoracic CT. The distance between this borderline and the line of tracheal bifurcation was measured. The level of tracheal bifurcation was termed '0 level'. Positive values were defined as the cranial distance from the tracheal bifurcation and negative values as the caudal distance. Arteries that progressed along the bronchus were identified as bronchial arteries. All bronchial arteries dividing from the aortic arch and descending aorta were followed using the transverse slice images. If the bronchial arteries could not be identified, three-dimensional MIP reformatted images in the coronal, sagittal, and oblique planes were used to search for tortuous bronchial arteries as they followed the bronchial tree from their origin at the aorta or other systemic artery. The frequency of intercosto-bronchial trunk was explored because the anterior spinal artery can arise from an intercosto-bronchial artery, and thus must be identified.

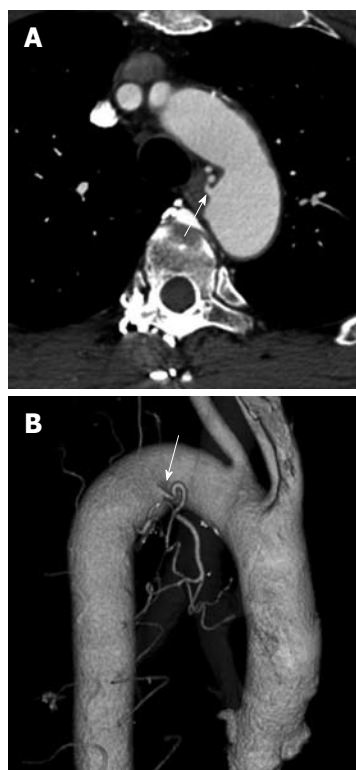


Figure 1 Common trunk of the right and left bronchial arteries from the aortic arch is indicated by arrows on an axial computed tomography image with mediastinal soft-tissue window settings (A) and on a thin-section maximum intensity projection image of a three-dimensional volumetric reformatted image (B).

First, dividing sites of the bronchial arteries from the aorta, dividing style (genuine or common trunk), and the number of bronchial arteries were explored. Second, the distance between the site of bronchial artery dividing and tracheal bifurcation was measured on the transverse 0.5 mm thick slices. Third, the dividing directions of the bronchial arteries from the descending aorta were explored using the transverse slice images. The directions of division from the descending aorta were described in terms of positions of the numbers on a clock face. In bronchial arteries that divided from the aortic arch, the dividing directions were described as right caudal, middle caudal, and left caudal.

RESULTS

CT values in the aorta

In the 100 subjects, mean CT values (HU) at the level of the ascending aorta, aortic arch, descending aorta, and diaphragm were 389 ± 71 , 364 ± 65 , 374 ± 66 , and 353 ± 68 , respectively.

Aortic sites of bronchial artery ostia

We identified 198 aortic sites of bronchial artery ostia in the 100 subjects. Of these, 172 (87%) divided from the descending aorta, 25 (13%) from the aortic arch (Figure 1), and 1 (0.5%) from the left subclavian artery (Figure 2).

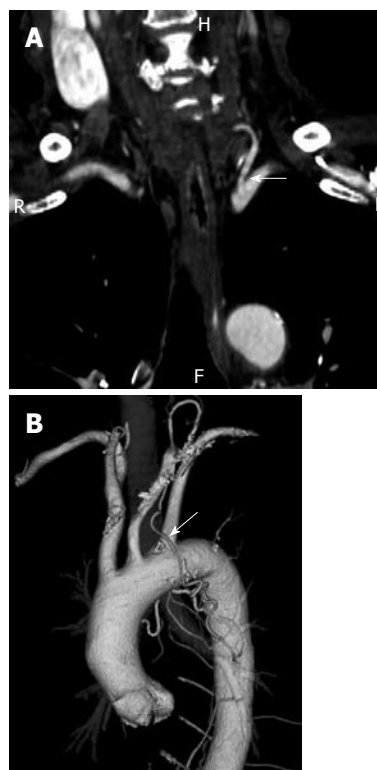


Figure 2 Left bronchial artery arising from the left subclavian artery is indicated by arrows on a reformatted coronal computed tomography image with mediastinal soft-tissue lung window settings (A) and on a thin-section maximum intensity projection image of a three-dimensional volumetric reformatted image (B).

Dividing style of right and left bronchial arteries, and frequency of intercostal artery sub-branching

Of the 198 dividing sites, 95 divided as right bronchial arteries, 67 as left bronchial arteries, and 36 as a common trunk of right and left bronchial arteries. Of the 95 right bronchial arteries, 28 divided independently as a genuine right branch and 67 (71%) divided as a common trunk of right bronchial and intercostal arteries (Figure 3). Of the 67 left bronchial arteries, 65 divided independently as a genuine left branch and 2 (3%) divided as a common trunk of left bronchial and intercostals arteries. Of the 36 common trunk arteries, 34 divided as a common trunk of right and left bronchial arteries, and 2 (6%) divided as a common trunk of right and left bronchial arteries, and intercostal arteries. No anterior spinal artery was delineated from intercostal arteries that divided from either common trunk.

Identified numbers of right and left bronchial arteries

We could not identify a right bronchial artery in 1 subject or a left bronchial artery in 9 subjects. A total of 234 bronchial arteries were identified: 131 (95 plus 36) right bronchial arteries, and 103 (67 plus 36) left bronchial arteries.

A singular right bronchial artery was observed in 68 subjects, dual right bronchial arteries in 30 subjects, and triple right bronchial arteries in 1 subject. The average

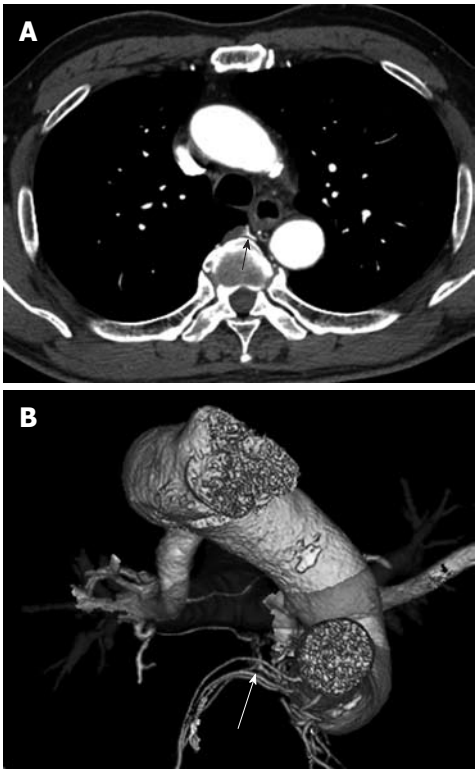


Figure 3 Right bronchial artery branches with an intercostal artery (arrow) at the approximate ventral center of the thoracic vertebra, shown on an axial computed tomography scan with mediastinal soft-tissue window settings (A) and on a thin-section maximum intensity projection image of a 3D volumetric reformatted image (B).

number of right bronchial arteries was 1.31 per subject. A singular left bronchial artery was observed in 79 subjects and dual left bronchial arteries in 12 subjects. The average number of left bronchial arteries was 1.03 per person.

Dividing sites of bronchial arteries related to tracheal bifurcation and their dividing directions

Of the 234 bronchial arteries, 15 divided from the aortic arch and 219 divided from the descending aorta. The mean border line between the aortic arch and descending aorta was at the level 18.4 ± 7.4 mm cranial to the tracheal bifurcation in the 100 subjects.

Figure 4 shows the relation between the right bronchial artery ostia and the tracheal bifurcation. Of the 95 right bronchial arteries, 29 (31%) divided at a level 0-1 cm cranial to the bifurcation, 60 (64%) at 0-2 cm cranial, and 13 (13%) at -1 to 0 cm caudal to the bifurcation. A total of 73 (77%) right bronchial arteries divided at between -1 and 2 cm from the bifurcation (Table 1).

The dividing directions of the right bronchial arteries are shown in Figure 4. Of the 79 right bronchial arteries that divided from the descending aorta, 64 (81%) divided in the direction of 9 to 10 o'clock (Table 2). Of the 16 right bronchial arteries that divided from the aortic arch, 13 (81%) divided in the right caudal direction, 2 in the left caudal direction, and 1 in the central caudal direction (Table 3).

Table 1 Relation between bronchial arteries ostia from aorta and tracheal bifurcation <i>n</i> (%)			
Level from tracheal bifurcation (cm)	Right bronchial artery	Left bronchial artery	Common tract artery
≥ 4, < 4.5	0 (0)	0 (0)	2 (6)
≥ 3.5, < 4	2 (2)	0 (0)	1 (3)
≥ 3, < 3.5	0 (0)	0 (0)	0 (0)
≥ 2.5, < 3	7 (7)	5 (8)	2 (6)
≥ 2, < 2.5	7 (7)	4 (6)	2 (6)
≥ 1.5, < 2	14 (15)	9 (14)	3 (8)
≥ 1, < 1.5	17 (18)	3 (5)	6 (17)
≥ 0.5, < 1	15 (16)	10 (15)	2 (6)
≥ 0, < 0.5	14 (15)	20 (30)	7 (19)
≥ -0.5, < 0	6 (6)	6 (9)	1 (3)
≥ -1, < -0.5	7 (7)	6 (9)	6 (17)
≥ -1.5, < -1	3 (3)	0 (0)	4 (11)
≥ -2, < -1.5	1 (1)	3 (5)	0 (0)
≥ -2.5, < -2	0 (0)	0 (0)	0 (0)
≥ -3, < -2.5	2 (2)	0 (0)	0 (0)
Total (<i>n</i> = 197)	95	66	36

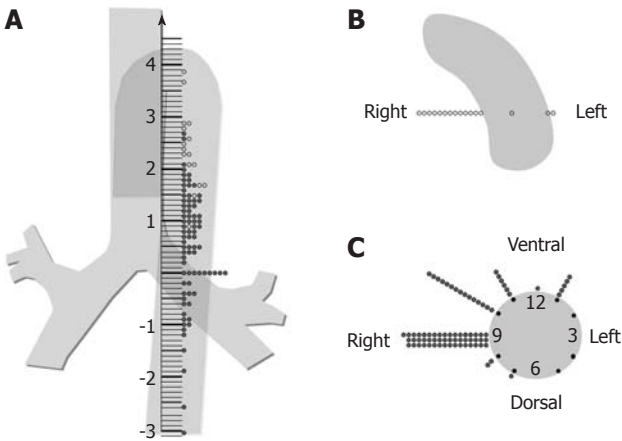


Figure 4 Diagram showing the relation of the tracheal bifurcation to the right bronchial artery ostia, coronal aspect (A), and dividing directions of the right bronchial artery from the aortic arch (B) and from the descending aorta (C), axial aspect.

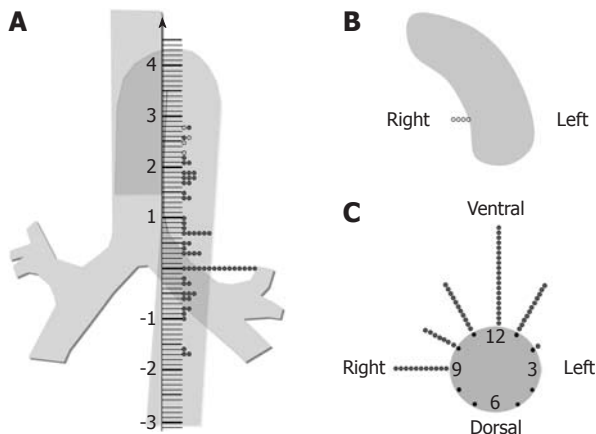
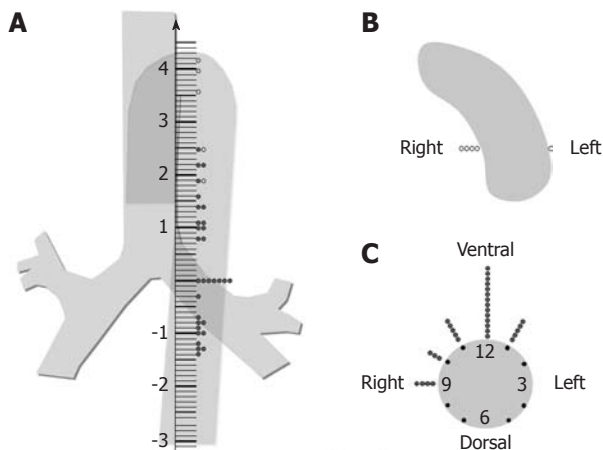
Figure 5 shows the relation between the left bronchial artery ostia and the tracheal bifurcation. Of the 66 left bronchial arteries, 33 (50%) divided at a level 0-1 cm cranial to the bifurcation, 42 (64%) at 0-2 cm cranial, and 12 (18%) at -1 to 0 cm caudal to the bifurcation. A total of 54 (82%) left bronchial arteries divided at between -1 and 2 cm from the bifurcation.

The dividing directions of the left bronchial artery are shown in Figure 5. Of the 62 left bronchial arteries that divided from the descending aorta, 43 (70%) divided in the direction of 11 to 1 o'clock and 18 (29%) divided at the direction of 9 to 10 o'clock (Table 2). All 4 of the left bronchial arteries that divided from the aortic arch did so in the right caudal direction (Table 3).

The relation between the ostia of the aortic common trunk bronchial arteries and the tracheal bifurcation is shown in Figure 6. Of the 36 common tract bronchial arteries, 9 (25%) divided at a level 0-1 cm cranial to the bifurcation, 18 (50%) at 0-2 cm cranial, and 7 (20%) at -1 to 0 cm caudal to the bifurcation. A total of 25 (70%)

Table 2 Dividing direction of bronchial arteries from descending aorta *n* (%)

Artery	Time o'clock direction								Total
	7	8	9	10	11	12	1	2	
Right bronchial	1 (1)	2 (3)	49 (62)	15 (19)	6 (8)	1 (1)	5 (6)	0 (0)	79
Left bronchial	0 (0)	0 (0)	11 (18)	7 (11)	11 (18)	21 (34)	11 (18)	1 (2)	62
Common tract	0 (0)	0 (0)	4 (13)	3 (10)	5 (16)	14 (45)	5 (16)	0 (0)	31

**Figure 5** Diagram showing the relation of the tracheal bifurcation to the left bronchial artery ostia, coronal aspect (A), and dividing directions of the left bronchial artery from aortic arch (B) and from the descending aorta (C), axial aspect.**Figure 6** Diagram showing the relation of the tracheal bifurcation to common trunk ostia of the right and left bronchial arteries, coronal aspect (A), dividing directions of the common trunk from the aortic arch (B) and from the descending aorta (C), axial aspect.

common tract bronchial arteries divided at a level between -1 and 2 cm from the bifurcation.

The dividing directions of the common tract bronchial artery are shown in Figure 6. Of the 31 common tract bronchial arteries that divided from the descending aorta, 24 (77%) divided in the direction of 11 to 1 o'clock and 7 (23%) divided at the direction of 9 to 10 o'clock (Table 2). Of the 5 common tract bronchial arteries that divided from the aortic arch, 4 (80%) divided in the right caudal direction and 1 (20%) in the central caudal direction (Table 3).

Table 3 Dividing direction of bronchial arteries from aortic arch *n* (%)

Artery	Direction			Total
	Right caudal	Left caudal	Middle caudal	
Right bronchial	13 (81)	2 (13)	1 (6)	16
Left bronchial	4 (100)	0 (0)	0 (0)	4
Common tract	4 (80)	0 (0)	1 (20)	5

Table 4 Comparisons of bronchial artery findings between pathological and multi-detector row computed tomography studies *n* (%)

	Pathological study		MDCT study	
	Kasai <i>et al</i> ^[10]	Morita <i>et al</i> ^[5]	Present study	
Right bronchial artery	<i>n</i> = 161	<i>n</i> = 80	<i>n</i> = 96	
Direct origin from asrta	44 (27)	15 (19)	28 (29)	
Intercostal bronchial trunk	86 (53)	61 (76)	67 (70)	
Subclavian artery	31 (19)	4 (5)	1 (1)	
Left bronchial artery	<i>n</i> = 117	<i>n</i> = 67	<i>n</i> = 67	
Direct origin from asrta	111 (95)	63 (94)	65 (97)	
Intercostal bronchial trunk	1 (1)	4 (6)	2 (3)	
Subclavian artery	5 (4)	0	0	
Common trunk of both bronchial arteries	<i>n</i> = 65	<i>n</i> = 38	<i>n</i> = 36	
Direct origin from aorta	/	/	34 (94)	
Intercostal bronchial trunk	/	/	2 (6)	

Data are numbers of right, left and common trunk arteries. Numbers in parentheses are percentages. MDCT: Multidetector row computed tomography.

DISCUSSION

In a postmortem study, Cauldwell *et al*^[11] documented that bronchial arteries divided from the aortic arch with an incidence of 17.3%, compared with 13% in the present study. Most bronchial arteries divide from the aorta; however, they can also divide from sites such as the right subclavian artery, left subclavian artery, or their branches. The incidence of dividing from outside the aorta was 0.5% in the present study, 3.3% in a previous MDCT series^[5], and 15% in a previous pathological manuscript (Table 4)^[11]. Morita *et al*^[5] proposed that bronchial arteries arising from the subclavian arteries are likely to go unnoticed on MDCT because of their small diameter. Although limitations exist, the MDCT data regarding dividing sites, styles, and numbers of bronchial arteries are comparable with data acquired in previous postmortem series (Table 5). MDCT studies have the advantage of

Table 5 Numbers of bronchial arteries

	Kasai <i>et al.</i> ^[10] (<i>n</i> = 370)	Cauldwell <i>et al.</i> ^[11] (<i>n</i> = 467)	The present study (<i>n</i> = 234)
No. of right bronchial arteries			
0	0	0	1 (1)
1	13 (13)	100 (67)	68 (68)
2	57 (57)	48 (32)	30 (30)
3	22 (22)	1 (0.7)	1 (1)
4	6 (6)	1 (0.7)	0
No. of left bronchial arteries			
0	0	0	9 (9)
1	3 (31)	47 (31)	79 (79)
2	59 (59)	93 (62)	12 (12)
3	8 (8)	9 (6)	0
4	2 (2)	1 (0.7)	0

enabling exploration of the relation between the tracheal bifurcation and other body components. The present data (Table 4) regarding bronchial artery division from the aorta are similar to the basic data obtained by Morita *et al.*^[5], but they did not focus on the relation between the bronchial artery ostia and the tracheal bifurcation.

Previous pathological manuscripts noted that the border between the aortic arch and the descending aorta corresponds to the site of the left recurrent laryngeal nerve^[10,11] and that dividing sites of the bronchial arteries correspond to thoracic vertebral levels 5 to 6^[10,11]. However, this information is not always useful in the clinical situation of catheter insertion to the bronchial arteries because the position of the X-ray fluoroscopic field changes frequently during catheterization, causing problems in identification of each thoracic vertebral level. The tracheal bifurcation, however, is easily identified. The information obtained in the present study can be used as a reference regarding positioning of the bronchial artery ostia from the aorta with respect to tracheal bifurcation.

During bronchial arterial embolization, it is important to inhibit the migration of embolic material to the spinal artery^[7,9], which may occur because the anterior spinal artery communicates with the intercostal arteries. In the present MDCT series, we observed no communication between the anterior spinal artery and the intercostal arteries, probably because of the small diameter of the branches. Intercostal arteries arise from the dorsal aspect of the aorta, while bronchial arteries arise from its ventral aspect. The frequency of a trunk of right bronchial and intercostal arteries is previously reported as 53.4%–66.8%^[10,11]; in the present study, this frequency was 70% (67/95) (Table 4), while that of a trunk of left bronchial and intercostal arteries was 3% (2/66), and that of a trunk of common tract and intercostal arteries was 6% (2/36). This difference in frequency between the right, left, and common trunk arteries may be related to the direction of division: i.e. the left bronchial artery and common trunk arteries most commonly divide at 11 to 1 o'clock, while the right bronchial artery most commonly divides at 9 to 10 o'clock. The intercostal arteries divided dorsal to the right bronchial arteries at the approximate

center of the thoracic vertebrae (Figure 3). Therefore, during catheterization in BAE, the microcatheter might pass over this dividing point to avoid causing neurological complications.

One of the weaknesses in our MDCT study was the failure to delineate the right bronchial artery in 1 subject and the left bronchial artery in 9 subjects. In a previous MDCT series, Morita *et al.*^[5] reported that MDCT did not detect 6 small bronchial arteries that were later revealed during surgery. In the present series, the mean CT values on CTA at the level of the ascending aorta, aortic arch, descending aorta, and diaphragm ranged from 389 to 353 HU. A greater density of contrast medium in the aorta and thinner CT slices would improve the detection of small bronchial arteries. Another weakness is that the present study is restricted to patients without any episode of hemoptysis. In contrast, in cases of hemoptysis the responsible bronchial artery is usually dilated and easily delineated on MDCT^[2,4].

In conclusion, although we could not demonstrate all of the bronchial arteries on MDCT, CTA using MDCT provides detailed information regarding the relation between bronchial artery ostia and tracheal bifurcation.

COMMENTS

Background

Although relationships between the origin of bronchial arteries and the thoracic vertebrae are known from early studies, it is clinically useful to know how the bronchial artery ostia relate to tracheal bifurcation rather than to the thoracic vertebrae because the tracheal bifurcation is visible fluoroscopically but the exact thoracic vertebral level is difficult to identify.

Research frontiers

The intact relation between bronchial artery ostia and tracheal bifurcation has not been reported yet in a population with no cause to have enlarged bronchial arteries.

Innovations and breakthroughs

Of the 95 right bronchial arteries, 29 (31%) divided at a level 0–1 cm cranial to the bifurcation, 60 (64%) at 0–2 cm cranial, and 13 (13%) at –1 to 0 cm caudal to the bifurcation. A total of 73 (77%) right bronchial arteries divided at between –1 and 2 cm from the bifurcation. Of the 79 right bronchial arteries that divided from the descending aorta, 64 (81%) divided in the direction of 9 to 10 o'clock. Of the 16 right bronchial arteries that divided from the aortic arch, 13 (81%) divided in the right caudal direction, 2 in the left caudal direction, and 1 in the central caudal direction. Of the 66 left bronchial arteries, 33 (50%) divided at a level 0–1 cm cranial to the bifurcation, 42 (64%) at 0–2 cm cranial, and 12 (18%) at –1 to 0 cm caudal to the bifurcation. A total of 54 (82%) left bronchial arteries divided at between –1 and 2 cm from the bifurcation.

Applications

The left bronchial artery and common trunk arteries most commonly divide at 11 to 1 o'clock, while the right bronchial artery most commonly divides at 9 to 10 o'clock. The intercostal arteries divide dorsal to the right bronchial arteries at the approximate center of the thoracic vertebrae. Therefore, during catheterization in BAE, the microcatheter might pass over this dividing point to avoid causing neurological complications.

Terminology

Computed tomography angiography (CTA) angiography using MDCT provides detailed information regarding the relation between bronchial artery ostia and tracheal bifurcation.

Peer review

This is a well-written manuscript that aim to explore the anatomical relationships between bronchial artery and tracheal bifurcation using CTA. There are a few points to be cleared.

REFERENCES

- 1 **Remy-Jardin M**, Bouaziz N, Dumont P, Brillet PY, Bruzzi J, Remy J. Bronchial and nonbronchial systemic arteries at multi-detector row CT angiography: comparison with conventional angiography. *Radiology* 2004; **233**: 741-749
- 2 **Bruzzi JF**, Rémy-Jardin M, Delhay D, Teisseire A, Khalil C, Rémy J. Multi-detector row CT of hemoptysis. *Radiographics* 2006; **26**: 3-22
- 3 **Yoon YC**, Lee KS, Jeong YJ, Shin SW, Chung MJ, Kwon OJ. Hemoptysis: bronchial and nonbronchial systemic arteries at 16-detector row CT. *Radiology* 2005; **234**: 292-298
- 4 **Chung MJ**, Lee JH, Lee KS, Yoon YC, Kwon OJ, Kim TS. Bronchial and nonbronchial systemic arteries in patients with hemoptysis: depiction on MDCT angiography. *AJR Am J Roentgenol* 2006; **186**: 649-655
- 5 **Morita Y**, Takase K, Ichikawa H, Yamada T, Sato A, Higano S, Takahashi S. Bronchial artery anatomy: preoperative 3D simulation with multidetector CT. *Radiology* 2010; **255**: 934-943
- 6 **Battal B**, Saglam M, Ors F, Akgun V, Dakak M. Aberrant right bronchial artery originating from right coronary artery - MDCT angiography findings. *Br J Radiol* 2010; **83**: e101-e104
- 7 **Yoon W**, Kim JK, Kim YH, Chung TW, Kang HK. Bronchial and nonbronchial systemic artery embolization for life-threatening hemoptysis: a comprehensive review. *Radiographics* 2002; **22**: 1395-1409
- 8 **Yoon W**, Kim YH, Kim JK, Kim YC, Park JG, Kang HK. Massive hemoptysis: prediction of nonbronchial systemic arterial supply with chest CT. *Radiology* 2003; **227**: 232-238
- 9 **Rémy J**, Arnaud A, Fardou H, Giraud R, Voisin C. Treatment of hemoptysis by embolization of bronchial arteries. *Radiology* 1977; **122**: 33-37
- 10 **Kasai T**, Chiba S. Macroscopic anatomy of the bronchial arteries. *Anat Anz* 1979; **145**: 166-181
- 11 **Cauldwell EW**, Siekert RG. The bronchial arteries; an anatomic study of 150 human cadavers. *Surg Gynecol Obstet* 1948; **86**: 395-412

S- Editor Cheng JX L- Editor O'Neill M E- Editor Zheng XM



ACKNOWLEDGMENTS

Acknowledgments to reviewers of *World Journal of Radiology*

Many reviewers have contributed their expertise and time to the peer review, a critical process to ensure the quality of *World Journal of Radiology*. The editors and authors of the articles submitted to the journal are grateful to the following reviewers for evaluating the articles (including those published in this issue and those rejected for this issue) during the last editing time period.

Dr. Kazushi Kishi, Wakayama Medical University, Kimiidera 811-1, Wakayama City 641-8510, Japan

Wazir Muhammad, PhD, Nuclear Energy Application Laboratory, Department of Physics, Kyungpook National University,

Sankuk-dong, Buk-gu, Daegu 702-701, South Korea

Yahya Paksoy, MD, Professor, Department of Radiology, Selcuk University Meram School of Medicine, 42085 Konya, Turkey

Dr. Monvadi Barbara Srichai-Parsia, Department of Radiology and Medicine, NYU School of Medicine, 530 First Avenue, HCC-C48, New York 11211, United States

Ioannis Tsalafoutas, PhD, Medical Physics Department, Anticancer Hospital "Agios Savvas", 115 22 Athens, Greece

Ender Uysal, MD, Sisli Etfal Training and Research Hospital, Clinic of Radiology, Sisli Etfal Eğitim ve Araştırma Hastanesi Radyoloji Kliniği, Etfal sok. Sisli, Istanbul 34377, Turkey



MEETINGS

Events Calendar 2012

January 3-7, 2012

Imaging at Bachelor Gulch
Beaver Creek, CO 81620,
United States

January 12-14, 2012

IROS 2012: Interventionell
Radiologischen Olbert Symposium
Salzburg, Austria

January 26-29, 2012

American Society of Neuroimaging
2012 35th Annual Meeting
Miami, FL 33169, United States

February 9-11, 2012

JIM joint interventional meeting
2012
Rome, Italy

February 13-16, 2012

Emergency Radiology
Palm Beach, FL 33480, United States

February 16-19, 2012

ASSR 2012 Annual Symposium
Miami Beach, FL 33169,
United States

February 19-23, 2012

Internal Derangements of Joints:
Advanced and Intensive MR
Imaging/With a Special Symposium
on Ankle and Foot
Coronado, CA 92118, United States

February 21-24, 2012

MRI in Practice
Oslo, Norway

March 1-5, 2012

ECR 2012
Vienna, Austria

March 7-10, 2012

ISCD's 18th Annual Meeting
Los Angeles, CA 90001,
United States

March 7-11, 2012

7th Annual Fundamentals of
Musculoskeletal Ultrasound
San Diego, CA 92111, United States

March 25-30, 2012

Diseases of the Brain, Head and
Neck Spine
Davos, Switzerland
April 13-15, 2012
ACR 35th National Conference on
Breast Cancer
Hollywood, FL 33019, United States

April 22-24, 2012

Euroson 2012
Madrid, Spain

April 24-27, 2012

MRI in Practice
Aalst, Belgium

April 25-28, 2012

ECIO 2012 - Third European
Conference on Interventional
Oncology
Florence, Italy

May 15-18, 2012

EURO PCR
Paris, France

May 19-23, 2012

ECTS 2012
Stockholm, Sweden

May 28-June 01, 2012

The International Congress of
Pediatric Radiology
Athens Greece

June 7-9, 2012

ASCI 2012 6th Congress of Asian
Society of Cardiovascular Imaging
Bangkok, Thailand

June 14-16, 2012

ICCIR 2012 - International
Conference on Complications in

Interventional Radiology
Poertschach, Austria

June 16-19, 2012

2nd IDKD Hong Kong 2012,
Diseases of the Abdomen and Pelvis
Hong Kong, China

June 17-20, 2012

14th Annual International
Symposium on Multidetector-Row
CT
San Francisco, CA 94103,
United States

June 27-30, 2012

CARS 2012
Pisa, Italy

July 1-3, 2012

16th Symposium Mammographicum
Harrogate, United Kingdom

July 19-22, 2012

Society of Cardiovascular Computed
Tomography 6th Annual Scientific
Meeting
Baltimore, Maryland

August 30-2, 2012

14th Asian Oceanian Congress of
Radiology
Sydney, Australia

September 6-8, 2012

Update in Abdominal and
Urogenital Imaging
Bruges, Belgium

September 12-15, 2012

ISS 2012
Rome, Italy

September 13-15, 2012

4th ESMINT Congress
Nice, France

September 13-16, 2012

18th Annual Symposium ESUR
Edinburgh, United Kingdom

September 15-19, 2012

CIRSE 2012
Lisbon, Portugal

September 20-23, 2012

2012 SDMS Annual Conference
Seattle, WA 98113, United States

September 24-27, 2012

MRI in Practice
Ballerup, Denmark

October 4-6, 2012

ESMRMB congress 2012 29th Annual
Scientific Meeting
Lisbon, Portugal

October 12-13, 2012

EUSOBI Annual Scientific Meeting
2012
Barcelona, Spain

October 26-28, 2012

22th Annual Meeting of the Society
of Radiologists in Ultrasound
Baltimore, MD 21213, United States

November 10-14, 2012

13th congress of WFITN
Buenos Aires, Argentina

November 14-17, 2012

BSIR Annual Meeting 2012
Bournemouth, United Kingdom

November 27- December 03, 2012

IEEE Nuclear Science Symposium
and Medical Imaging Conference
Anaheim, CA 92805, United States

December 2-4, 2012

ICI 2012 - Innovations in
Cardiovascular Interventions
Meeting
Tel Aviv, Israel

December 4-8, 2012

34rd San Antonio Breast Cancer
Symposium,
San Antonio, TX 78258 ,
United States



INSTRUCTIONS TO AUTHORS

GENERAL INFORMATION

World Journal of Radiology (*World J Radiol*, *WJR*, online ISSN 1949-8470, DOI: 10.4329), is a monthly, open-access (OA), peer-reviewed journal supported by an editorial board of 319 experts in Radiology from 40 countries.

The biggest advantage of the OA model is that it provides free, full-text articles in PDF and other formats for experts and the public without registration, which eliminates the obstacle that traditional journals possess and usually delays the speed of the propagation and communication of scientific research results. The open access model has been proven to be a true approach that may achieve the ultimate goal of the journals, i.e. the maximization of the value to the readers, authors and society.

Maximization of personal benefits

The role of academic journals is to exhibit the scientific levels of a country, a university, a center, a department, and even a scientist, and build an important bridge for communication between scientists and the public. As we all know, the significance of the publication of scientific articles lies not only in disseminating and communicating innovative scientific achievements and academic views, as well as promoting the application of scientific achievements, but also in formally recognizing the "priority" and "copyright" of innovative achievements published, as well as evaluating research performance and academic levels. So, to realize these desired attributes of *WJR* and create a well-recognized journal, the following four types of personal benefits should be maximized. The maximization of personal benefits refers to the pursuit of the maximum personal benefits in a well-considered optimal manner without violation of the laws, ethical rules and the benefits of others. (1) Maximization of the benefits of editorial board members: The primary task of editorial board members is to give a peer review of an unpublished scientific article via online office system to evaluate its innovativeness, scientific and practical values and determine whether it should be published or not. During peer review, editorial board members can also obtain cutting-edge information in that field at first hand. As leaders in their field, they have priority to be invited to write articles and publish commentary articles. We will put peer reviewers' names and affiliations along with the article they reviewed in the journal to acknowledge their contribution; (2) Maximization of the benefits of authors: Since *WJR* is an open-access journal, readers around the world can immediately download and read, free of charge, high-quality, peer-reviewed articles from *WJR* official website, thereby realizing the goals and significance of the communication between authors and peers as well as public reading; (3) Maximization of the benefits of readers: Readers can read or use, free of charge, high-quality peer-reviewed articles without any limits, and cite the arguments, viewpoints, concepts, theories, methods, results, conclusion or facts and data of pertinent literature so as to validate the innovativeness, scientific and practical values of their own research achievements, thus ensuring that their articles have novel arguments or viewpoints, solid evidence and correct conclusion; and (4) Maximization of the benefits of employees: It is an iron law that a first-class journal is unable to exist without first-class editors, and only first-class editors can create a first-class academic journal. We insist on strengthening our team cultivation and construction so that every employee, in an open, fair and transparent environment, could contribute their wisdom to edit and publish high-quality ar-

ticles, thereby realizing the maximization of the personal benefits of editorial board members, authors and readers, and yielding the greatest social and economic benefits.

Aims and scope

The major task of *WJR* is to rapidly report the most recent improvement in the research of medical imaging and radiation therapy by the radiologists. *WJR* accepts papers on the following aspects related to radiology: Abdominal radiology, women health radiology, cardiovascular radiology, chest radiology, genitourinary radiology, neuroradiology, head and neck radiology, interventional radiology, musculoskeletal radiology, molecular imaging, pediatric radiology, experimental radiology, radiological technology, nuclear medicine, PACS and radiology informatics, and ultrasound. We also encourage papers that cover all other areas of radiology as well as basic research.

Columns

The columns in the issues of *WJR* will include: (1) Editorial: To introduce and comment on major advances and developments in the field; (2) Frontier: To review representative achievements, comment on the state of current research, and propose directions for future research; (3) Topic Highlight: This column consists of three formats, including (A) 10 invited review articles on a hot topic, (B) a commentary on common issues of this hot topic, and (C) a commentary on the 10 individual articles; (4) Observation: To update the development of old and new questions, highlight unsolved problems, and provide strategies on how to solve the questions; (5) Guidelines for Basic Research: To provide guidelines for basic research; (6) Guidelines for Clinical Practice: To provide guidelines for clinical diagnosis and treatment; (7) Review: To review systemically progress and unresolved problems in the field, comment on the state of current research, and make suggestions for future work; (8) Original Articles: To report innovative and original findings in radiology; (9) Brief Articles: To briefly report the novel and innovative findings in radiology; (10) Case Report: To report a rare or typical case; (11) Letters to the Editor: To discuss and make reply to the contributions published in *WJR*, or to introduce and comment on a controversial issue of general interest; (12) Book Reviews: To introduce and comment on quality monographs of radiology; and (13) Guidelines: To introduce consensus and guidelines reached by international and national academic authorities worldwide on the research in radiology.

Name of journal

World Journal of Radiology

ISSN

ISSN 1949-8470 (online)

Editor-in-Chief

Filippo Cademartiri, MD, PhD, FESC, FSCCT, Professor, Cardio-Vascular Imaging Unit-Giovanni XXIII Hospital, Via Giovanni XXIII, 7-31050-Monastier di Treviso (TV), Italy

Editorial Office

World Journal of Radiology

Editorial Department: Room 903, Building D,
Ocean International Center, No. 62 Dongsihuan Zhonglu,
Chaoyang District, Beijing 100025, China

Instructions to authors

E-mail: [wjw@wjnet.com](mailto:wjr@wjnet.com)
<http://www.wjnet.com>
Telephone: +86-10-59080039
Fax: +86-10-85381893

Indexed and Abstracted in

PubMed Central, PubMed, Digital Object Identifier, and Directory of Open Access Journals.

Published by

Baishideng Publishing Group Co., Limited.

SPECIAL STATEMENT

All articles published in this journal represent the viewpoints of the authors except where indicated otherwise.

Biostatistical editing

Statistical review is performed after peer review. We invite an expert in Biomedical Statistics from to evaluate the statistical method used in the paper, including *t*-test (group or paired comparisons), chi-squared test, Redit, probit, logit, regression (linear, curvilinear, or stepwise), correlation, analysis of variance, analysis of covariance, *etc.* The reviewing points include: (1) Statistical methods should be described when they are used to verify the results; (2) Whether the statistical techniques are suitable or correct; (3) Only homogeneous data can be averaged. Standard deviations are preferred to standard errors. Give the number of observations and subjects (*n*). Losses in observations, such as drop-outs from the study should be reported; (4) Values such as ED50, LD50, IC50 should have their 95% confidence limits calculated and compared by weighted probit analysis (Bliss and Finney); and (5) The word 'significantly' should be replaced by its synonyms (if it indicates extent) or the *P* value (if it indicates statistical significance).

Conflict-of-interest statement

In the interests of transparency and to help reviewers assess any potential bias, *WJR* requires authors of all papers to declare any competing commercial, personal, political, intellectual, or religious interests in relation to the submitted work. Referees are also asked to indicate any potential conflict they might have reviewing a particular paper. Before submitting, authors are suggested to read "Uniform Requirements for Manuscripts Submitted to Biomedical Journals: Ethical Considerations in the Conduct and Reporting of Research: Conflicts of Interest" from International Committee of Medical Journal Editors (ICMJE), which is available at: http://www.icmje.org/ethical_4conflicts.html.

Sample wording: [Name of individual] has received fees for serving as a speaker, a consultant and an advisory board member for [names of organizations], and has received research funding from [names of organization]. [Name of individual] is an employee of [name of organization]. [Name of individual] owns stocks and shares in [name of organization]. [Name of individual] owns patent [patent identification and brief description].

Statement of informed consent

Manuscripts should contain a statement to the effect that all human studies have been reviewed by the appropriate ethics committee or it should be stated clearly in the text that all persons gave their informed consent prior to their inclusion in the study. Details that might disclose the identity of the subjects under study should be omitted. Authors should also draw attention to the Code of Ethics of the World Medical Association (Declaration of Helsinki, 1964, as revised in 2004).

Statement of human and animal rights

When reporting the results from experiments, authors should follow the highest standards and the trial should conform to Good Clinical Practice (for example, US Food and Drug Administration Good Clinical Practice in FDA-Regulated Clinical Trials; UK Medicines Research Council Guidelines for Good Clinical Practice in Clinical Trials) and/or the World Medical Association Declaration of Helsinki. Generally, we suggest authors follow the lead investigator's national standard. If doubt exists whether the research was conducted

in accordance with the above standards, the authors must explain the rationale for their approach and demonstrate that the institutional review body explicitly approved the doubtful aspects of the study.

Before submitting, authors should make their study approved by the relevant research ethics committee or institutional review board. If human participants were involved, manuscripts must be accompanied by a statement that the experiments were undertaken with the understanding and appropriate informed consent of each. Any personal item or information will not be published without explicit consents from the involved patients. If experimental animals were used, the materials and methods (experimental procedures) section must clearly indicate that appropriate measures were taken to minimize pain or discomfort, and details of animal care should be provided.

SUBMISSION OF MANUSCRIPTS

Manuscripts should be typed in 1.5 line spacing and 12 pt. Book Antiqua with ample margins. Number all pages consecutively, and start each of the following sections on a new page: Title Page, Abstract, Introduction, Materials and Methods, Results, Discussion, Acknowledgements, References, Tables, Figures, and Figure Legends. Neither the editors nor the publisher are responsible for the opinions expressed by contributors. Manuscripts formally accepted for publication become the permanent property of Baishideng Publishing Group Co., Limited, and may not be reproduced by any means, in whole or in part, without the written permission of both the authors and the publisher. We reserve the right to copy-edit and put onto our website accepted manuscripts. Authors should follow the relevant guidelines for the care and use of laboratory animals of their institution or national animal welfare committee. For the sake of transparency in regard to the performance and reporting of clinical trials, we endorse the policy of the ICMJE to refuse to publish papers on clinical trial results if the trial was not recorded in a publicly-accessible registry at its outset. The only register now available, to our knowledge, is <http://www.clinicaltrials.gov> sponsored by the United States National Library of Medicine and we encourage all potential contributors to register with it. However, in the case that other registers become available you will be duly notified. A letter of recommendation from each author's organization should be provided with the contributed article to ensure the privacy and secrecy of research is protected.

Authors should retain one copy of the text, tables, photographs and illustrations because rejected manuscripts will not be returned to the author(s) and the editors will not be responsible for loss or damage to photographs and illustrations sustained during mailing.

Online submissions

Manuscripts should be submitted through the Online Submission System at: <http://www.wjnet.com/1949-8470/office>. Authors are highly recommended to consult the ONLINE INSTRUCTIONS TO AUTHORS (http://www.wjnet.com/1949-8470/g_info_20100316162358.htm) before attempting to submit online. For assistance, authors encountering problems with the Online Submission System may send an email describing the problem to [wjw@wjnet.com](mailto:wjr@wjnet.com), or by telephone: +86-10-85381892. If you submit your manuscript online, do not make a postal contribution. Repeated online submission for the same manuscript is strictly prohibited.

MANUSCRIPT PREPARATION

All contributions should be written in English. All articles must be submitted using word-processing software. All submissions must be typed in 1.5 line spacing and 12 pt. Book Antiqua with ample margins. Style should conform to our house format. Required information for each of the manuscript sections is as follows:

Title page

Title: Title should be less than 12 words.

Running title: A short running title of less than 6 words should be provided.

Authorship: Authorship credit should be in accordance with the standard proposed by International Committee of Medical Journal Editors, based on (1) substantial contributions to conception and design, acquisition of data, or analysis and interpretation of data; (2) drafting the article or revising it critically for important intellectual content; and (3) final approval of the version to be published. Authors should meet conditions 1, 2, and 3.

Institution: Author names should be given first, then the complete name of institution, city, province and postcode. For example, Xu-Chen Zhang, Li-Xin Mei, Department of Pathology, Chengde Medical College, Chengde 067000, Hebei Province, China. One author may be represented from two institutions, for example, George Sgourakis, Department of General, Visceral, and Transplantation Surgery, Essen 45122, Germany; George Sgourakis, 2nd Surgical Department, Korgialenio-Benakio Red Cross Hospital, Athens 15451, Greece

Author contributions: The format of this section should be: Author contributions: Wang CL and Liang L contributed equally to this work; Wang CL, Liang L, Fu JF, Zou CC, Hong F and Wu XM designed the research; Wang CL, Zou CC, Hong F and Wu XM performed the research; Xue JZ and Lu JR contributed new reagents/analytic tools; Wang CL, Liang L and Fu JF analyzed the data; and Wang CL, Liang L and Fu JF wrote the paper.

Supportive foundations: The complete name and number of supportive foundations should be provided, e.g., Supported by National Natural Science Foundation of China, No. 30224801

Correspondence to: Only one corresponding address should be provided. Author names should be given first, then author title, affiliation, the complete name of institution, city, postcode, province, country, and email. All the letters in the email should be in lower case. A space interval should be inserted between country name and email address. For example, Montgomery Bissell, MD, Professor of Medicine, Chief, Liver Center, Gastroenterology Division, University of California, Box 0538, San Francisco, CA 94143, United States. montgomery.bissell@ucsf.edu

Telephone and fax: Telephone and fax should consist of +, country number, district number and telephone or fax number, e.g., Telephone: +86-10-85381892 Fax: +86-10-85381893

Peer reviewers: All articles received are subject to peer review. Normally, three experts are invited for each article. Decision for acceptance is made only when at least two experts recommend an article for publication. Reviewers for accepted manuscripts are acknowledged in each manuscript, and reviewers of articles which were not accepted will be acknowledged at the end of each issue. To ensure the quality of the articles published in *WJR*, reviewers of accepted manuscripts will be announced by publishing the name, title/position and institution of the reviewer in the footnote accompanying the printed article. For example, reviewers: Professor Jing-Yuan Fang, Shanghai Institute of Digestive Disease, Shanghai, Affiliated Renji Hospital, Medical Faculty, Shanghai Jiaotong University, Shanghai, China; Professor Xin-Wei Han, Department of Radiology, The First Affiliated Hospital, Zhengzhou University, Zhengzhou, Henan Province, China; and Professor Anren Kuang, Department of Nuclear Medicine, Huaxi Hospital, Sichuan University, Chengdu, Sichuan Province, China.

Abstract

There are unstructured abstracts (no more than 256 words) and structured abstracts (no more than 480). The specific requirements for structured abstracts are as follows:

An informative, structured abstracts of no more than 480 words should accompany each manuscript. Abstracts for original contributions should be structured into the following sections. AIM (no more than 20 words): Only the purpose should be included. Please write the aim as the form of "To investigate/study/...;

MATERIALS AND METHODS (no more than 140 words); RESULTS (no more than 294 words): You should present *P* values where appropriate and must provide relevant data to illustrate how they were obtained, e.g. 6.92 ± 3.86 vs 3.61 ± 1.67 , $P < 0.001$; CONCLUSION (no more than 26 words).

Key words

Please list 5-10 key words, selected mainly from *Index Medicus*, which reflect the content of the study.

Text

For articles of these sections, original articles and brief articles, the main text should be structured into the following sections: INTRODUCTION, MATERIALS AND METHODS, RESULTS and DISCUSSION, and should include appropriate Figures and Tables. Data should be presented in the main text or in Figures and Tables, but not in both. The main text format of these sections, editorial, topic highlight, case report, letters to the editors, can be found at: http://www.wjgnet.com/1949-8470/g_info_20100313183720.htm.

Illustrations

Figures should be numbered as 1, 2, 3, *etc.*, and mentioned clearly in the main text. Provide a brief title for each figure on a separate page. Detailed legends should not be provided under the figures. This part should be added into the text where the figures are applicable. Figures should be either Photoshop or Illustrator files (in tiff, eps, jpeg formats) at high-resolution. Examples can be found at: <http://www.wjgnet.com/1007-9327/13/4520.pdf>; <http://www.wjgnet.com/1007-9327/13/4554.pdf>; <http://www.wjgnet.com/1007-9327/13/4891.pdf>; <http://www.wjgnet.com/1007-9327/13/4986.pdf>; <http://www.wjgnet.com/1007-9327/13/4498.pdf>. Keeping all elements compiled is necessary in line-art image. Scale bars should be used rather than magnification factors, with the length of the bar defined in the legend rather than on the bar itself. File names should identify the figure and panel. Avoid layering type directly over shaded or textured areas. Please use uniform legends for the same subjects. For example: Figure 1 Pathological changes in atrophic gastritis after treatment. A: ...; B: ...; C: ...; D: ...; E: ...; F: ...; G: ... *etc.* It is our principle to publish high resolution-figures for the printed and E-versions.

Tables

Three-line tables should be numbered 1, 2, 3, *etc.*, and mentioned clearly in the main text. Provide a brief title for each table. Detailed legends should not be included under tables, but rather added into the text where applicable. The information should complement, but not duplicate the text. Use one horizontal line under the title, a second under column heads, and a third below the Table, above any footnotes. Vertical and italic lines should be omitted.

Notes in tables and illustrations

Data that are not statistically significant should not be noted. ^a*P* < 0.05, ^b*P* < 0.01 should be noted (*P* > 0.05 should not be noted). If there are other series of *P* values, ^c*P* < 0.05 and ^d*P* < 0.01 are used. A third series of *P* values can be expressed as ^e*P* < 0.05 and ^f*P* < 0.01. Other notes in tables or under illustrations should be expressed as ¹F, ²F, ³F; or sometimes as other symbols with a superscript (Arabic numerals) in the upper left corner. In a multi-curve illustration, each curve should be labeled with ●, ○, ■, □, ▲, △, *etc.*, in a certain sequence.

Acknowledgments

Brief acknowledgments of persons who have made genuine contributions to the manuscript and who endorse the data and conclusions should be included. Authors are responsible for obtaining written permission to use any copyrighted text and/or illustrations.

REFERENCES

Coding system

The author should number the references in Arabic numerals ac-

Instructions to authors

cording to the citation order in the text. Put reference numbers in square brackets in superscript at the end of citation content or after the cited author's name. For citation content which is part of the narration, the coding number and square brackets should be typeset normally. For example, "Crohn's disease (CD) is associated with increased intestinal permeability^[1,2]". If references are cited directly in the text, they should be put together within the text, for example, "From references^[19,22-24], we know that..."

When the authors write the references, please ensure that the order in text is the same as in the references section, and also ensure the spelling accuracy of the first author's name. Do not list the same citation twice.

PMID and DOI

Please provide PubMed citation numbers to the reference list, e.g. PMID and DOI, which can be found at <http://www.ncbi.nlm.nih.gov/sites/entrez?db=pubmed> and <http://www.crossref.org/SimpleTextQuery/>, respectively. The numbers will be used in E-version of this journal.

Style for journal references

Authors: the name of the first author should be typed in bold-faced letters. The family name of all authors should be typed with the initial letter capitalized, followed by their abbreviated first and middle initials. (For example, Lian-Sheng Ma is abbreviated as Ma LS, Bo-Rong Pan as Pan BR). The title of the cited article and italicized journal title (journal title should be in its abbreviated form as shown in PubMed), publication date, volume number (in black), start page, and end page [PMID: 11819634 DOI: 10.3748/wjg.13.5396].

Style for book references

Authors: the name of the first author should be typed in bold-faced letters. The surname of all authors should be typed with the initial letter capitalized, followed by their abbreviated middle and first initials. (For example, Lian-Sheng Ma is abbreviated as Ma LS, Bo-Rong Pan as Pan BR) Book title. Publication number. Publication place: Publication press, Year: start page and end page.

Format

Journals

English journal article (list all authors and include the PMID where applicable)

- 1 **Jung EM**, Clevert DA, Schreyer AG, Schmitt S, Rennert J, Kubale R, Feuerbach S, Jung F. Evaluation of quantitative contrast harmonic imaging to assess malignancy of liver tumors: A prospective controlled two-center study. *World J Gastroenterol* 2007; **13**: 6356-6364 [PMID: 18081224 DOI: 10.3748/wjg.13.6356]

Chinese journal article (list all authors and include the PMID where applicable)

- 2 **Lin GZ**, Wang XZ, Wang P, Lin J, Yang FD. Immunologic effect of Jianpi Yishen decoction in treatment of Pixu-diarhoea. *Shijie Huaren Xiaohua Zazhi* 1999; **7**: 285-287

In press

- 3 **Tian D**, Araki H, Stahl E, Bergelson J, Kreitman M. Signature of balancing selection in Arabidopsis. *Proc Natl Acad Sci USA* 2006; In press

Organization as author

- 4 **Diabetes Prevention Program Research Group**. Hypertension, insulin, and proinsulin in participants with impaired glucose tolerance. *Hypertension* 2002; **40**: 679-686 [PMID: 12411462 PMID: 2516377 DOI: 10.1161/01.HYP.0000035706.28494.09]

Both personal authors and an organization as author

- 5 **Vallancien G**, Emberton M, Harving N, van Moorselaar RJ; Alf-One Study Group. Sexual dysfunction in 1, 274 European men suffering from lower urinary tract symptoms. *J Urol* 2003; **169**: 2257-2261 [PMID: 12771764 DOI: 10.1097/01.ju.0000067940.76090.73]

No author given

- 6 21st century heart solution may have a sting in the tail. *BMJ*

2002; **325**: 184 [PMID: 12142303 DOI: 10.1136/bmj.325.7357.184]

Volume with supplement

- 7 **Geraud G**, Spierings EL, Keywood C. Tolerability and safety of frovatriptan with short- and long-term use for treatment of migraine and in comparison with sumatriptan. *Headache* 2002; **42** Suppl 2: S93-99 [PMID: 12028325 DOI: 10.1046/j.1526-4610.42.s2.7.x]

Issue with no volume

- 8 **Banit DM**, Kaufer H, Hartford JM. Intraoperative frozen section analysis in revision total joint arthroplasty. *Clin Orthop Relat Res* 2002; **(401)**: 230-238 [PMID: 12151900 DOI: 10.1097/00003086-200208000-00026]

No volume or issue

- 9 Outreach: Bringing HIV-positive individuals into care. *HRSA Careaction* 2002; 1-6 [PMID: 12154804]

Books

Personal author(s)

- 10 **Sherlock S**, Dooley J. Diseases of the liver and biliary system. 9th ed. Oxford: Blackwell Sci Pub, 1993: 258-296

Chapter in a book (list all authors)

- 11 **Lam SK**. Academic investigator's perspectives of medical treatment for peptic ulcer. In: Swabb EA, Azabo S. Ulcer disease: investigation and basis for therapy. New York: Marcel Dekker, 1991: 431-450

Author(s) and editor(s)

- 12 **Breedlove GK**, Schorfheide AM. Adolescent pregnancy. 2nd ed. Wiczorek RR, editor. White Plains (NY): March of Dimes Education Services, 2001: 20-34

Conference proceedings

- 13 **Harden P**, Joffe JK, Jones WG, editors. Germ cell tumours V. Proceedings of the 5th Germ cell tumours Conference; 2001 Sep 13-15; Leeds, UK. New York: Springer, 2002: 30-56

Conference paper

- 14 **Christensen S**, Oppacher F. An analysis of Koza's computational effort statistic for genetic programming. In: Foster JA, Lutton E, Miller J, Ryan C, Tettamanzi AG, editors. Genetic programming. EuroGP 2002: Proceedings of the 5th European Conference on Genetic Programming; 2002 Apr 3-5; Kinsdale, Ireland. Berlin: Springer, 2002: 182-191

Electronic journal (list all authors)

- 15 Morse SS. Factors in the emergence of infectious diseases. *Emerg Infect Dis* serial online, 1995-01-03, cited 1996-06-05; 1(1): 24 screens. Available from: URL: <http://www.cdc.gov/ncidod/eid/index.htm>

Patent (list all authors)

- 16 **Pagedas AC**, inventor; Ancel Surgical R&D Inc., assignee. Flexible endoscopic grasping and cutting device and positioning tool assembly. United States patent US 20020103498. 2002 Aug 1

Statistical data

Write as mean \pm SD or mean \pm SE.

Statistical expression

Express *t* test as *t* (in italics), *F* test as *F* (in italics), chi square test as χ^2 (in Greek), related coefficient as *r* (in italics), degree of freedom as *v* (in Greek), sample number as *n* (in italics), and probability as *P* (in italics).

Units

Use SI units. For example: body mass, *m* (B) = 78 kg; blood pressure, *p* (B) = 16.2/12.3 kPa; incubation time, *t* (incubation) = 96 h; blood glucose concentration, *c* (glucose) 6.4 ± 2.1 mmol/L; blood CEA mass concentration, *p* (CEA) = 8.6 ± 24.5 μ g/L; CO₂ volume fraction, 50 mL/L CO₂, not 5% CO₂; likewise for 40 g/L formaldehyde, not 10% formalin; and mass fraction, 8 ng/g, *etc.* Arabic numerals such as 23, 243, 641 should be read 23 243 641.

The format for how to accurately write common units and quantums can be found at: http://www.wjgnet.com/1949-8470/g_info_20100313185816.htm.

Abbreviations

Standard abbreviations should be defined in the abstract and on first mention in the text. In general, terms should not be abbreviated unless they are used repeatedly and the abbreviation is helpful to the reader. Permissible abbreviations are listed in Units, Symbols and Abbreviations: A Guide for Biological and Medical Editors and Authors (Ed. Baron DN, 1988) published by The Royal Society of Medicine, London. Certain commonly used abbreviations, such as DNA, RNA, HIV, LD50, PCR, HBV, ECG, WBC, RBC, CT, ESR, CSF, IgG, ELISA, PBS, ATP, EDTA, mAb, can be used directly without further explanation.

Italics

Quantities: *t* time or temperature, *c* concentration, *A* area, *l* length, *m* mass, *V* volume.

Genotypes: *gyrA*, *arg 1*, *c myc*, *c fos*, etc.

Restriction enzymes: *EcoRI*, *HindI*, *BamHI*, *Kbo I*, *Kpn I*, etc.

Biology: *H. pylori*, *E. coli*, etc.

Examples for paper writing

Editorial: http://www.wjgnet.com/1949-8470/g_info_20100313182341.htm

Frontier: http://www.wjgnet.com/1949-8470/g_info_20100313182448.htm

Topic highlight: http://www.wjgnet.com/1949-8470/g_info_20100313182639.htm

Observation: http://www.wjgnet.com/1949-8470/g_info_20100313182834.htm

Guidelines for basic research: http://www.wjgnet.com/1949-8470/g_info_20100313183057.htm

Guidelines for clinical practice: http://www.wjgnet.com/1949-8470/g_info_20100313183238.htm

Review: http://www.wjgnet.com/1949-8470/g_info_20100313183433.htm

Original articles: http://www.wjgnet.com/1949-8470/g_info_20100313183720.htm

Brief articles: http://www.wjgnet.com/1949-8470/g_info_20100313184005.htm

Case report: http://www.wjgnet.com/1949-8470/g_info_20100313184149.htm

Letters to the editor: http://www.wjgnet.com/1949-8470/g_info_20100313184410.htm

Book reviews: http://www.wjgnet.com/1949-8470/g_info_20100313184803.htm

Guidelines: http://www.wjgnet.com/1949-8470/g_info_20100313185047.htm

SUBMISSION OF THE REVISED MANUSCRIPTS AFTER ACCEPTED

Please revise your article according to the revision policies of *WJR*. The revised version including manuscript and high-resolution image figures (if any) should be re-submitted online (<http://www.wjgnet.com/1949-8470office/>). The author should send the copyright transfer letter, responses to the reviewers, English language Grade B certificate (for non-native speakers of English) and final manuscript checklist to [wjgnet.com](mailto:wjr@wjgnet.com).

Language evaluation

The language of a manuscript will be graded before it is sent for revision. (1) Grade A: priority publishing; (2) Grade B: minor language polishing; (3) Grade C: a great deal of language polishing needed; and (4) Grade D: rejected. Revised articles should reach Grade A or B.

Copyright assignment form

Please download a Copyright assignment form from http://www.wjgnet.com/1949-8470/g_info_20100313185522.htm.

Responses to reviewers

Please revise your article according to the comments/suggestions provided by the reviewers. The format for responses to the reviewers' comments can be found at: http://www.wjgnet.com/1949-8470/g_info_20100313185358.htm.

Proof of financial support

For paper supported by a foundation, authors should provide a copy of the document and serial number of the foundation.

Links to documents related to the manuscript

WJR will be initiating a platform to promote dynamic interactions between the editors, peer reviewers, readers and authors. After a manuscript is published online, links to the PDF version of the submitted manuscript, the peer-reviewers' report and the revised manuscript will be put on-line. Readers can make comments on the peer reviewer's report, authors' responses to peer reviewers, and the revised manuscript. We hope that authors will benefit from this feedback and be able to revise the manuscript accordingly in a timely manner.

Science news releases

Authors of accepted manuscripts are suggested to write a science news item to promote their articles. The news will be released rapidly at EurekaAlert/AAAS (<http://www.eurekaalert.org>). The title for news items should be less than 90 characters; the summary should be less than 75 words; and main body less than 500 words. Science news items should be lawful, ethical, and strictly based on your original content with an attractive title and interesting pictures.

Publication fee

WJR is an international, peer-reviewed, Open-Access, online journal. Articles published by this journal are distributed under the terms of the Creative Commons Attribution Non-commercial License, which permits use, distribution, and reproduction in any medium, provided the original work is properly cited, the use is non commercial and is otherwise in compliance with the license. Authors of accepted articles must pay a publication fee. The related standards are as follows. Publication fee: 1300 USD per article; Reprints fee: 350 USD per 100 reprints, including postage cost. Editorial, topic highlights, book reviews and letters to the editor are published free of charge.